Spring 2010

Electric Field Analysis in Insulating Films for Complex Electrode Systems

Anusha Jambula
Old Dominion University

Recommended Citation

Jambula, Anusha. "Electric Field Analysis in Insulating Films for Complex Electrode Systems" (2010). Master of Science (MS), Thesis, Electrical & Computer Engineering, Old Dominion University, DOI: 10.25777/gkzq-4m72
https://digitalcommons.odu.edu/ece_etds/376

TWO-DIMENSIONAL DRIFT-DIFFUSION SIMULATIONS OF SILICON AVALANCHE SHAPER (SAS) DEVICES FOR HIGH POWER APPLICATIONS

By:

Hamid Jalali
B.S.E.E. December 1994, Old Dominion University

A Thesis Submitted to the Faculty of
Old Dominion University in Partial Fulfillment of the
Requirements for the Degree of

MASTER OF SCIENCE

ELECTRICAL ENGINEERING

OLD DOMINION UNIVERSITY
August, 1996

Approved by:

Dr. R. P. Joshi

Dr. L. L. Vahala

Dr. G. A. Gerdin

ABSTRACT

TWO-DIMENSIONAL DRIFT-DIFFUSION SIMULATIONS OF SILICON AVALANCHE SHAPER (SAS) DEVICES FOR HIGH POWER APPLICATIONS

Hamid Jalali
Old Dominion University
Director: Dr. Ravindra Joshi

Silicon Avalanche Shaper devices have been projected as being important components of an inexpensive, semiconductor-based technology for high power switching applications. The primary advantage of this technology is that it is based on Silicon material which is easy to fabricate and has a well established processing technology. Unlike other high power technologies, the SAS devices do not rely on external optical triggering which eliminates the need for lasers and related optical circuitry.

The SAS based high power switching technology has been pioneered and tested by a Russian group. Though preliminary results have been very encouraging, the device reliability and its operating capability at high voltages have not been studied in detail. Also, the potential for internal current filametation and device breakdown has not been analyzed. This aspect can best be studied and understood through numerical simulations.

In this thesis, a two-dimensional simulator for the SAS has been developed based on the drift-diffusion model. The role of transverse variations in the doping profile have been analyzed by obtaining transient current characteristics. The results reveal the development and propagation of internal electric field waves. Simulation data for the conduction current distribution within the device at various time instants, clearly show the growth of filamentary modes. The filamentation is strongly dependent on the transverse doping characteristics.

ACKNOWLEDGEMENTS

I would first like to thank God for giving me the talent and ability to accomplish my goal of getting my Masters degree. I would like to thank Dr. Ravindra P. Joshi for his help and guidance throughout this research and my graduate career. His willingness to guide and assist in this research was impeccable. I would like to thank Dr. G. A. Gerdin and Dr. L. L. Vahala for serving on my thesis committee. I also would like to thank all the faculty at the ECE department, student advisors, and secretaries.

I am very grateful to the friends I have made throughout my college career. Sanjay Pathak, Zeki Hamsioglu, Behnam Dashtipour, Arvind Prabhu, and many others, have made my college years enjoyable and continue to be very close friends.

Finally, I would like to thank my parents for thier belief in me, my brothers for their support and guidance, my sisters and thier family for being there for me. The love and gratitude I have for them is beyond words. I also would like to thank all my friends back home and all over the world for keeping the long distance friendship up.

TABLE OF CONTENTS

PAGE

CHAPTER

LIST OF TABLES

LIST OF FIGURES

CHAPTER 1

INTRODUCTION

1.1 HIGH POWER SWITCHING

High power switches are the crucial components in a variety of engineering circuits. The switches are needed for a wide range of applications including high voltage pulse generators, dc to RF conversion, high energy pulsed lasers and generation of ultrawideband microwaves. The overriding motivation has been to develop compact switches that are capable of withstanding power levels in the MWatt and TeraWatt ranges, and can be activated within the nanosecond and subnanosecond time frames. These requirements, for instance, are encountered in controlled fusion projects, in high power lasers and accelerators, high frequency plasmatrons, high power radio transmitting, impulse radar systems, and frozen waveform generators [1].

In pulse power systems there are two basic ways to store electrical energy, namely in electric fields and in magnetic fields. To release the energy to the load, efficient switches are required to extract the energy from the electric (capacitive) and magnetic (inductive) energy storage elements. Often, this has to be done repetitively, at high frequency. Although energy can be stored at greater density using magnetic rather than electric fields, the latter are employed much more commonly because energy extraction is performed by closing switches which are essentially state-of-the-art devices for a very wide range of performance parameters. The opening switches needed to extract the energy from magnetic fields are less developed for high power applications [2].

The major factors which need to be considered in the development of high power switches include: (a) the efficiency of energy delivery from the pulser to the load, (b) shaping of the output pulses, and (c) the control of the timing and its relative sequence. The effects on efficiency arise, for example, from losses in the switch itself. The energy transferred to the load usually must be delivered as a pulse of given rise time and duration. In addition, the time of delivery of the pulse frequently must be controlled accurately. Also, since several switches may be used in one network to reduce the power dissipated per switch to a manageable level, close synchronization is often required [2].

Traditionally, fast high-power switching was realized with gas discharge devices. Consequently, the construction and technical feasibility of many installations and pulsed power projects was largely driven by progress in gas discharge switching. These devices, however, have a number of inherent shortcomings, and as a result, have largely been replaced in the last 15-20 years by high power semiconductors [1]. The shortcomings associated with gas discharge-based or mechanical switching include: (i) an inherently slower response, (ii) large bulk and size, and (iii) lower thermal capacity. The development of materials with non-linear resistivity in commercial quantities and a greater range of electrical characteristics, in particular those whose resistance depends upon current or temperature, gave rise to the utilization of solid state devices as closing and/or opening switches in pulse power applications [3,4]. Such semiconductor based switches have a number of potential advantages. These advantages include: (i) Compactness and small size leading to weight reductions, (ii) low jitter associated with optically triggered semiconductor switches, (iii) larger thermal capacity, (iv) ultrafast switching times and rapid repetition rates, and (v) the potential for a higher density plasma which can initiate a rapid transition into the conducting state.

Power switching by semiconductor devices of any type occurs through a strong modulated increase in the conductivity. In the "OFF" state, the device is in its high resistive state and so effectively blocks any external potential applied to the device. This region can either be the space charge region (SCR) of a reverse-biased junction which is completely depleted of free carriers by the strong external field, or a highly resistive low-doped semiconductor region. For schemes based on highly resistive low-doped semiconductors, the "OFF" state is maintained through Schottky contacts which provide an effective barrier to carrier injection. In the "ON" state, the conductivity of this region increases dramatically as it becomes filled with an electron-hole plasma. The electron-hole plasma can be created by any one of the following mechanisms:

(a) Photo-excitation by an external optical source such as a laser or a light emitting diode,

(b) Electron-beam bombardment to create a plasma,

(c) Charge injection through device contacts by applying a circuit voltage, and

(d) By initiating an internal avalanche breakdown process through either band-to-band or band-to-trap impact ionization.

The use of a solid state material with the resistivity changing reversibly by several orders of magnitude, provides a better alternative to high power switches. For example, many of the semiconductor switches exhibit volume conduction changes that, in contrast to arc discharges, do not involve ionization. A sufficient flux of photons [5,6] or charged particles [7] injected into normally high resistivity bulk semiconductors makes these materials conducting [2]. The most promising semiconductor switches appear to be those based on bulk material with carrier mobility changing throughout the entire device volume. Such materials, in principle, provide the highest volumetric efficiency since they would utilize the entire material volume uniformly on both microscopic and macroscopic scales [2]. The uniformity also works to ensure a homogeneous current density and should therefore reduce the potential for localized filamentation.

1.2 CHARACTERISTICS OF HIGH POWER SWITCHES

In general, solid state switches for high power applications should exhibit the following desirable characteristics:

- The ability to withstand high electric fields and to have a large breakdown/blocking voltage.
- Low leakage currents to preserve a high-impedance "OFF" state.
- Short turn-on times attainable through high mobility charge carriers.
- A very low resistance during the "ON" state and the ability to sustain high current densities.
- Device reliability and the absence of internal instabilities such as current filamentation.
- Good thermal conductivity for heat dissipation.
- A negative temperature coefficient for suppression of thermal instabilities.
- Simple structure and ease of fabrication for cost minimization.

Given the diverse applications of high power technology, the switches are generally required to have a broad range of characteristics. These characteristics can be grouped into those relating to the electrical capabilities of the switch and those relating to its physical, operational, and other features. Switch voltage characteristics include:

- Hold-off, or stand-off voltage.
- Voltage drop across the switch during conduction.
- Rate of rise or drop of voltage across the switch for opening and closing switches, repetitively.
- The possibility of prefire or switching below nominal switch hold-off voltage.
- The trigger voltage, or secondary voltage pulse necessary to initiate switching.

In addition to the voltage characteristics, there are several other switch characteristics which are related to current conduction. These include:

- The maximum current that can pass through the switch without damage.
- The maximum charge that can pass through the switch without damage.
- Rate of rise of current allowed by the switch during switching out of its low conductance state.

The product of the current through the switch and hold-off voltage, even though not necessarily occurring at the same time, provides the customary definition of power of the pulse that the switch handles. The energy handled by the switch is defined more rigorously, as the time integral of the product of current and voltage during switching. Some of the other design criteria and switch specifications include:

- Time of current conduction through the switch.
- Time of voltage hold-off.
- Opening time and closing time.
- Switching delay, or the interval between trigger signal and switch closing or opening.
- Jitter time, or the deviation from nominal switching delay time.
- The recovery time required by the switch to become ready for the next operation.
- Repetition rate (with the maximum rate being the inverse of the recovery rate).

Obviously not all the factors listed above are of consequence to each switch operation. Depending on the switch application, some of the following characteristics can also be significant and could frequently dominate the choice of the switches or determine their design:

- Lifetime, or the number of switching operations before failure.
- Reliability.
- Maintainability.
- Fault modes, or ways in which the switch fails.

- Ease of installation.
- Weight and volume.
- Cost.

Other characteristics also become important in those circumstances where large energy transfer through the switch occurs. These might include the thermal conductivity of the switch material, and the currents and/or device voltage thresholds beyond which reversibility between the conducting and non-conducting states is lost.

1.3 SEMICONDUCTOR SWITCH MATERIALS

The choice of the semiconducting material to be used for a high power switch is very important for optimizing the electrical characteristics, its efficiency and overall utility. As already mentioned, the switching process has to be initiated throughout the bulk of the device. Such a bulk generation has the following advantages: (i) Greater current carrying capability due to the larger available area, (ii) Better uniformity in the current density distribution, (iii) easier and faster heat dissipation for improved reliability and controlled device parameters, (iv) higher energy handling capacity, (v) lower internal resistance leading to reduced internal voltage drops and lower "RC" time constants.

Given the importance of bulk switching and plasma propagation throughout the device, the choice of a material for high power switching devices is guided by the bulk semiconductor properties. The bulk properties of some of the important semiconductors that have been developed and are currently available commercially are listed in Figure 1.1. The important parameters are: (i) The material band gap which controls leakage currents, places an upper limit on the operating temperature, the intrinsic carrier concentration and the impedance of the "OFF" state. (ii) The breakdown field and dielectric strength which determine the maximum hold-off voltage. These parameters also provide a measure of the device length necessary to ensure the blockage of high voltages. (iii) The saturated drift velocity which controls the response speed and the current density levels. (iv) The ionization coefficient which determines the threshold for impact ionization and the possibility for internal carrier generation through avalanching. (v) The nature of the band-gap since a direct bandgap semiconductor provides the possibility of optical excitation while an indirect semiconductor does not. (vi) The thermal conductivity which may become a relevant consideration for energy dissipation and in enhancing the power handling capacity. (vii) Ease of fabrication, commercial development of the semiconductor and relative costs of device manufacture.

Based on the above considerations, silicon and GaAs emerge as the materials of choice for high power switches. Of these GaAs is a direct bandgap material and is exclusive to optically based switches. Silicon, though unsuited for photoswitches, has a number of advantages over GaAs. For example, the related processing technology is very well developed and the costs involved in device manufacture are the least. It also has a much higher carrier drift velocity which ensures fast response times at high fields. The thermal conductivity is also larger than GaAs which is beneficial for high power switching. Finally, both Ohmic and Schottky contacts can be fabricated which are robust and increase the device reliability. Finally, Si unlike GaAs, does not exhibit the

property	Si	GaAs	GaP	3C-SiC (6H-SiC)	Diamond	GaN
Band gap (eV) at 300 K	1.1	1.4	2.3	2.2 (3.0)	5.5	3.39
Maximum operating temperature (K)	600	760	1250	1200 (1580)	1400	
Melting point (K)	1690	1510	1740	Sublimes >2100	Phase change	
Physical stability	Good	Fair	Excellent	Very good	Good	Good
Electron mobility RT, cm^2/Vs	1400	8500	350	1000 (600)	2200	900
Hole mobility RT, cm^2/Vs	600	400	100	40	1600	150
Breakdown voltage E_b, 10^6V/cm	0.3	0.4	–	4	10	5
Thermal conductivity c_T, W/cm	1.5	0.5	0.8	5	20	1.3
Sat. C. elec. drift vel. v(sat), 10^7cm/s	1	2	–	2	2.7	2.7
Dielectric const. K(0)	11.8	12.8	11.1	9.7	5.5	9

Figure 1.1. Comparison of important semiconductor properties.

intervalley electron transfer "Gunn effect" [8] which leads to negative differential conductivity (NDC). NDC, as is well known, is detrimental to reliable device and can give rise to internal instabilities. As a result, the research described in this thesis will focus on Silicon based high power switches. Finally, since silicon is not suited for photoexcitation, the switching mechanism and physics of device operation will be different from that used in other high power switches to date [9,10].

The high power switch studied here relies on the creation of an internal travelling electric field and the impact ionization of electron-hole pairs to trigger the device into the conducting state. For an efficient transition into the "ON" state, the associated ionization coefficient "α" for the material has to be large. The "α_{Si}" value happens to be larger than "α_{GaAs}". This occurs because the impact ionization threshold energy E_{TH} which depends on the bandgap is lower for silicon. Secondly, the disparity between electron and hole effective masses is lower for silicon as compared to GaAs. As a result, **both** electrons and holes can contribute to avalanche multiplication in Si more effectively than in GaAs. These considerations therefore favor silicon as the material of choice over GaAs.

1.4 RESEARCH OBJECTIVES

The transient behavior of silicon avalanche switches which are used for high-power waveform shaping applications, is studied in this thesis. Numerical simulations have been performed to predict switching currents and examine the repetitive device response. The main research objective is to simulate two-dimensional effects and thereby probe the possibility of current filamentation and the prospects of internal non-uniform current density channels. Such localized current channels and filamentation is known to be destructive and needs to be controlled for useful device performance. However, unless the two-dimensional effects are first understood through numerical simulations and device modeling, one cannot hope to control these effects. The simulations presented in this thesis address this objective.

Two-dimensional effects in devices can arise due to spatial nonuniformities. These could either be due to non-uniformities in the device geometry or due to inhomogeneous doping distributions. Spatially non-uniform traps and defects can also contribute to two-dimensional effects. In this thesis, only the dopant inhomogeneities will be addressed. The resulting two-dimensional current distributions which can lead to filamentation and localized heating, will be evaluated for various doping levels and profiles.

In chapter 2 a brief literature review on semiconductor high power switches is given. This provides some background on previous related work. The silicon avalanche shaper device (SAS) and its operation is also discussed in this chapter. The simulation scheme used for carrying out the numerical modeling and details of the implementation are presented in Chapter 3. Both one-dimensional and two-dimensional modeling schemes are discussed. Finally, the central results obtained from this research will be given in Chapter 4. Discussion of the results including the salient trends observed will also be presented. Finally, summarizing conclusions are presented in Chapter 5. Scope for future work in this area is also discussed.

CHAPTER 2

LITERATURE REVIEW AND DEVICE CONCEPT

2.1 INTRODUCTION

The various technologies for semiconductor based high power switching are given in the following section. This provides an overview of the possible options. A brief discussion of the merits, advantages and drawbacks of the various options is also presented. Next, the silicon avalanche shaper (SAS) devices used in this study are discussed. Their operational principle and potential merits are given. This is followed by a section on the two-dimensional effects and an outline of the research issues and tasks.

2.2 CURRENT SOLID STATE TECHNOLOGIES FOR POWER SWITCHES

In general, present day semiconductor switches for power applications generally fall under two main categories: (1) Metal Oxide Semiconductor (MOS) gate-controlled power devices which include power MOS Field Effect Transistors, MOS controlled thyristors [11,12], and Insulated Gate Bipolar Transistors (IGBTs) [13,14], and (2) Current controlled power devices such as: thyristors, bulk optically controlled switches [15,16], photoconductive avalanche devices [17,18], and bulk ionization wave switches [19,20], and optothyristors [21,22]. The power handling capability of the latter group of devices, however, is much greater than the MOS based devices. As a result, the MOS devices are not particularly useful or relevant in the context of high pulsed power switching. However, for completeness, both classes of devices are briefly discussed below:

(1a) As regards MOS-based switches, power MOSFETs generally have high "on-resistance" values and low current carrying capability of about 20 A/cm^2 [23]. Their power handling limits and voltage blocking levels are also inadequately low and hence are not suitable for high power applications being considered here.

(1b) The MOS controlled thyristors (MCTs) [11,12] represent a hybrid thyristor-MOSFET design. These devices are aimed at providing improvements in the speed of conventional thyristors, to have lower "on-state resistance" and furnish current carrying capabilities substantially larger than those of power MOSFETs. However, the MCTs have the following disadvantages: **(i)** A low blocking voltage capability, **(ii)** Relatively long "turn-on" times, and **(iii)** The inability of the device to lend itself to voltage scaling.

(1c) The IGBTs can sustain currents that are at least an order of magnitude higher than those attainable in power MOSFETs and have much lower "on-state" losses. However, the "turn-off" speeds of the IGBTs are notoriously slow since the excess charge in the transistor structure is removed through recombination. Increasing the turn-off speeds through lifetime control adversely affects the on-state resistance and energy efficiency [24].

(2a) Thyristors [25] rely on minority carrier injection through electrical contacts to transfer into conducting mode based on regenerative feedback between two coupled transistor structures which modulates the internal gain. Though the device is capable of carrying large currents (about 200 A/cm^2) and has a low "on-resistance", its turn-on times are fairly large in the microsecond range. This limitation clearly makes this class of devices unsuited for the fast switching application being considered here. The turn-off process is also slow since carriers are removed mainly through internal recombination processes.

(2b) The bulk optically controlled semiconductor switch (BOSS), which has been a recent development [26], relies on optical triggering at a pre-determined wavelength for switch "closure". The high resistance, hold-off region, of these devices comprises of Cu-doped semi-insulating (SI) GaAs material at a near compensated level. Device turn-off is achieved through an optical excitation pulse at a different wavelength for quenching. Figure 2.1 shows the basic device concept and switching scheme. The device, however, suffers from the "lock-on" phenomena [27] which delays the switch opening time. This phenomena is also known to degrade device reliability and to lead to filamentary instabilities. From a reliability standpoint therefore, this device as such is not a good candidate, unless a mechanism for excessive charge extraction can be designed and built into the device structure. Furthermore, since the BOSS is based on GaAs, it suffers from all of the problems associated with optical triggering as discussed in the next section.

(2c) The optically controlled avalanche switches are similar to the BOSS, but do not use specific dopant levels (such as the Cu_A and Cu_B) for wavelength selective

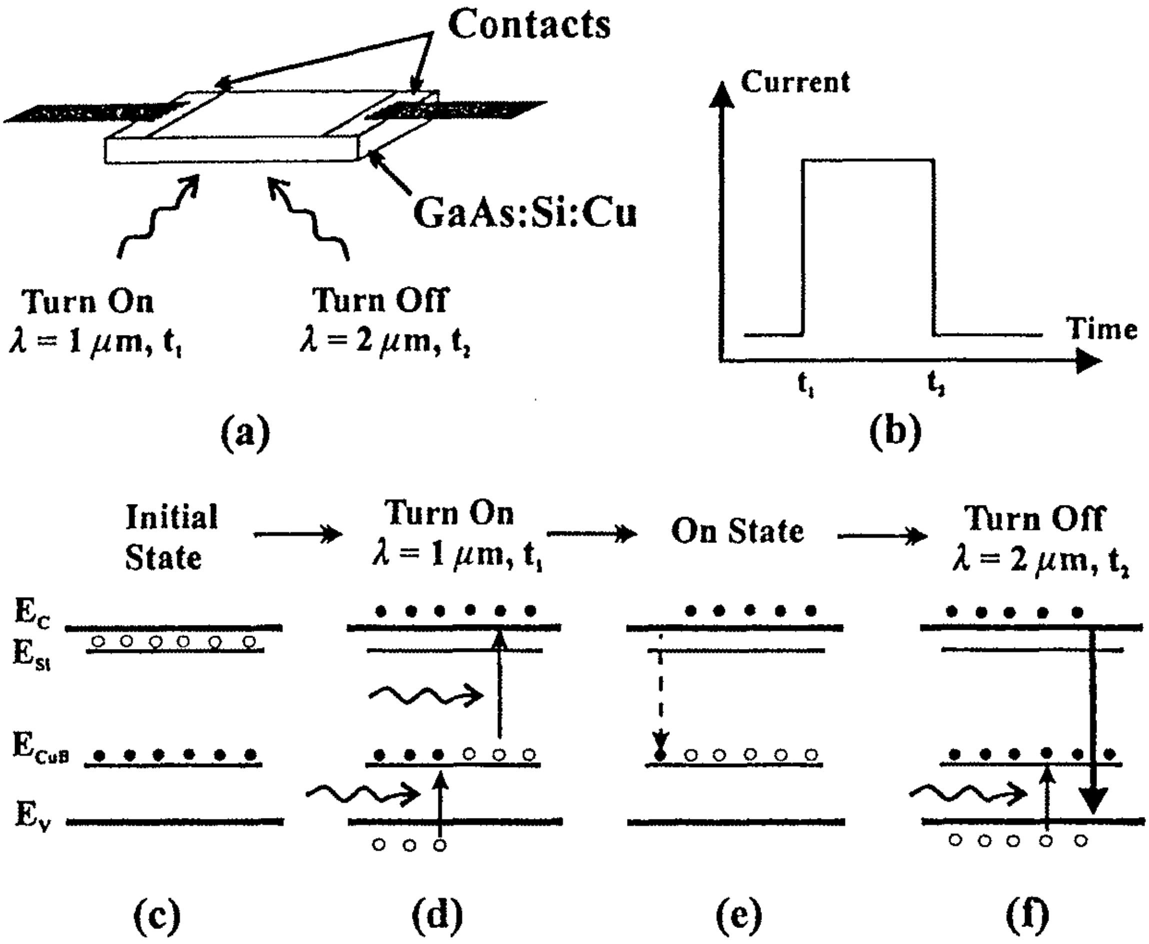

Figure. 2.1. The basic geometry of BOSS swith (a); the resulting current delivered to the load during the BOSS switching cycle (b); the initial high-resistivity state of the material prior to the first laser pulse (c); the optical excitation of electrons from the Cu_B center to the conduction band (d); the slow decay of electrons during the on state (e); and the fast photo-induced quenching of the photoconductivity.

turn-on. However, they too suffer from potential instabilities and "lock-on" problems. Besides, high optical energy is required to trigger and sustain the device in the conductive state to counter the internal recombination losses occurring within these switches. Undesirable and inefficient as it is, this requirement of a high optical level (typically beyond 2 x 10^{-5} Joule) also limits the pulse repetition rate. This occurs because practical laser systems are unable to deliver the requisite high laser energy beyond a frequency of 3 KHz.

(2d) Development of a two terminal solid state switching device technology based on the creation of internal plasma waves have been reported primarily by a Russian group at the Ioffe Institute in St. Petersburg [19,28-30]. This scheme is conceptually simple in design and relatively inexpensive. It is based on silicon material which is easy for fabrication, and does not require any optical excitation which helps reduce the size and circuit complexity. However, this technology has not been extensively evaluated or independently tested outside the Ioffe group.

(2e) Finally, the optothyristor concept is based on using heterostructures formed out of III-V direct bandgap materials. It is an optically triggered thyristor, and represents an attempt to enhance the turn-on speed of the conventional thyristors [21]. However, being optically based, these devices suffer all of the disadvantages of optical triggering and cannot be fashioned into compact "on-chip" integrated elements.

2.3 COMPARISON BETWEEN OPTICAL AND ELECTRICAL TRIGGERING

In the above section, it was mentioned that optically triggered switches have a number of inherent drawbacks. This section briefly outlines the main comparisons between the optical and electrical triggering mechanisms for semiconductor switches. The comparison provides reasons in support of electrically triggered silicon avalanche switches (SAS) and give motivation for the present study.

(i) Complex optical sources or external lasers and photogenerating elements are not required for electrical triggering. This reduces the size of the switching element making it more compact.

(ii) Electrically switched elements can easily be integrated with other electronic components on a chip.

(iii) The optical switches rely on direct band gap semiconductors such as GaAs, InP and other III-V materials. All of these are more expensive to fabricate than the indirect bandgap silicon.

(iv) All of the direct bandgap materials used for optical switches have satellite valleys which leads to intervalley transfer. This phenomena can give rise to internal domain formation and can result in internal instabilities.

(v) The density of the electron-hole plasma inside optically excited switches usually is non-uniform. This arises from the Beer-Lampert law which leads to an exponential distribution of electron-hole pairs internally. This inherent nonuniformity can lead to instabilities, localized current channels or current filamentation.

2.4 THE SAS OPERATIONAL PRINCIPLE

The silicon avalanche shaper switch (SAS) was first proposed and successfully demonstrated by a Russian group [28-30]. Simple qualitative discussions of the SAS operating principle have been given in several papers by Grekhov et al. [19, 28-30] over the years. The concept relies on the generation of a fast propogating electric field and an accompanying ionization wave within the device through the application of a rapid reverse bias across a Silicon p-n junction device. The basic device schematic with the various doping regions are shown in Figure 2.2.

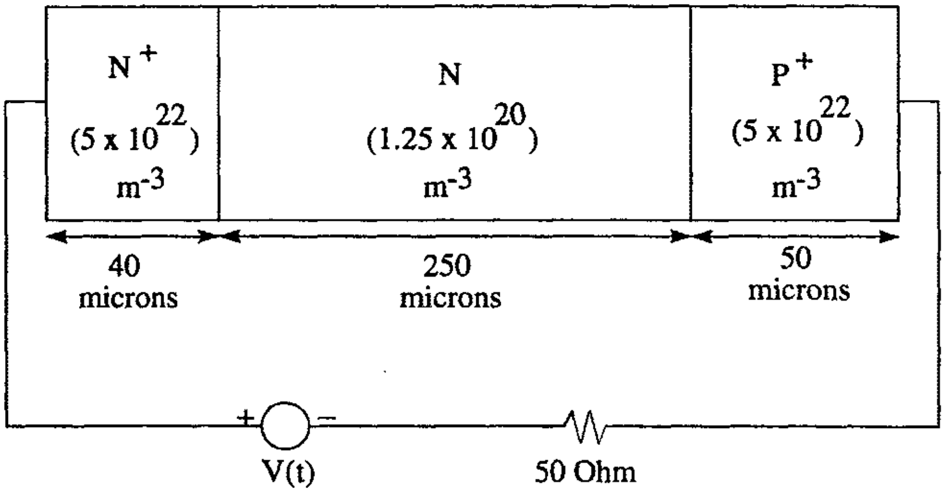

Figure 2.2. Device schematics with various doping regions.

Basically the device has a N^+-N-P^+ structure. The low-doped, near intrinsic "N" region is depleted of carriers during the holdoff phase and supports a large voltage drop. Initially the device is able to hold off an applied voltage and a negligible current flows in the circuit. This corresponds to the "OFF" state. This applied hold-off bias is below the critical breakdown voltage. As soon as the total applied peak bias exceeds the static breakdown voltage, the switch transitions into the "ON" state through the rapid avalanche generation of electron-hole pairs within the high-field regions of the device. The conductivity is therefore enhanced rather quickly, and the switch triggers into the conductive "ON" state. The switch is therefore triggered by an internal avalanche process through either band-to-band or band-to-trap impact ionization. A brief summary of the important sequence of physical events is given below.

(i) The SAS is initially in the non-conducting "OFF" state with a moderate reverse bias across the N^+-N-P^+ structure. The applied voltage is held to a value below the characteristic avalanche voltage of the Si device. This hold-off voltage can, in principle, be varied by changing either the internal doping densities or the device length. Lowering the doping for example, increases the internal electric field, making it possible for the device to withstand an initiation into the avalanche mode. Similarly, increasing the device length also increases the holdoff voltage capability.

(ii) For turn-on, a sharply reverse voltage pulse is applied. As a result, the total voltage across the SAS device then exceeds the breakdown limit. At the higher voltage, a high-field region is created across the P^+-N junction, with field strengths exceeding the critical breakdown value. Impact ionization is thus initiated in a region localized near the P^+-N junction.

(iii) Rapid impact ionization creates a high conductivity region at the P^+-N junction. The electrons and holes thus created through impact ionization, begin to move in opposite directions. The motion of the mobile charge contributes to a current rise.

(iv) Next, the electric field in the highly conduction region begin to collapse as the separation of mobile charge forms an internal polarization field. The electric field in the adjacent non-conducting N-region, however, increases to sustain the overall voltage drop across the device. This increase in the electric field provides the displacement current necessary to maintain exact continuity of the total current across the entire device.

(v) As a result of the above mechanism, the electric field grows starting from the P^+-N junction, towards the N^+ anode side through the N-region in the middle. A propagating electric field wave is thus set up. This propagating field, in turns, creates a travelling impact ionization front, and is responsible for the uniform turn-on of the entire device.

(vi) The current in the SAS device can be turned off by lowering the applied bias to a level below the critical sustaining breakdown voltage. Upon lowering the external voltage, the carriers are removed through a combination of drift flush-out and recombination.

A schematic for the turn-on sequence is shown below in Figure 2.3. The initial field in the N-P$^+$ depletion region is below the critical value for impact ionization. Hence, the carrier concentration and the conductivity remain at a low level. On the application of a large reverse bias, the field increases beyond the critical value, and carrier generation via impact ionization is initiated. This ionization effectively increases the local conductivity, and forces the growth of the electric field in an adjoining low conductivity region. This progressive movement of the electric field away from the junction and into the low conductivity N-region continues, as carriers continually keep getting generated within the N-layer starting from the junction.

2.5 ADVANTAGES AND BENEFITS OF THE SAS DEVICE

Based on the above summary of the SAS operational principle, several key advantages can be identified. These are based on the inherent operating principle and the device physics. The following is a list of important advantages for this SAS-based high power technology:

(i) The elimination of external lasers for triggering and turn-on. This simplifies the complexity of the circuit.

(ii) A natural self-propagation of the electric fields within the device. This facilitates a gradual and more homogeneous turn-on. The potential for instabilities

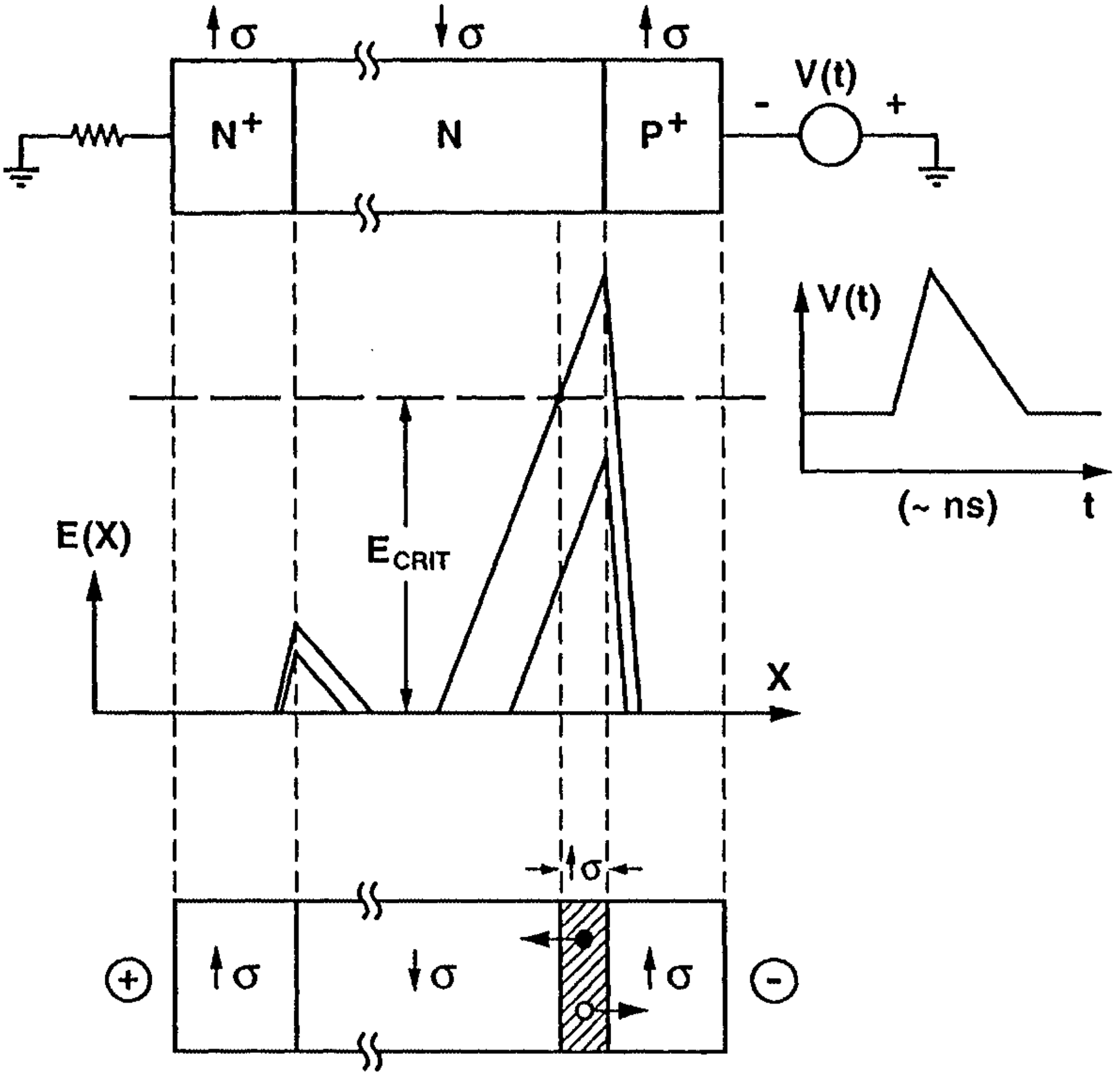

Figure 2.3. Schematic of the turn on sequence.

associated with spatial non-uniformities as with localized charge injection, is thus greatly reduced.

(iii) The application of a rapidly increasing voltage pulse dramatically decreases the likelihood of current filamentation and "micro-channels". As is well known [31], such filamentation is associated with the rapid growth of the electric fields within localized regions of the device due to density fluctuations. This effect is shown in the sketch of Figure 2.4. Due to the formation of a localized region of carrier density within a semiconductor, the fields in the adjacent low conductivity regions "A" and "B" build up. The increased field in turn, causes a further increase in the carrier density through impact ionization and thermal heating. The process builds on itself, and lead to fatal device failure as the high conductivity region rapidly propagates along the micro-pipe. However for an SAS, the field is intentionally made to increase rapidly through an external pulse. Consequently, any localized field increases in regions "A" and "B" brought about by density fluctuations, would quickly be swamped by the rapid increase forced by the external circuit. Besides, rapid increases in the field generated by the external bias, would also be produced in the micropipe regions "C" and "D". Consequently, the entire region comprising of the channels "C", "D" and "AB" would collectively grow, instead of the microchannel "AB" alone. This effectively would prevent localized filamentation.

(iv) Another advantage of this technology is its reliance on Si rather than GaAs. Silicon has the following inherent advantages over GaAs, a material which is often

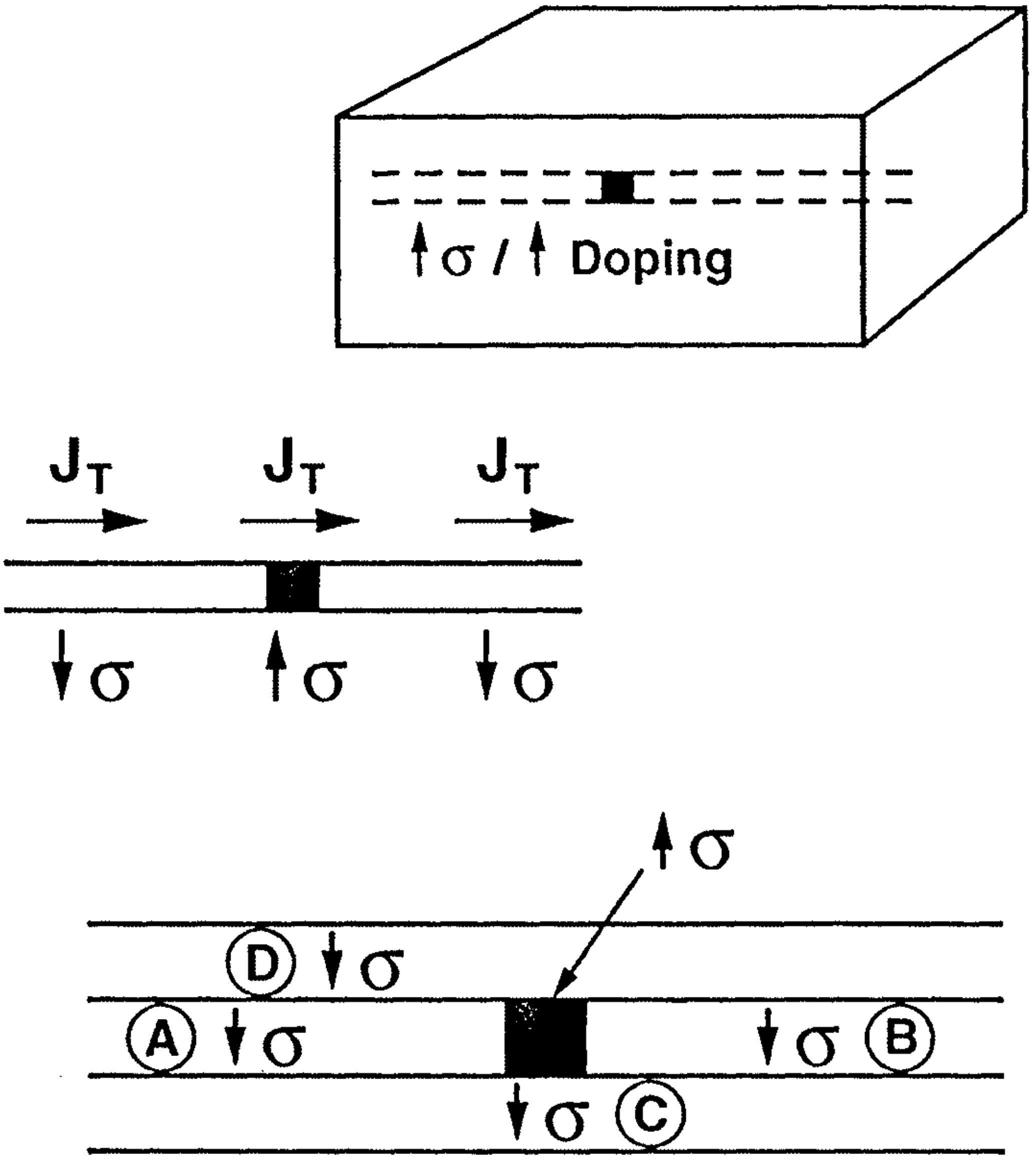

Figure 2.4. Effect of rapid electric field growth on current filamentation.

used in photoconducting switches. The advantages include: **(a)** Ease of fabrication. **(b)** A higher thermal conductivity for better heat dissipation and better protection against thermal runaway. **(c)** A higher carrier saturation velocity which should lead to higher currents and faster turn-on. **(d)** A material system inherently free of Negative Differential Resistance (NDR) effect. As is well known, the NDR effect in GaAs associated with inter-valley transfer gives rise to a potential instability [32].

(v) Furthermore, the SAS by being a p-n junction device, naturally ensures that the regions of high electric field occur within the bulk device and not at the end contacts. As a result, the device circumvents many of the "contact problems" that are associated with other devices. These problems include uncontrolled thermionic emission and carrier tunneling due to high fields at the contact, excessive heating and contact degradation.

(vi) Finally, the SAS also offers the possibility of scaling the hold-off voltage. This could be done by stacking several such devices in series, increasing the size of the central N-region, and by decreasing the doping levels. Therefore there do not appear to be any fundamental limits on the voltage scaling.

2.6 TWO-DIMENSIONAL EFFECTS AND RESEARCH ASPECTS

There are basically two important aspects that are addressed in this thesis research. These two areas are: **(1)** The issue of current filamentation, and **(2)** Determining the role of two-dimensional variations in the doping density on the electrical response and device stability. Both of these aspects are important in determining the reliability and usefulness of the SAS device. For instance, if the doping is not homogeneous across all of the cross-sections of the device, the internal conductivity will also be nonuniform. The nonuniform conductivity can then lead to the formation of localized current channels with the possibility of premature switch turn on.

As is well known, current filamentation arises from spatial non-uniformities across the device cross section, and is basically a two-dimensional effect. Such non-uniformities can arise from any one of the following reasons: **(a)** Doping inhomogeneities (either intentional or accidental) during the processing and fabrication steps. **(b)** The formation of spatially non-uniform traps and defects within the semiconductor. **(c)** The development of non-uniform fields within the semiconductor during device operation which can lead to non-uniform impact ionization with variable charge creation. **(d)** Thermal effects which again can lead to non-uniform carrier generation within the device.

In order to explore these issues, a two-dimensional numerical model has to be developed. Such a model would be a natural extension of the present 1-D simulation scheme. By setting up the 2-D model, it would be possible to then directly examine and analyze the following aspects:

(i) The possibility of current filamentation for a given device geometry, biasing condition, and doping profile. **(ii)** The potential for quenching such deleterious filamentation effects through suitable tailoring of the transverse dopant profiles, or through rapid increases in the applied voltage pulse. It is expected that a fast voltage rise times, corresponding to high "dV/dt" values, should work to quench the spatial non-uniformities. This would be a direct result of a high plasma production within the device which would dilute any existing non-uniformity in the carrier density and electric field.

In the following chapter, the numerical formulation for simulating such two-dimensional effects and to obtain the transient electrical response of the SAS devices is described. The numerical implementation scheme is also discussed.

CHAPTER 3

SIMULATION SCHEME AND NUMERICAL IMPLEMENTATION

3.1 INTRODUCTION

The numerical procedure used for simulations of the SAS devices are discussed in this chapter. The various techniques available for device modeling are first discussed briefly. This is followed by a detailed description of the "Drift-Diffusion" approach. The governing equations and parameters for the silicon SAS device are then in the proceeding section. This is followed by a flowchart of the actual numerical implementation.

3.2 SEMICONDUCTOR SIMULATION APPROACHES

The principal goal of semiconductor device simulations is to determine the behavior of terminal current and device voltage in response to an external driving force. The external stimulus could either be an external bias, an optical excitation, or a thermal perturbation as a function of time. The mathematical model to be used for device analysis should in general, include the dynamics of free carriers within the bulk semiconductor, appropriate boundary conditions between semiconductor sections, the time dependent behavior at the contacts and surfaces, and any applicable thermal exchanges within the semiconductor system. A variety of simulation approaches are available for modeling the transport behavior in semiconductors [33]. Some of the more important techniques are as given below.

(1) The simplest methodology is called the **Kinetic Approach**, since it uses the kinetics of an "average particle" with a simple treatment of collisions to describe it's equation of motion [34]. In it's simple form, the semiconductor band structure is considered parabolic, leading to a constant effective mass, and particle is considered to be non-interacting. This implies low concentrations and non-degenerate Maxwell-Boltzmann internal carrier distributions. Frequency-dependent response is analyzed for the time periods larger than the relaxation time. However, this method can not account for the spatial variations. It is also not very useful since actual devices cannot be characterized in terms of an overall "average particle".

(2) In the **Boltzmann Transport Approach** which represents a higher level of sophistication, a governing integro-differential equation is obtained for the equation of motion for the distribution function $f(r,p,t)$ of particle ensemble [35]. This distribution function f is the probability of finding a particle with the momentum p at a position r at time t. Unlike the previous approach, the Boltzmann Transport Equation (BTE) does incorporate all of the internal scattering effects taking place over time. It is therefore able to correctly describe non-equilibrium, transient effects. However, this method is quite difficult to implement and solve for two reasons. First, the scattering processes cannot easily be calculated and closed form mathematical relationships can not easily be obtained. Second, solution of the BTE integro-differential equation is itself difficult and generally requires intensive computational effort.

(3) In order to correctly simulate semiconductor structures having very small dimensions, for phenomena involving ultrashort time scales, or when the assumptions of the BTE become unacceptable, another approach called the **Monte Carlo Approach** is often used for accuracy [36]. In the stochastic Monte Carlo approach, individual particles are randomly selected and their motion followed in space and time. The average ensemble behavior is subsequently determined by collecting enough information about the particles. The biggest advantage of this method is that, no fitting parameter is required. However, the approach is very intensive computationally since a large number of particles are required to yield reliable statistics. Consequently, this technique will not be used for the present research.

(4) The Boltzmann transport equation, under several assumptions, can be simplified down into a relatively straight-forward expression, known as the Drift-Diffusion equation. For this research, such a **Drift-Diffusion Transport Approach** will be employed given its relative simplicity and modest computational requirements. Furthermore, since the device dimensions in this study are well above the micrometer range and the time scale of interest are relatively large (higher than 10 ns), the more complex approaches will not be necessary. The results obtained from the drift-diffusion scheme are therefore expected to be adequate.

3.3 THE DRIFT-DIFFUSION TRANSPORT APPROACH

The governing Drift-Diffusion equation in one-dimensional form is given as:

$$J=nqv_n+pqv_p-qD_n(\frac{dn}{dx})+qD_p(\frac{dp}{dx}) \qquad (3.1)$$

where J is the current density, n and p are the electron and hole densities, D_n and D_p are the electron and hole diffusion coefficients, v_n and v_p are the electron and hole drift velocities and q is the electronic charge. This equation is derived from the Boltzmann transport equation under the following assumptions:

a) An isotropic and parabolic single band.

b) Inherent assumption of the relaxation time approximation.

c) Absence of degeneracy with no hot carrier effects.

d) A homogeneous collision time. For example, a single energy-independent relaxation time τ_p is assumed for mobility calculations. The carrier mobility μ is then given in terms of the effective mass m^* through the following expression:

$$\mu = \frac{q\,\tau_p}{m^*} \, . \tag{3.2}$$

The validity of the drift-diffusion scheme also requires that the scattering time τ_p be significantly smaller than the simulation time scale of interest.

e) No strong off-equilibrium effects, and

f) An assumption that the length scales for spatial variation of the electric field and impurity concentrations are much longer than the carrier mean free path.

In order to adequately include high frequency and transient effects, the displacement current which is observed as a capacitive effect in the external circuit, needs to be incorporated in the drift-diffusion model. The overall current transport is then an aggregate of particle current and displacement current and is given as:

$$J=nqv_n+pqv_p-qD_n(\frac{dn}{dx})+qD_p(\frac{dp}{dx})+\epsilon\frac{dE}{dt} \qquad (3.3)$$

where E is the electric field and ε is the permitivity of material. The permitivity was taken to be constant since its dependence on the free carrier density is negligible. The details of the underlying transport model used in this research and it's numerical implementation are presented in the following section. In summary, it may be noted that the model developed for the study of the SAS devices has the following salient features:

- It is based on the drift-diffusion approach.
- It explicitly solves for the two-dimensional distributions of the internal electric fields and carrier densities.
- It yields the self-consistent transient analysis, as well as the final steady-state response.
- The model is bipolar and can treat both electron and hole transport.
- An important component of the model consists of rate equations which describe the transient dynamics of free-carrier generation, trapping and recombination.
- An external circuit has been incorporated in the model.
- The model takes into account the distributed capacitance of the device in the form of an internal displacement current.

- An added feature of the model is the inclusion of impact ionization at high electric fields. This mechanism is very important since it is at the heart of the switch "turn-on" process.
- The numerical implementation includes heat generation within the device. A one-dimensional diffusive heat flow model is included, and changes in the transport parameters with any resulting temperature rise taken into account.
- Finally, carrier injection at the two contacts was implemented based on the thermionic emission model which uses the Richardson coefficient A^*. A value of 80 $A/cm^2/K^2$ was assumed for A^*. The barrier heights at each contact were assumed fixed at a value of 0.5 eV independent of the current density.

3.4 SEMICONDUCTOR EQUATIONS AND MATERIAL PARAMETERS

The 1D Drift-diffusion equation (3.3) which includes the displacement current is the basic equation for charge transport. Changes in the free carrier densities n(x,t) and p(x,t) in the absence of charge flow and spatial movements are described in terms of the following rate equations:

$$\frac{dn}{dt} = e_n N_{D0} - n N_D^+ \sigma_n v_{th}^n - \frac{(np - n_{ie})}{\tau_p (n + n_{ie}) + \tau_n (p + n_{ie})} - (C_p p + C_n n)(np - n_{ie}^2) + \alpha_n n |v_n| \tag{3.4a}$$

$$\frac{dp}{dt} = e_p N_{A0} - p N_A^{+} \sigma_p v_{th}^{p} - \frac{(np - n_{ie})}{\tau_p (n + n_{ie}) + \tau_n (p + n_{ie})} + (C_p p + C_n n)(np - n_{ie}^2) + \alpha_p p |v_p| \qquad (3.4b)$$

where e_n and e_p are the emission coefficients, σ_n and σ_p are the capture cross sections, N_{D0} and N_{A0} are the unionized dopant concentrations and N_D^+ and N_A^- are ionized donor and acceptor concentrations. C_n and C_p are the Auger recombination coefficients, α_n and α_p are the band-to-band impact ionization coefficients, v_{th}^n and v_{th}^p are the thermal velocities and n_{ie} is the intrinsic carrier density. The first two terms of the equations (3.4a) and (3.4b) are the trap to band thermal generation and recombination, respectively, while the next two terms correspond to the Shockley-Reed-Hall [37] and Auger recombination-generation [38] processes. The second last term of (3.4a) and last term of (3.4b) are the band-to-band impact ionization terms for electrons and holes, respectively. The lifetimes τ_n and τ_p of electrons and holes, for the SHR process depend on the doping level, and have been described by the Scharfetter relations [38]:

$$\tau_n = \frac{\tau_{n0}}{1 + \left(\frac{N_D + N_A}{N_n^{SRH}}\right)^{\gamma_{n}}} \qquad (3.5a)$$

for electrons, and for holes the lifetime is:

$$\tau_p = \frac{\tau_{p0}}{1+(\frac{N_D+N_A}{N_p^{SRH}})^{\gamma_{ps}}} \tag{3.5b}$$

where N_D and N_A are the donor and acceptor concentrations, and N^{SRH}, and $\gamma_{ns,ps}$ are some constant parameters. The appropriate values of parameters for Si used in this research are given in Table I. The rate coefficients for band to band Auger recombination in Si are similarly tabulated.

The impact ionization coefficients α_n and α_p given in the rate equation, determine the strength of the impact ionization process and are in general field-dependent. An empirical relation of the electron and hole impact ionization rates is used in this research. This relation is given by [38]:

$$\alpha_n = a_n \exp(-\frac{b_n}{|E|}) \text{ , } and \ \alpha_p = a_p \exp(-\frac{b_p}{|E|}) \tag{3.6}$$

In the above, a_n, b_n, a_p, and b_p are fitting parameters, and have been given in the Table II. The velocities $v_n(x)$ and $v_p(x)$ needed for the calculations in (3.3), are usually obtained in terms of the local electric field "E(x)". At low values, the velocity is linearly related to the local electric field. However, at larger fields non-linear effects become dominant, and the velocity is modeled in terms of a field-dependent mobility. In this framework,

Table I. List of the parameters used in the research.

Parameters	for electrons	for holes
$\sigma_{n,p}$ (m^{-2})	$2x10^{-19}$	$2x10^{-19}$
$\tau_{no,po}$(sec)	$5x10^{-9}$	$1x10^{-9}$
$C_{n,p}$ (m^6/sec)	$2.8x10^{-37}$	$9.9x10^{-38}$
$\gamma_{ns,ps}$	0.3	0.3
$N_{n,p}^{RSH}$ (m)	$3x10^{-23}$	$3x10^{-23}$
$V_{sn,sp}$ (m/sec)	$2x10^5$	$1x10^5$
$\beta_{n,p}$	0.2	0.2
$E_{d,a}$ (meV)	45	45
n_i (m^{-3})	1.6	1.6
ρ (kg/m^3)	$3.166x10^3$	$3.166x10^3$
C_p (J/mol/K)	36	36

the low-field drift mobility is modeled by the Caughey-Thomas equation [37]:

$$\mu_{n,p} = \mu_{n,p}^{\min} + \frac{\mu_{n,p}^{\delta}}{1+\left(\frac{N_D+N_A}{N_{n,p}^{\mu}}\right)^{\gamma_{n,p}}}\left(\frac{T}{300K}\right) \tag{3.7}$$

Table II. Fitting parameter for the Caughey-Thomas equation.

Material	$\mu_{n,p}^{\delta}$ (cm^2/Vs)	$\mu_{n,p}^{\min}$ (cm^2/Vs)	N_{ref} (cm^{-3})	γ
N: Si	947	0	$1.94\text{x}10^{17}$	0.61
P: Si	108.1	15.9	$1.76\text{x}10^{19}$	0.31

Based on experimental Hall mobility data obtained from Si samples at 300 K, the parameters given in Table II were obtained as the best fits to the Caughey-Thomas equation.

At high electric fields, the drift velocity v_n and v_p of the carrier begins to saturate. This can be described by the following field dependent mobility model:

$$\mu_n^E = \mu_n[\frac{1}{1+(\frac{E\mu_n}{v_{sn}})^{\beta_n}}]^{1/\beta_n} \quad and \quad \mu_p^E = \mu_p[\frac{1}{1+(\frac{E\mu_p}{v_{sp}})^{\beta_p}}]^{1/\beta_p} \tag{3.8a}$$

and,

$$\overline{v_n} = \mu_n^E \, \overline{E} \quad and \quad \overline{v_p} = \mu_n^E \, \overline{E} \tag{3.8b}$$

for electrons and holes, respectively. Where $v_{sn,sp}$ is the drift saturation velocity of carriers, $\beta_{n,p}$ are constant parameters, and μ_n^E and μ_p^E are the high field electron and hole mobilities respectively.

Since Si exhibits directional anisotropy, directionally dependent effective masses need to be used. Cyclotron resonance measurement on Si has yielded a longitudinal effective mass $m^*_L = 0.19\ m_o$ and a transverse effective mass m^*_T of $0.916\ m_o$ [39]. The effective mass tensor and conductivity masses for Si can be obtained based on the above values, and have been used in this research. The energy band gap E_g of silicon, like other semiconducting materials, is a function of temperature. The following relation is used here for the energy gap as a function of the device temperature T [37]:

$$E_g(T)=3-3.3*10^{-4}(T-300)\ eV. \tag{3.9}$$

In order to compute the occupancy and ionized density of the donors and acceptors as given in (3.3), the corresponding energy levels need to be specified. For Si these were chosen to be located at 45 meV and 45 meV from the conduction and valance bands.

This corresponds to experimentally measured values for the phosphorus and aluminum dopant impurities in silicon as shown in Figure 3.1.

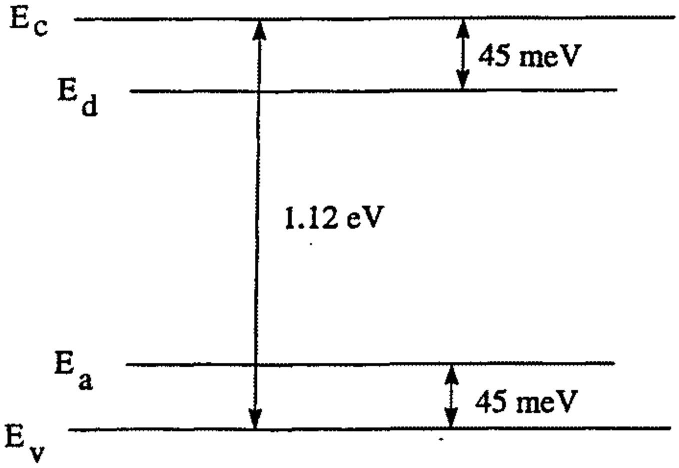

Figure 3.1. Energy band diagram representing donor and acceptor levels.

Finally, in order to describe the internal device temperature T(x,t) of the simulated Si devices, a one-dimensional diffusive heat flow equation has been used. The density ρ, thermal conductivity k, and specific heat capacity Cp have all been assumed to be fixed constants, independent of the temperature. The heat flow equation is as:

$$k \frac{\partial^2 T(x,t)}{\partial x^2} + g(x,t) = \rho C_p \frac{\partial T(x,t)}{\partial t} . \qquad (3.10)$$

Here g(x,t) is the power generation rate per unit volume. The constant values for the above equation are given in Table I. For numerical implementation, the above equation was discretized and solved using the implicit Crank-Nicholson technique.

The effect of a changing temperature appears in the following parameters: saturation velocity, mobility, life time and emission coefficients of carriers. The appropriate equations are as given below [37]:

$$\mu_{n,p} = \mu_{n,p\ RT}\left(\frac{T}{T_{RT}}\right) \tag{3.11a}$$

$$v_{s_{n,p}} = \frac{v_{s_{n,p}\ RT}}{1+0.8\exp\left(\frac{T}{T_{RT}}\right)} \tag{3.11b}$$

$$\tau_{n,p} = \tau_{n,p\ RT}\left(\frac{T}{T_{RT}}\right) \tag{3.11c}$$

$$e_{n,p} = e_{n,p\ RT}\left(\frac{T}{T_{RT}}\right)^2 \exp\left[\frac{-E_{DA}}{kT}\left(1-\frac{T}{T_{RT}}\right)\right] \tag{3.11d}$$

where T is the operating temperature and T_{RT} is the room temperature equal to 300K (subscript RT in the above equations stands for values at room temperature). In the last equation, the effect of temperature on all the associated terms need to be included.

Finally, carrier flow across the anode and cathode contacts between the semiconductor and the metal were treated on the basis of thermionic emission theory. In this approach, the metal-semiconductor interface is viewed as an impediment to current flow, and a Schottky barrier is assumed to exist at the boundary. This impediment is created by the formation of internal electric fields which arise from charge redistribution between the metal and the semiconductor. This redistribution is necessary for attaining thermodynamic equilibrium. The characteristic Schottky barrier to electronic flow from the metal into the conduction band of the semiconductor was taken to be 0.5 eV. This value was assumed to be independent of the current density. Based on the thermionic emission theory [40], the electron and hole currents $I_{n,p}{}^{B}$ at the two boundaries can be evaluated as:

$$I_{n,p}^{B} = A\ A^{*}\ T^{2} \exp[-\frac{\phi_{n,p}^{B}}{k_B\ T}]\ [\frac{n,p^{B}}{n,p_{eq}^{B}} - 1\ ]\ , \tag{3.12}$$

where n,p^{B} are the electron and hole concentrations on the semiconductor side of the boundary, $n,p_{eq}{}^{B}$ are the equilibrium values under unbiased conditions, k_B is the Boltzmann constant, T the temperature in Kelvin, and $\phi_{n,p}{}^{B}$ the carrier barrier heights. Equation (3.12) uses an effective Richardson constant A^{*}, with "A" being the cross sectional area. For the SAS simulations, the following values were chosen: $A^* = 80$ $A/cm^2/K^2$ and $A = 2 \times 10^{-2}\ cm^2$.

3.5 SEMICONDUCTOR MODEL IMPLEMENTATION AND SIMULATION SCHEME

For numerical implementation of the mathematical device model described in the proceeding section, the SAS device was spatially divided into "N" boxes each with a finite spatial extent as shown in Figure 3.2. The density of free carriers, ionized/unionized donors and acceptors, the average internal electric field, and device temperature were all represented by discrete values at the center of each box. Thus the above parameters were assumed to be fixed within each box, but to vary from box to box during each time step of the simulation.

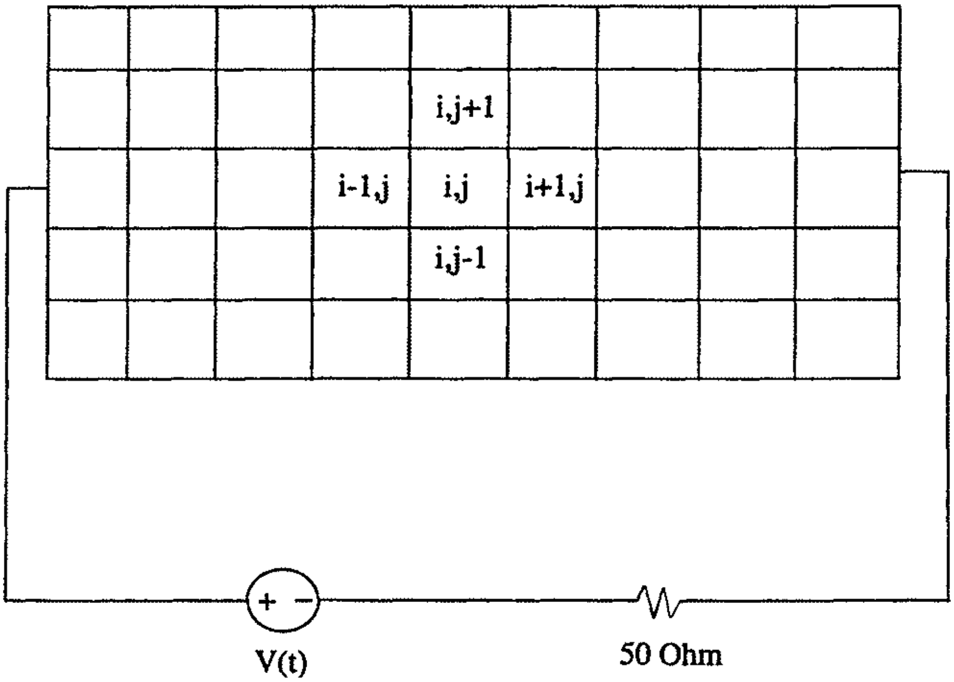

Figure 3.2. Circuit diagram of the device used for simulation.

The temporal scale was also discretized into time intervals of magnitude Δt. This time step Δt was chosen to satisfy the requirement of being greater than both the relaxation time and the internal collision times. In order to obtain numerical stability of the space-time discretization, the well known "Courant-Fredericks-Lewy" inequality condition [41] was used to put a constraint on the upper limit on the value of the time step Δt. The limit for the maximum value of Δt is related to the size of the box Δx and the maximum carrier drift velocity v_{max} as:

$$\Delta t_{max} \leq \frac{\Delta x}{2 v_{max}} \; . \tag{3.13}$$

The silicon SAS device structure used for the simulation was a N^+-N-P^+ diode with dimensions of 40μm, 250μm and 50μm, respectively. A total of 136 discretized boxes along the longitudinal and 10 boxes along the transverse direction were chosen for the device simulations. A simple step-by-step outline of the numerical implementation of the overall simulation scheme is described next. For clarity and ease of discussion, only the one-dimensional equations have been given. However based on the outline and discretized mathematical equations provided below, the scheme can easily be extended for two-dimensional analysis. In order to do so, additional terms corresponding to spatial variations along the "y-direction" would need to be incorporated. The modifications necessary for the 2D analysis are indicated in the following section. The time dependent 1D device simulation procedure used for this study is as follows.

(a) Initialization of the value of the following variables in each of the boxes

- electric field E[i] equal to zero,
- electron and hole velocity $v_{n,p}$[i] equal to zero,
- temperature T[i] equal to the room temperature,
- electron and hole density n[i] and p[i] corresponding to their impurity doping using charge neutrality and equilibrium conditions,
- Ionized and unionized dopant concentrations N_{D0}[i], N_D^+[i], N_{A0}[i], N_A^-[i] corresponding to the impurity doping concentrations.

(b) Initialization of the following parameters in each box

- mobilities of the electron and holes using equation 3.7 and 3.8,
- emission coefficients for electron and hole using the following equilibrium condition:

$$\frac{d(n,p)}{dt} = e_{(n,p)} N_{D_0 A_0} - \sigma N_{D,A}^{+,-} v_{th} (n,p) = 0, \qquad (3.14a)$$

$$e_{(n,p)} = \frac{\sigma N_{D,A}^{+,-} v_{th} (n,p)}{N_{D_0 A_0}}. \qquad (3.14b)$$

- diffusion coefficients for electron and holes using the Einstien relationship

$$D_{(n,p)} = \frac{kT}{q} \mu_{(n,p)} \qquad (3.14c)$$

(c) This and the following calculations up to step (j) were carried out for a small time step Δt chosen in accordance with the CFL condition. Changes in electric field within the ith box were calculated and updated over this time step as:

$$\Delta E_i = \frac{\Delta t}{\epsilon}[J - n_i q v_{ni} - p_i q v_{pi} + qD_{ni}\frac{\Delta n_i}{\Delta x} - qD_{pi}\frac{\Delta p_i}{\Delta x}] \quad \textit{and,} \tag{3.15a}$$

$$E_i^{new} = E_i + \Delta E_i \tag{3.15b}$$

where $J = \frac{V_o - V_d}{RA}$ is the total circuit current, V_0 = applied voltage, and V_d = device voltage at time t, "R" the external resistance, and "A" the area of device. The corresponding values of the field dependent carrier velocities within each simulation box were obtained next.

(d) Changes in the holes and electrons densities in each box were calculated during Δt as:

$$\Delta n_i = T_{n1} + T_{n2} + T_{n3} + T_{n4} + T_{n5} + T_{n6} \tag{3.16a}$$

where

$$T_{n1} = -n_i|v_{ni}|\frac{\Delta t}{\Delta x} + n_{i+1}|v_{n(i+1)}|\frac{\Delta t}{\Delta x} + n_{i-1}|v_{n(i-1)}|\frac{\Delta t}{\Delta x}, \tag{3.16b}$$

$$(if\ E_{i+1}>0) \quad (if\ E_{i-1}<0)$$

$$T_{n2} = \frac{(D_{ni}+D_{n(i+1)})}{2}(n_{i+1}-n_i)\frac{\Delta t}{(\Delta x)^2}+\frac{(D_{ni}+D_{n(i-1)})}{2}(n_{i-1}-n_i)\frac{\Delta t}{(\Delta x)^2}, \tag{3.16c}$$

$$T_{n3} = (e_{ni}N_{D_0i}-n_iN_D{}^+(i)\sigma_n v_{th})\Delta t, \tag{3.16d}$$

$$T_{n4} = -\frac{(n_ip_i-n_{ie}{}^2)\Delta t}{\tau_p(n_i+n_{ie})+\tau_n(p_i+n_{ie})}, \tag{3.16e}$$

$$T_{n5} = -(C_pp_i+C_nn_i)(n_ip_i-n_{ie}{}^2)\Delta t, \quad and, \tag{3.16f}$$

$$T_{n6} = \alpha_n n_i|v_n|\Delta t + \alpha_n' n_i|v_n|\Delta t. \tag{3.16g}$$

for electrons, and

$$\Delta p_i = T_{p1}+T_{p2}+T_{p3}+T_{p4}+T_{p5} \tag{3.17a}$$

where

$$T_{p1} = -p_i|v_{pi}|\frac{\Delta t}{\Delta x}+p_{(i+1)}|v_{p(i+1)}|\frac{\Delta t}{\Delta x}+p_{(i-1)}|v_{n(i-1)}|\frac{\Delta t}{\Delta x}, \tag{3.17b}$$

$$(\mathit{if}\ E_{i+1}<0) \quad (\mathit{if}\ E_{i-1}>0)$$

$$T_{p2} = \frac{(D_{pi}+D_{p(i+1)})}{2}(p_{i+1}-p_i)\frac{\Delta t}{(\Delta x)^2}+\frac{(D_{pi}+D_{p(i-1)})}{2}(p_{i-1}-p_i)\frac{\Delta t}{(\Delta x)^2}, \tag{3.17c}$$

$$T_{p3} = (e_{pi}N_{A_0i}-p_iN_{Ai}^{-}\sigma_p v_{th})\Delta t, \tag{3.17d}$$

$$T_{p4} = -\frac{(n_ip_i-n_{ie}^2)\Delta t}{\tau_p(n_i+n_{ie})+\tau_n(p_i+n_{ie})}, \ \mathit{and}, \tag{3.17e}$$

$$T_{p5} = -(C_pp_i+C_nn_i)(n_ip_i-n_{ie}^2)\Delta t. \tag{3.17f}$$

for holes. Terms T_{n2} and T_{p2} do not contain diffusion beyond the first and last box. The changes in the concentration were due to combined drift, diffusion, recombination, and impact ionization processes.

(e) Changes in the density of ionized dopants during the time interval Δt were calculated as:

$$\Delta N_{Di}^{+} = (e_nN_{D_0i} - n_iN_D^{+}\sigma_n v_{th})\Delta t, \quad \mathit{and} \tag{3.18a}$$

$$\Delta N_{Ai}^{-} = (e_pN_{A_0i} - p_iN_A^{-}\sigma_p v_{th})\Delta t. \tag{3.18b}$$

for electron and holes, respectively. The calculation for changes in neutral dopant density were as:

$$\Delta N_{D_{d}i} = -\Delta N_{Di}^{+} \quad and \quad \Delta N_{A_{d}i} = -\Delta N_{Ai}^{-}. \tag{3.19}$$

(f) It was assumed that there was no recombination at the contact surface. The total number of injected particle was the algebraic sum of particles coming in and going out due to the thermionic emission process. The net current at the boundary as given by equation (3.12) was used as the basis for updating the carrier densities within the first and last simulation boxes. Apart from the net inflows/outflows across the boundaries as given by (3.12), the internal carrier drift and diffusion processes were also taken into account.

(g) Power generation per unit volume terms Gen$_i$ for each box is calculated as:

$$Gen_i = E_i J_i \tag{3.21}$$

(h) Increases in the temperature of each box due to energy generation and heat diffusion was given in terms of the following discretized equation:

$$\Delta T_i = \frac{Gen_i \, \Delta t}{\rho C_p} + \frac{\Delta t \, K}{\rho C_p (\Delta x)^2} [T_{i+1} - 2T_i + T_{i-1}] \quad and \tag{3.22a}$$

$$T_i^{new} = \Delta T + T_i \tag{3.22b}$$

where $\rho \equiv$ density of Si, $C_p \equiv$ heat capacity, and $K \equiv$ the thermal conductivity of Si.

(i) Boundary conditions for temperature variation at the top surface and the bottom substrate layer are taken to be constant and equal to the ambient temperature of 300 K.

(j) The device voltage and circuit current were calculated at each time step as:

$$|V_d| = \sum_{i=0}^{N} E_i dx \tag{3.23}$$

$$I = \frac{V_0 - V_d}{R} \tag{3.24}$$

and saved as an output. The above steps represented a repetitive block covering the device simulation over a time step Δt. Following the above steps, the time was incremented as $t = t + \Delta t$, and the applied voltage updated according to the chosen input voltage pulse. These calculations are repeated again starting from step (c) until the time was greater than the desired simulation time.

(k) Finally, the electric field and carrier densities profiles, circuit currents and device voltages were saved at predetermined time instants of the simulation for eventual output.

3.6 MODIFICATIONS FOR IMPLEMENTING THE 2D SEMICONDUCTOR MODEL

This section briefly describes the modifications necessary for implementing the more complex 2D simulation model. The 1D model described in detail in the proceeding section was used as the basis for developing the 2D equations. Basically in the 2D case, the current density becomes a vector quantity with components along the longitudinal "x-direction" and the transverse "y-direction". However, the form of the drift-diffusion equation (3.3) remains the same, and so the relation can still be used to express the individual x- and y-components of the total internal current. Thus:

$$J_x = nqv_{nx} + pqv_{px} - qD_n\left(\frac{dn}{dx}\right) + qD_p\left(\frac{dp}{dx}\right) + \epsilon\frac{dE_x}{dt} \ , \tag{3.25a}$$

$$J_y = nqv_{ny} + pqv_{py} - qD_n\left(\frac{dn}{dy}\right) + qD_p\left(\frac{dp}{dy}\right) + \epsilon\frac{dE_y}{dt} \ , \tag{3.25b}$$

where J_x and J_y are the components of the current density, $E_{x,y}$ are the two components of the internal electric field, while v_{nxy} and v_{pxy} are the components of the electron and hole drift velocities, respectively. The result is that the set of scalar equations 3.3-3.13 remain valid for describing the current components along each of the two constituent directions, and can still be used for the 2D case. However, equations 3.14 and 3.15 need slight modification. For instance, changes in the electric field ΔE_x^{ij} at any node (i,j) within the simulation region have to satisfy the requirement of producing a constant sum along the x-direction regardless of the transverse location "j" of the node. This arises from the requirement that the integral of E_x along any path parallel to the longitudinal x-axis must always equal the device voltage regardless of its transverse location. Furthermore, the y-component of the total current flowing within the device has to equal zero regardless of the x-location, since the device has no contacts or an applied bias along the transverse direction. These considerations lead to a slight complexity in the evaluation of the time dependent variations of the electric field within the device. Details for updating the electric field ΔE_x^{ij} are given below. The corresponding equation for updating the y-field component has the same form, with the y-variables replacing all the corresponding x-components.

For concreteness, the derivation given below assumes that the total device is divided into a uniformly spaced grid of N_i points along the x-direction and N_j points along the transverse y-direction. Conservation of total current requires that the current I_{tot}^{xj} along the x-direction be constant for any grid point (i,j). Thus:

$$I_{TOT}^{xj} = J_{cond}^{x\,ij}(\Delta A) + \epsilon \frac{\partial E_x^{ij}}{\partial t}(\Delta A) \ , \tag{3.26}$$

where J_{cond}^{xij} represents the conduction current along the x-direction at the grid point (i,j), E_x^{ij} is the associated electric field, and ΔA the differential area of the "longitudinal tube" located at "j" parallel to the x-axis. Based on (3.26), the change in the E_x component is given as:

$$\Delta E_x^{ij} = [I_{TOT}^{xj} - J_{cond}^{xij}(\Delta A)]\frac{\Delta t}{\epsilon(\Delta A)} \ . \tag{3.27}$$

The total voltage across the longitudinal tube given by a summation of the electric fields E_x at each grid point in the discretized implementation, equals the bias across the device. This bias has to be independent of the y-location, due to the presence of uniform metallic contacts across each of the two end faces of the device. Hence, the summation of ΔE_x^{ij} along the path of the longitudinal tube at "j" must be a constant, independent of the "j" coordinate. This leads to:

$$\sum_{i=1}^{N_i} \Delta E_x^{ij} = \frac{\Delta t}{\epsilon}[N_i I_{TOT}^{xj} - (\Delta A)\sum_{i=1}^{N_i} J_{cond}^{xij}] \ . \tag{3.28}$$

For convenience, the terms on the right side of equation (3.28) are denoted by "K". Thus:

$$N_i I_{TOT}^{xj} - (\Delta A)\sum_{i=1}^{N_i} J_{cond}^{xij} \equiv K \ . \tag{3.29}$$

The total circuit current given by I_{tot}^x equals the sum of the contributions of the currents in each of the longitudinal tubes. These tubes represent parallel conduction paths spread across the entire transverse dimension of the device. Thus, the total circuit current I_{tot}^x can be obtained as:

$$I_{TOT}^{x} = \sum_{j=1}^{N_j} I_{TOT}^{x\,j} = \frac{V_o - V_d}{R} \ . \tag{3.30}$$

Using equation (3.29) in (3.30) to replace I_{tot}^{xj} leads to:

$$\frac{V_o - V_d}{R} = \frac{K}{N_i} N_j + \frac{(\Delta A)}{N_i} \sum_{j=1}^{N_j} \sum_{i=1}^{N_i} J_{cond}^{x\,ij} \ , \tag{3.31}$$

which yields the following expression for the constant "K":

$$K = (\frac{V_o - V_d}{R}) \frac{N_i}{N_j} - \frac{(\Delta A)}{N_j} \sum_{j=1}^{N_j} \sum_{i=1}^{N_i} J_{cond}^{x\,ij} \equiv N_i I_{TOT}^{x\,j} - (\Delta A) \sum_{i=1}^{N_i} J_{cond}^{x\,ij} \ . \tag{3.32}$$

Replacing the above relation for "K" in equation (3.29) yield:

$$I_{TOT}^{x\,j} = (\frac{V_o - V_d}{R}) \frac{1}{N_j} - \frac{(\Delta A)}{N_i N_j} \sum_{j=1}^{N_j} \sum_{i=1}^{N_i} J_{cond}^{x\,ij} + \frac{(\Delta A)}{N_i} \sum_{i=1}^{N_i} J_{cond}^{x\,ij} \ . \tag{3.33}$$

Finally, time dependent variations of the electric field along the x-direction in the discretized 2D case, are obtained by using (3.33) back into (3.27). The final result is the following:

$$\Delta E_x^{ij} = \frac{\Delta t}{(\Delta A)\epsilon}[(\frac{V_o - V_d}{R})\frac{1}{N_j} - \frac{(\Delta A)}{N_i N_j}\sum_{j=1}^{N_j}\sum_{i=1}^{N_i} J_{cond}^{x\,ij} + \frac{(\Delta A)}{N_i}\sum_{i=1}^{N_i} J_{cond}^{x\,ij} - (\Delta A) J_{cond}^{x\,ij}] \ . \tag{3.34}$$

The y-components of the electric field and current can be treated in the exactly the same manner as given above. The final equations will be similar to (3.33) and (3.34) with $V_o = 0$ due to the absence of an external bias. Also, the x-components being replaced by the corresponding y-variables. Finally, equations (3.16) and (3.17) given previously for the 1D model, have to be expanded to allow for carrier flows along the transverse y-direction. Thus, for example, additional terms similar to T_{n1} and T_{n2} are required to account for the variations along y. Expressions for these additional terms can easily be obtained and have not been given here for simplicity.

CHAPTER 4

RESULTS AND DISCUSSION

4.1 INTRODUCTION

This chapter provides all of the numerical simulation results that were obtained for the SAS device. The simulations were carried out to predict and gauge the electrical response characteristics. Both the one-dimensional (1D) and two-dimensional (2D) implementations based on the semiconductor models discussed in the preceding chapter were used for this purpose. The primary objectives of the numerical simulations were: (i) comparisons between the results obtained from the one-dimensional simulations and the more accurate predictions of the two-dimensional model. Differences between the two serve to highlight the potential shortcomings of the simpler 1D approach, and indicate the regimes over which two dimensional modeling becomes necessary. (ii) Quantitative study of the 2D nature of the internal electrical field distributions and its impact on the electrical response characteristics of the device. (iii) Assessment of the role of doping density variations along the transverse direction on the device performance. Such variations in the transverse direction are important and should be carefully considered in a real SAS device for the following reasons: (a) The variations may occur naturally in the semiconductor due to out-diffusion of the dopant species after fabrication, (b) they may arise due to the formation of an internal radial doping profile having azimuthal symmetry due to ion-implantation or diffusion during processing, or (c) the variations may be deliberate and intended to provide a means of tailoring the doping profile for optimizing the overall electrical characteristics.

The results obtained for the SAS device have been analyzed and discussed in this chapter. Salient features of the electrical characteristics and the primary effects of two-dimensional doping variations as revealed by the simulations have also been examined. Based on the results given in this chapter, a set of appropriate conclusions will be presented and the scope of future research in this area discussed in the following chapter.

4.2 ONE-DIMENSIONAL RESULTS AND ANALYSIS

The numerical implementation of the one-dimensional drift-diffusion model discussed in chapter 3 was used initially to obtain the transient response of the SAS device. The SAS device was assumed to comprise of piecewise, uniformly doped N^+-N-P^+ Si material with doping concentrations of $N_D = 5 \times 10^{16}$ cm^{-3} and $N_D = 10^{14}$ cm^{-3} for the n-sides, and $N_A = 5 \times 10^{16}$ cm^{-3} for the P^+ region. As a result of the 1D nature of these simulations, possible non-uniformities and inhomogeneities in the doping along the transverse direction were completely neglected. A simple "idealized" device was therefore being assumed for purposes of these simulations. For conducting realistic simulations, the SAS device was assumed to be embedded in a simple circuit consisting of a 50 Ohm resistor in series with an independent voltage source. The simulated circuit for the SAS is shown in Figure 4.1. The device area was 2×10^{-2} cm^2 and the operating temperature was assumed to be 300 K. For simplicity, a periodic "saw-tooth" type voltage waveform was assumed to be associated with the voltage source. Such a waveshape is similar to that actually used in preliminary experimental tests so far [42]. Quantitative details of the applied voltage are shown in Figure 4.2. It comprises of an initial 2 ns, 600 Volt turn-on ramp. The voltage was then assumed to be held fixed at 600 Volts until 15 ns to allow a steady state to be reached within the active device. Such a steady state represents the "steady OFF state" during which the current conduction is negligible. As this applied voltage of 600 Volts is below the breakdown level, the device merely "holds off" the voltage without progressing into a high conductive state. Following the initialization into a "steady OFF state", the voltage was linearly increased from 600 Volts to 1600 Volts over a 5 ns period. These values are again typical of those used in actual experiments. This voltage increase is intended to take the device into its conducting state beyond hold off and initiate current flow through the circuit. Internal impact ionization is also expected to begin following the application of this high voltage. Finally, as seen from Figure 4.2, the applied bias was assumed to decay back to its initial steady state hold-off value of 600 Volts at about 40 ns. This effectively yields an applied pulse of 25 ns, which was then repeated. A second voltage pulse can be seen in Figure 4.2 beginning at 40 ns.

The transient circuit current corresponding to the above periodic voltage waveform is shown in Figure 4.3. An initial spike in the current is seen, and this is due to a displacement current that is generated within the device in response to the voltage ramp from 0 Volts to 600 Volts. Following the initial build up of the internal fields and carrier densities within the device, a steady OFF state situation is reached and the current drops to near-zero levels. The current remains at this near-zero level until the application of

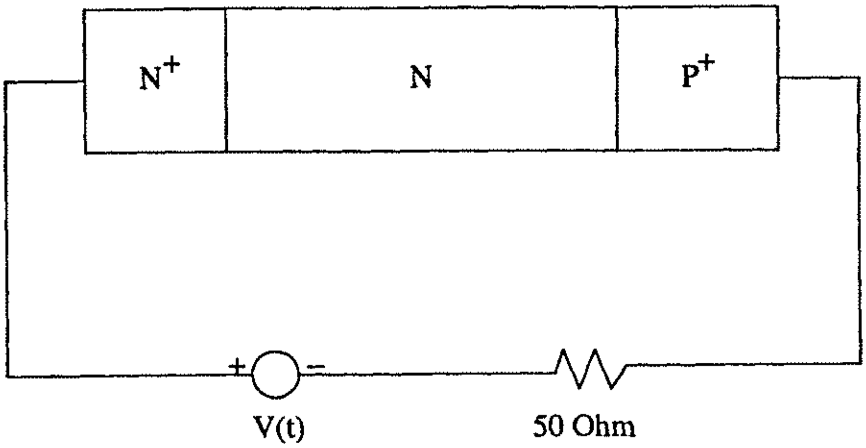

Figure 4.1. Circuit configuration for SAS device.

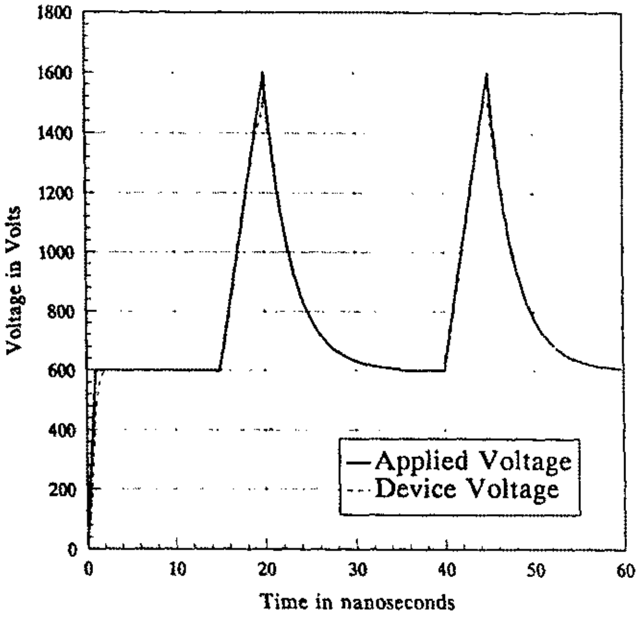

Figure 4.2. Time dependence of the applied and device voltage.

the ionizing voltage ramp at 15 ns. The current then increases to about 0.5 Ampere, and is comprised of both the displacement and conduction components. Of these two, the displacement component gradually weakens as a steady state electric field distribution begins to be set up within the device. This gives rise to a slight decrease in the current from the 0.5 Ampere level to about 0.4 Ampere. At around 18 ns in time, the current is seen to begin increasing dramatically from its value of about 0.4 Ampere to a maximum of about 1.7 Amperes. This maximum occurs at 20 ns, and corresponds to the time at which the applied voltage is a maximum of 1600 Volts. The increase in current is due to the initiation of internal impact ionization and the process of carrier avalanche. As a result of this current increase, the device voltage drops slightly due to the increase in the voltage across the 50 Ohm resistor. This can be seen from the "dashed curve" of Figure 4.2.

Following a decay in the applied voltage, the current begins to decrease as expected. The current falls below zero at about 21 ns, and assumes a slight undershoot before settling to a near-zero level at around 32 ns. The negative current signifies that the SAS device is functioning as an active element and supplying power to both the resistor and the voltage element. Physically, the source of this power supply comes from the stored electromagnetic energy within the SAS device which had been built up during the applied voltage ramp. The undershoot characteristic and its duration is expected to depend on the actual circuit conditions. For instance, a higher value of the circuit resistance would lead to a quicker dissipation of the energy stored within the SAS device, and hence a less significant undershoot. Similarly, the presence of circuit inductances would also weaken the undershoot behavior. Alternatively, by incorporating suitable diode elements into the overall circuit, the negative portions could effectively be clipped. Finally, as seen from Figure 4.3, the current response to the second voltage pulse is similar in nature to the first. A repetitive and periodic current waveform is therefore seen to result from this device with some degree of internal avalanche action. The current pulse width is about 6 ns with the sharp peak having an even smaller duration of 1 ns. This 1 ns pulse could actually be extracted and made available for subsequent purposes by using suitable high pass filters to eliminate the slower components of the transient.

Results of the internal electric field profile and the carrier distributions for the SAS device under the above simulation conditions are presented next. These details provide better insight into the overall physics of the device operation. The initial steady state conditions existing within the device under unbiased conditions are shown first through the curves of Figure 4.4. These curves were obtained by carrying out the 1D numerical simulations with zero applied bias. The ionized impurity concentration is seen to be piecewise continuous and nearly equal to the density of the impurity atoms. This is due to the low ionization energies of the dopant atoms in Silicon which leads to near-complete ionization. Thus for example, the ionized donor density N_D^+ within the heavily doped N^+-region on the left is nearly 5×10^{16} cm^{-3}. As expected, the electron density is appreciable only over the heavily doped N^+-region and is negligible elsewhere. This is consistent with the results based on a simple depletion approximation [40] and hence validates our simulation approach. Similarly the hole density is appreciable only over the heavily doped P^+-acceptor region and negligible elsewhere.

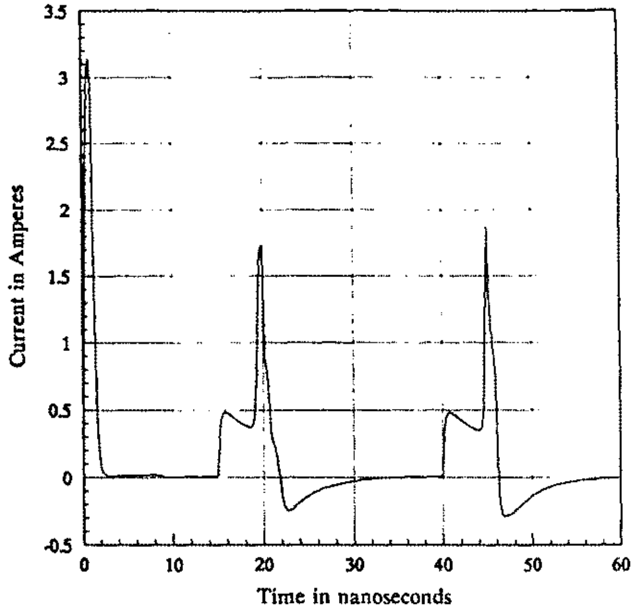

Figure 4.3. Current transient through the device.

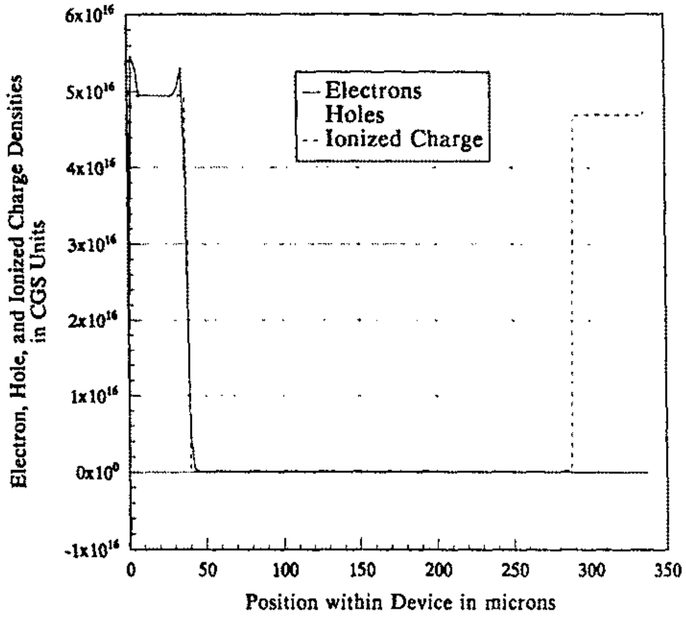

Figure 4.4. Initial free carrier densities for unbiased case.

A slight structure in the carrier densities is seen from the curves of Figure 4.4. This is due to the effects of carrier diffusion. On both the two extreme ends of the device for instance, the carrier densities fall sharply. This decrease arises due to the diffusion of majority carriers out across the boundaries of the device. For instance, the holes on the right diffuse into the metallic contacts leaving behind a much lower concentration of holes. As is the case with simple p-n junctions, such a diffusive flow which sharply reduces the mobile carrier density, leads to the creation of internal electric fields. These fields stabilize the current and establish a dynamic equilibrium. For instance at the right boundary, the outflow of holes creates a charge imbalance, leaving behind a net negative charge within the semiconductor due to the presence of the immobile ionized acceptors. A negative electric field is gradually established as a result which works to counter the diffusive flow. Finally, in the steady state shown in Figure 4.4 this buildup in field prevents the flow of any net current. Carrier fluctuations of a similar origin are also seen at the left boundary and all of the homojunctions. The resulting fields due to this charge readjustment is shown in Figure 4.5. As expected, the fields are positive at the N^+-N and the N-P^+ junctions. The magnitude in keeping with simple depletion approximation p-n junction theory, is much higher at the N-P^+ junction. This occurs due to the larger band-bending and a higher built-in potential that is associated with the N-P^+ junction as compared to the N^+-N junction. The results of Figures 4.4 and 4.5 not only provide a validation of the numerical model that has been implemented here, but also furnish data on the initial steady state of the device for subsequent transient simulations.

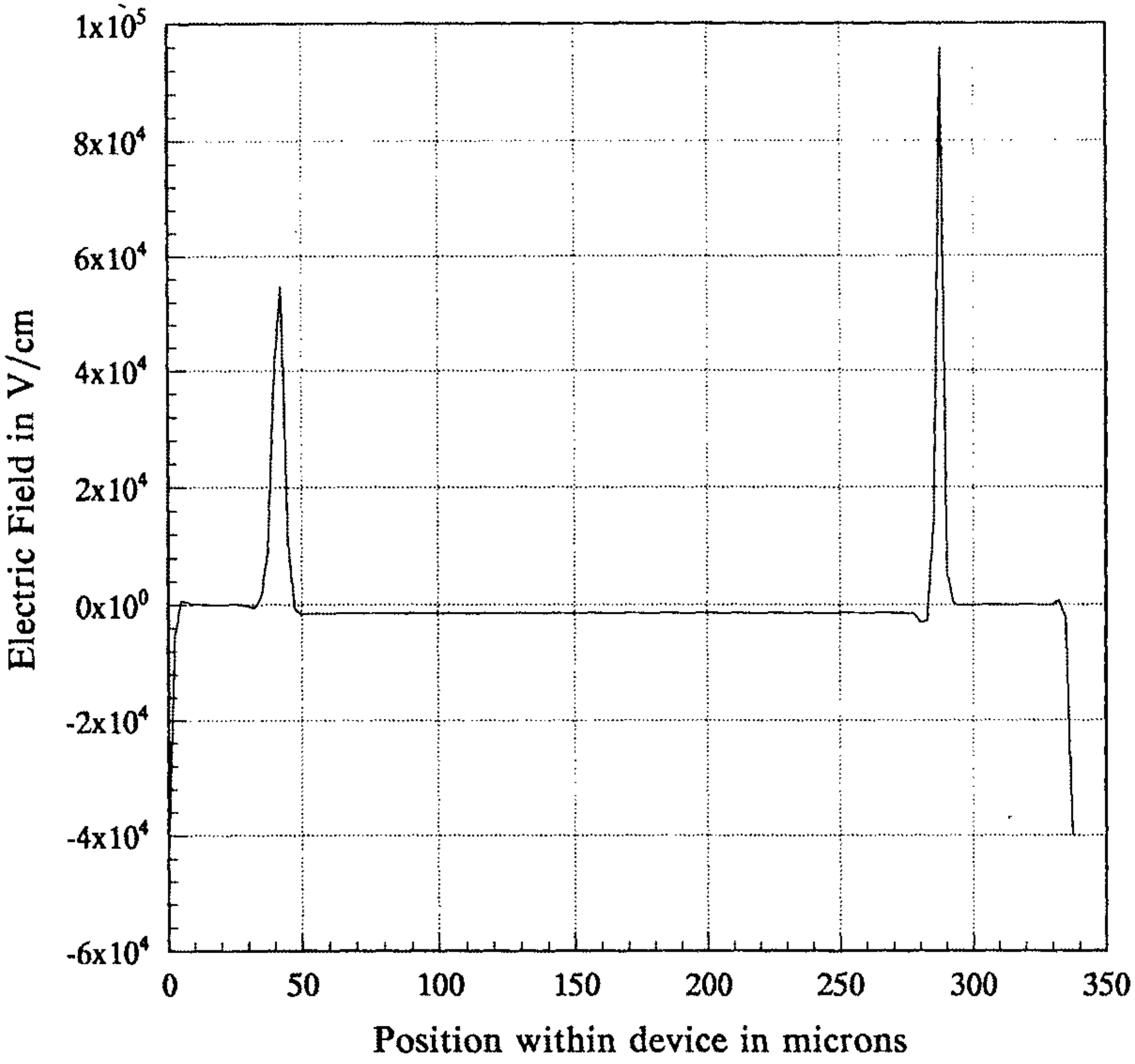

Figure 4.5. Internal electric field profile for unbiased case.

Results relating to the internal behavior of the SAS device during transient operation are presented next. The internal profiles were obtained at discrete times during the switching transient for the voltage waveform described in Figure 4.2. Hence, the data represents snapshots of the internal electric fields and carrier densities during the temporal evolution of the device. The electric field profile at 10 ns is shown in Figure 4.6. At this time, a voltage of about 600 Volts is applied across the device as seen from the waveform of Figure 4.2. The electric field profile is triangular in shape as would be expected on the basis of the depletion approximation, with a maximum value occuring at the N-P^+ junction. The peak magnitude of 1.44×10^7 V/m is below that for impact ionization. Most of the field extends into the low doped, low-conductivity N-region. The carrier densities at 10 ns are shown in Figure 4.7. The density of ionized carriers almost remains the same as that for the unbiased case shown in Figure 4.4. However, some changes are evident in these profiles. For example, at the 600 V bias, the depletion region widths are larger than those of Figure 4.4 due to the strong reverse bias. The mobile carriers tend to move away from the junctions as the depletion regions expand. This leads to free carrier accumulations and charge density increases within the adjoining space. These accumulations are seen as peaks in the curves of Figure 4.7 adjacent to the depletion regions. Due to the close proximity of the metal-semiconductor and the N^+-N junctions, these accumulations give rise to a twin peaked structure in the electron distribution within the N^+ region.

The electric field distributions at 18 ns and 20 ns are shown in Figures 4.8 and 4.9. The development of an electric field and its gradual expansion into the low doped

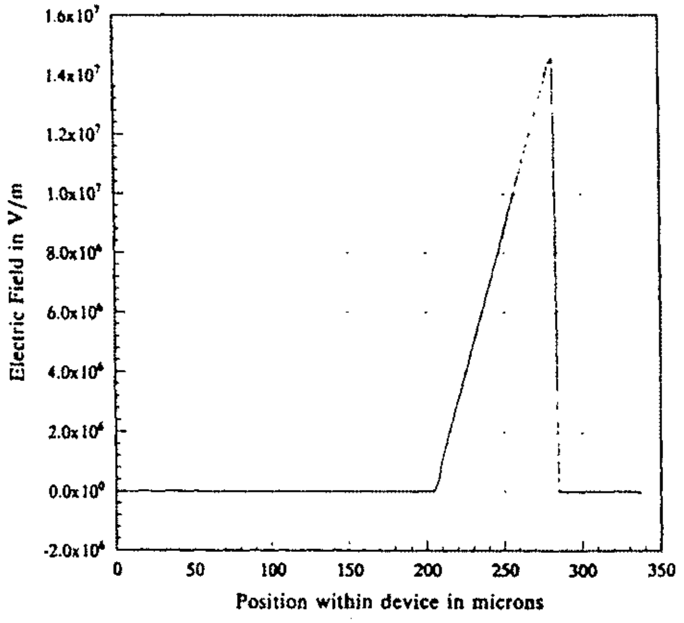

Figure 4.6. Internal electric field at 10 nSec.

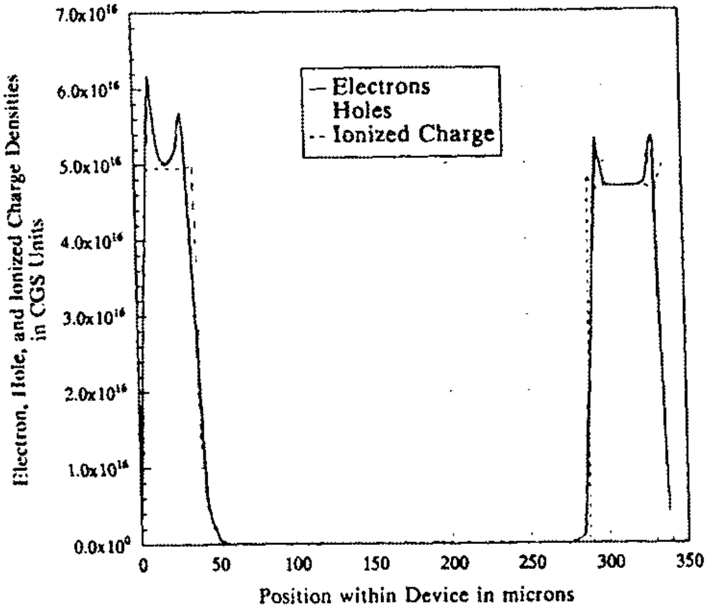

Figure 4.7. Free carrier densities at 10 nSec.

N-region is evident. Physically, propogation of the field within the device gives rise to an internal displacement current. A relative comparison between Figures 4.8 and 4.9 reveals a slight polarization effect between the 220 micron to 260 micron region. This polarization is caused by the movement of electron-hole pairs in opposite directions upon impact ionization. This leads to a weakening of the electric field and appears in Figure 4.9 as a slight dip in the field in the region between 220 microns and 260 microns. The charge distribution at 20 ns is shown in Figure 4.10. The twin peaked structure evident in Figure 4.7 is not so pronounced as the process of diffusion tends to smear out the inhomogeneities. Diffusion remains a powerful process in this region due to the low electric field levels. The hole densities are higher as compared to Figure 4.7 due to contributions arising from some impact ionization at the N-P^+ region. Two important features regarding the free carrier densities are worth noting. First, the increase in the electron concentrations is minimal since the electric field within the N^+ region is almost negligible. Second, the hole density does not undergo a dramatic increase. This is due to the fact that the system does not have an abundant supply of carriers for injection into the high field region at the N-P^+ interface. As the field increases at this interface, holes move into the P^+ region, while the electrons are made to drift out towards the N^+ side. This process of charge movement, however, depletes the N-P^+ junction and increases the depletion layer. Once the free carriers have been depleted from the high field region in this fashion, the supply of carriers needed to initiate and sustain avalanche multiplication is lost.

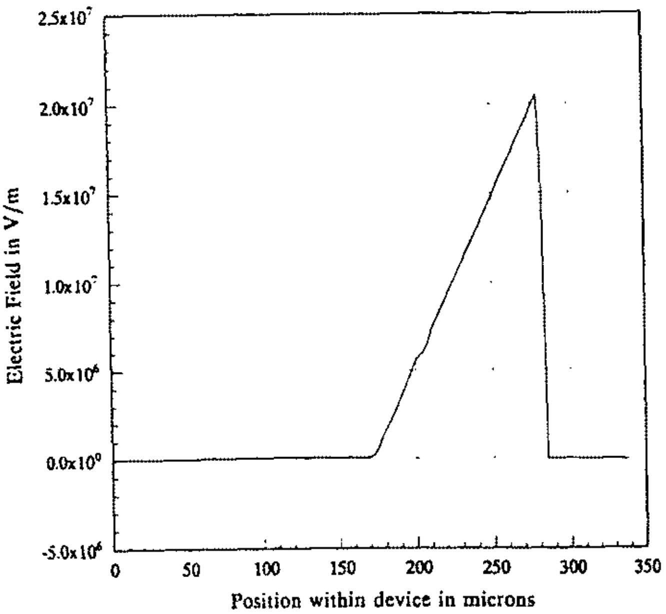

Figure 4.8. Internal electric field at 18 nSec.

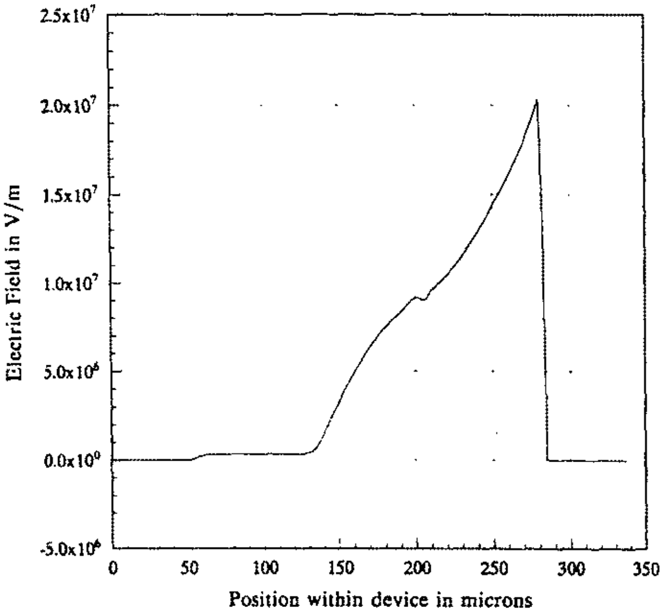

Figure 4.9. Internal electric field at 20 nSec.

At later times, the internal fields begin to collapse as the external bias is reduced back towards the 600 Volt level. This is evident from the internal electric field distributions shown in Figures 4.11 and 4.12 which correspond to the 30 ns and 38 ns time instants. The peak values are seen to be getting progressively smaller and the spatial extention into the N-region is much smaller than that seen in Figure 4.10. The carrier profile at 30 ns is shown in Figure 4.13. The electron density has become smoother due to diffusive smearing. The hole density still remains higher than the level at 10 ns as shown in Figure 4.7. Unlike the electron distribution, however, the hole profile cotinues to exhibit a twin-peaked structures. This is because the diffusion process in holes is relatively weak given their larger effective mass and lower mobilities which leads to low diffusion coefficients.

As was briefly mentioned above, the impact ionization and avalanche process in the SAS device is not very strong nor can it be sustained over a long time duration. The root cause for this is the inadequate supply of free carriers within the high field regions that are necessary for carrier multiplication. The limited supply can only give rise to an initial burst of avalanche generation. Hence, changes in the conduction within this device is predominantly due to displacement currents and the development and propogation of internal electric fields.

4.3 TWO-DIMENSIONAL ANALYSIS

Having presented the simulation results for the transient electrical response of the SAS device based on a one-dimensional drift-diffusion approach, this section describes

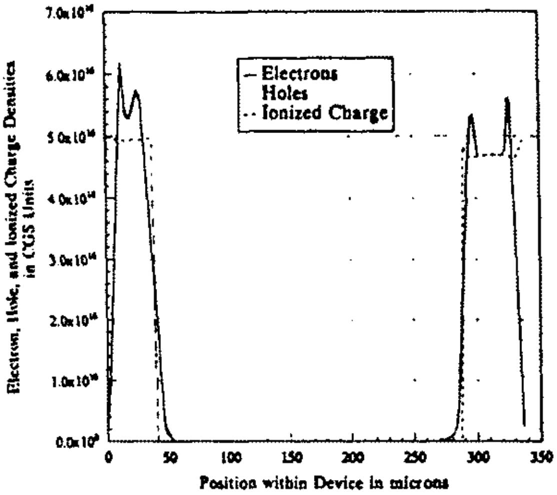

Figure 4.10. Free carrier densities at 20 nSec.

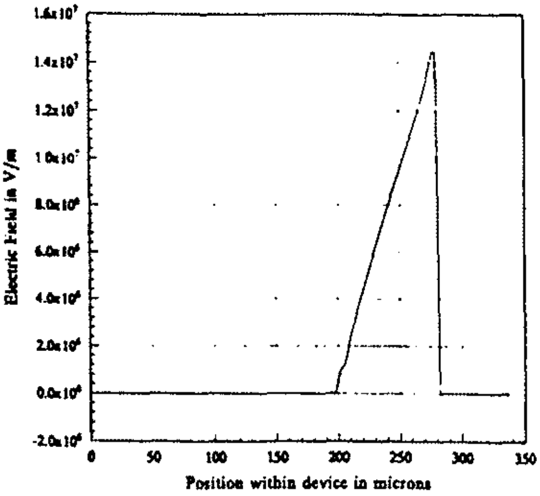

Figure 4.11. Internal electric field at 30 nSec.

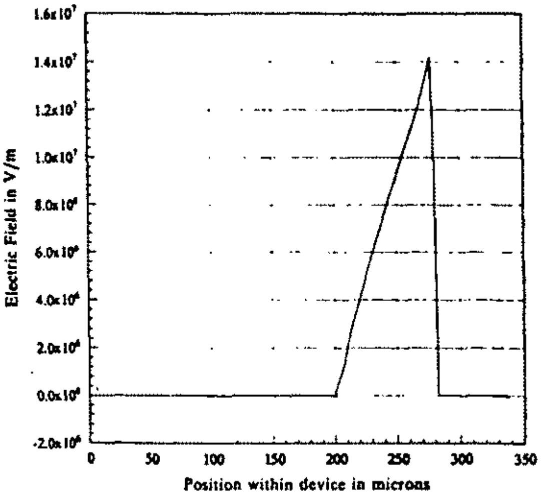

Figure 4.12. Internal electric field at 38 nSec.

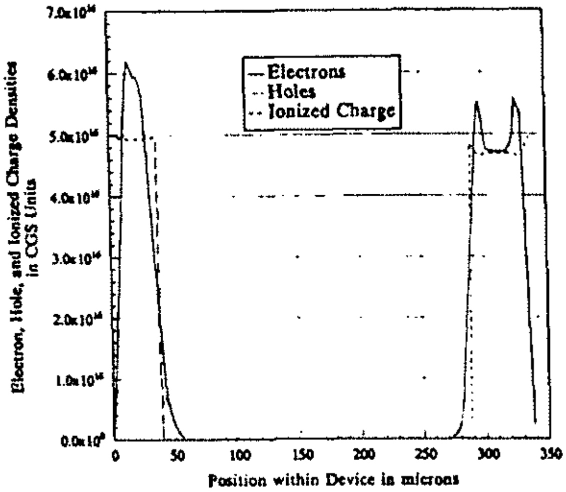

Figure 4.13. Free carrier densities at 30 nSec.

the results obtained with a two-dimensional model. As mentioned earlier, there were two main objectives in carrying out the 2D simulations. (i) First, effects of doping variations along the transverse direction on the response characteristics were to be probed and analyzed. Such variations could either be accidental being fashioned by the implantation and diffusion characteristics during processing, or deliberate in nature. In the former case, the simulations would provide quantitative assessment of changes in the device performance due to the accidental aberrations. In the case of deliberate tailoring, the simulations would be a convenient tool for selecting an optimum transverse doping profile for enhanced performance. The potential benefits of such tailoring could then be brought out very clearly in a quantitative manner. (ii) Evaluation of two-dimensional effects, such as current filamentation and the transverse non-uniformities in impact ionization, for the SAS devices. Based on the simulation results, the spatial locations and extent of such detrimental 2D effects would be better understood. This understanding could then be used to develop more efficient, robust and rugged devices.

The 2D implementation as discussed in chapter 3 was used to obtain the transient response of the SAS device. The simulations were carried out for four different doping profiles along the transverse direction. These four doping profiles chosen for the simulations were as: (i) A sinusoidal shaped centro-symmetric distribution with maximum dopant density at the two opposite surfaces and a minima over the axial center, (ii) A sinusoidal shaped centro-symmetric distribution with a minimum dopant density at the two opposite surfaces and a maxima over the axial center, (iii) A two-layer asymmetric, off-center composite distribution, and (iv) Uniform doping profiles along the transverse direction. Three-dimensional plots showing details of the dopant distribution profiles for each case are shown later alongwith a discussion of the results obtained for each profile.

4.3.1 TWO-DIMENSIONAL RESULTS AND ANALYSIS: CASE I

As with the 1D simulations, the SAS device was again assumed to comprise of N^+-N-P^+ Si material with nonuniform doping profiles along the transverse direction for each of the three regions. The same functional form was used for the doping profiles in the three constituent regions. The peak dopant density values were taken to be: $N_D^{max} = 5 \times 10^{16}$ cm^{-3} in the N^+ region, $N_D^{max} = 10^{14}$ cm^{-3} for the lower doped N-layer, and $N_A^{max} = 5 \times 10^{16}$ cm^{-3} for the P^+ region. The external circuit was the same as that used for the 1D simulations and has already been shown in Figure 4.1. The periodic "saw-tooth" type voltage waveform was again assumed.

Simulation results for the initial unbiased steady state conditions within the SAS device for the first of the four 2D doping profiles are shown in Figures 4.14-4.18. The dopant profile for this case was taken to be a sinusoidally symmetric distribution with minimum dopant density at the two opposite surfaces and a maxima on the central axis. The resulting ionized impurity concentration as obtained from the simulations is shown in Figure 4.14. The peak magnitude of the ionized impurity density nearly equals 5×10^{16} cm^{-3} which is the maximum concentration of dopant atoms. This peak lies on the central axis of the device and the profile is symmetric. The 2D electron and hole profiles are plotted in Figures 4.15 and 4.16, respectively. Their transverse shapes follow that of the dopant distribution. In addition, some structure along the longitudinal direction is also seen at the junctions. This is the same as that obtained for the 1D case shown in Figure 4.4. This is due to free carrier diffusion and the formation of built-in electric fields and depletion regions at the various junctions and interfaces. The unbiased steady state electric fields associated with the charge distributions of Figures 4.14-4.16 have been shown in Figures 4.17 and 4.18. The longitudinal electric field distribution E_x shown in Figure 4.17 is similar to that of Figure 4.5 for the 1D case. The transverse field E_y is seen in Figure 4.18. A number of features associated with this plot are immediately evident. First, the magnitude of E_y is much smaller than that of E_x. This is to be expected since the steady state electric field is roughly proportional to the negative gradient of the majority carrier density "n(x,y)". This follows from the requirement of a zero conduction current, and leads to E_y being proportional to: -[dn/dy]. Since the gradient "dn/dy" is antisymmetric for the chosen doping profile, the electric field distribution E_y also has an anti-symmetric shape. Next, since the gradient of the majority carrier density and dopant distribution along the transverse "y" direction is not as large as that along the x-direction, the magnitude of E_y is smaller than E_x. Finally, since electrons and holes are oppositely charged, their diffusion along the transverse direction gives rise to built-in fields E_y which are mutually anti-parallel. This is evident from Figure 4.18 as the E_y direction within the P^+ region on the left is opposite that of the field direction in the N and N^+ regions.

The transient SAS circuit voltage waveform used for the 2D simulations was the same as before, and is shown again in Figure 4.19 for clarity. The transient current

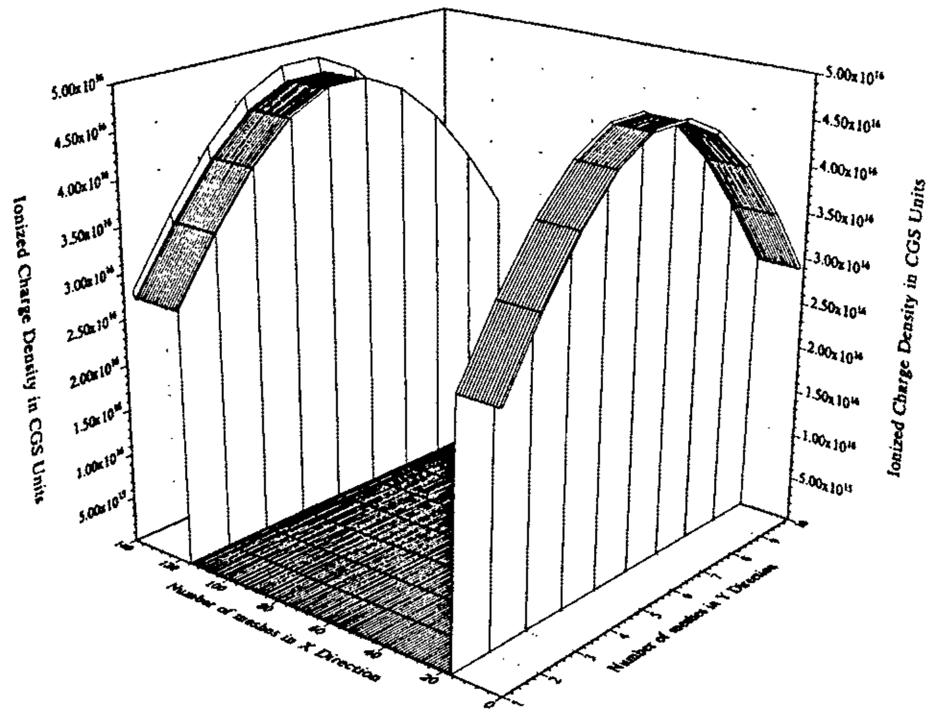

Figure 4.14. Initial ionized charge densiy: unbiased.

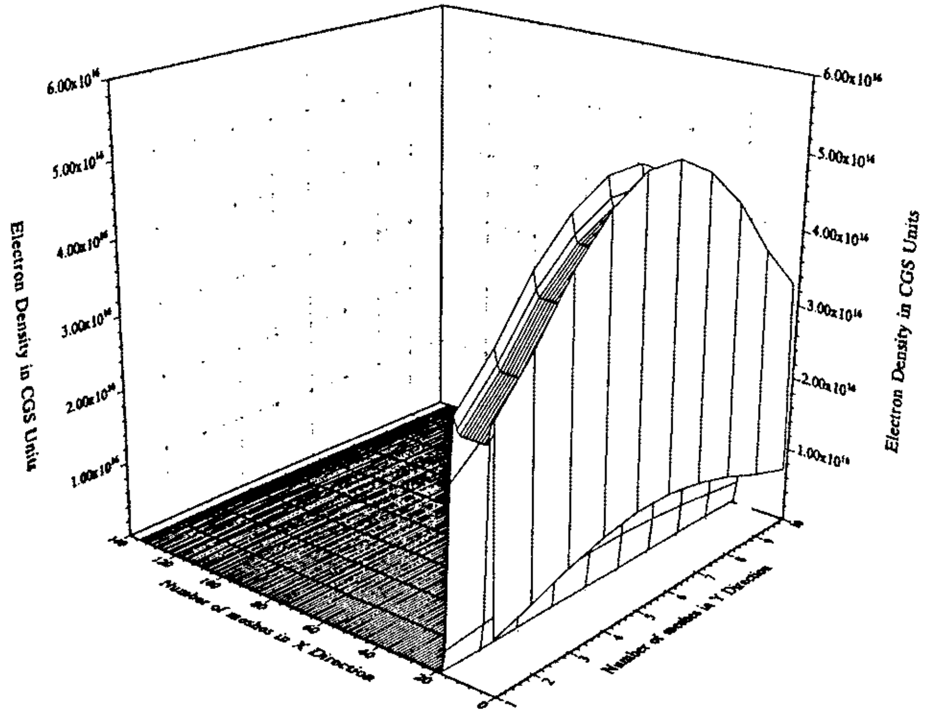

Figure 4.15. Initial electron density: unbiased.

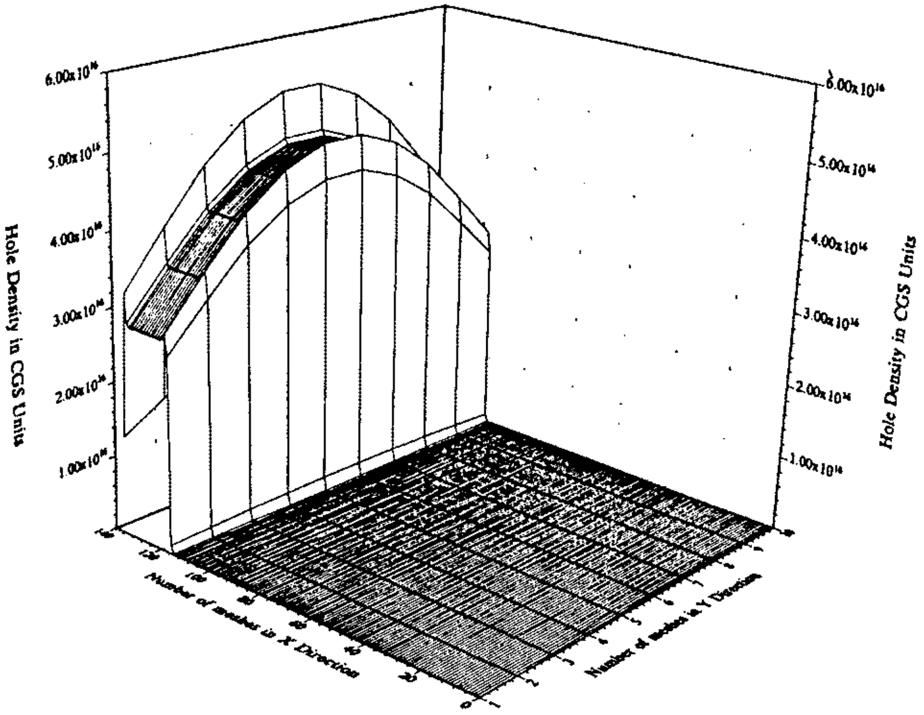

Figure 4.16. Initial hole density: unbiased.

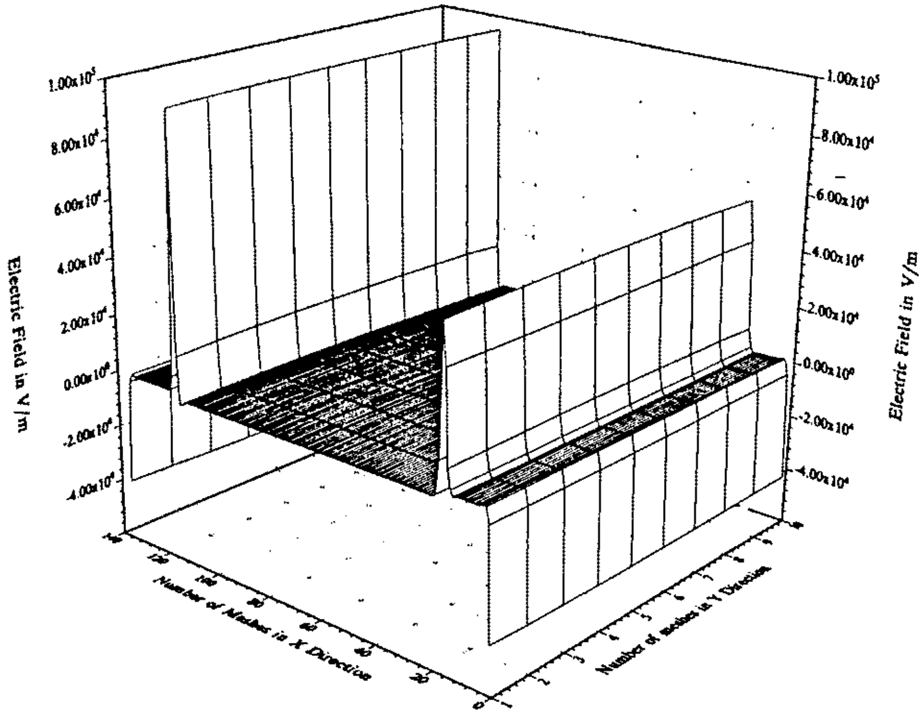

Figure 4.17. X-component of electric field profile: unbiased.

corresponding to this voltage waveform is shown in Figure 4.20. The initial spike represents as before, a displacement current created in response to the voltage ramp from 0 Volts to 600 Volts. Most of the other features and characteristics are also very similar to those obtained in Figure 4.3 from the 1D simulation. The only notable difference is that the second current pulse appears to have a slightly lower peak than the first. This marginal variation between the first and second current pulses seems to suggest that a "short-term memory effect" is inherent in the SAS device. Such a memory effect is probably associated with the transverse propagation of both the electric field and the free carrier densities within the device during the turn-on cycle. Though most of the changes and movements take place along the longitudinal direction, the time dependent transverse variations and movements are not completely negligible. The movement of carriers along the transverse direction and the resulting changes in the electric field distort the state of the semiconductor system. The system tries to revert back to its initial "OFF state" and to annul the distortions after the external voltage decreases and goes back to the 600 Volt level. During the "turn-off" transient, changes in the electric fields are predominantly along the longitudinal direction since this is the orientation of the applied voltage. In response to the changing electric fields, the carrier density distributions also change, with the movement being primarily along the longitudinal direction as well. The result is a relatively fast redistribution parallel to the longitudinal axis leading to near complete recovery of the semiconductor system. However, the recovery and charge redistribution in the transverse direction is not as rapid. This occurs for two reasons. First, the electric field is changing at a very slow rate as there is no applied voltage in this direction.

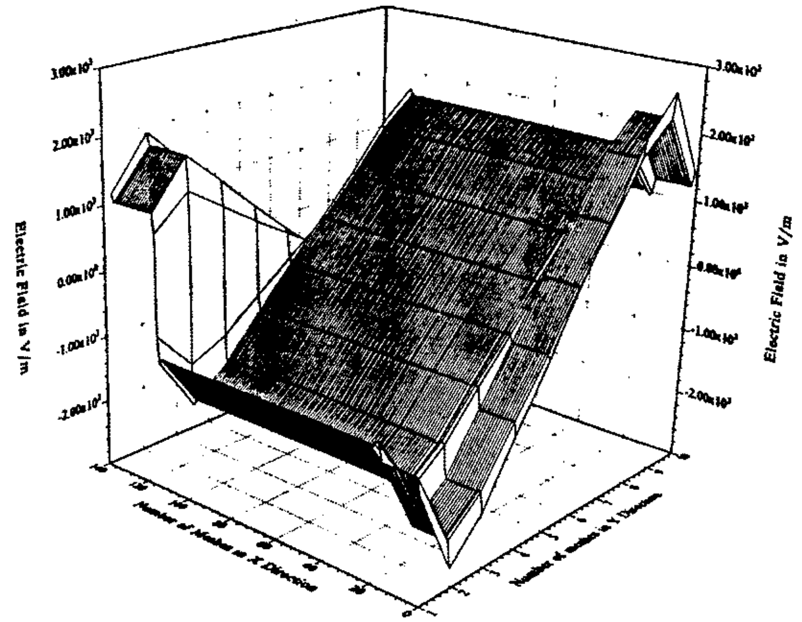

Figure 4.18. Y-component of internal electric field profile: unbiased.

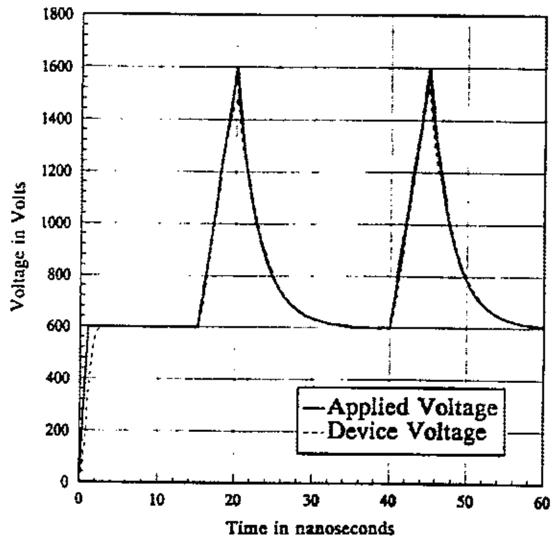

Figure 4.19. Time dependence of voltages.

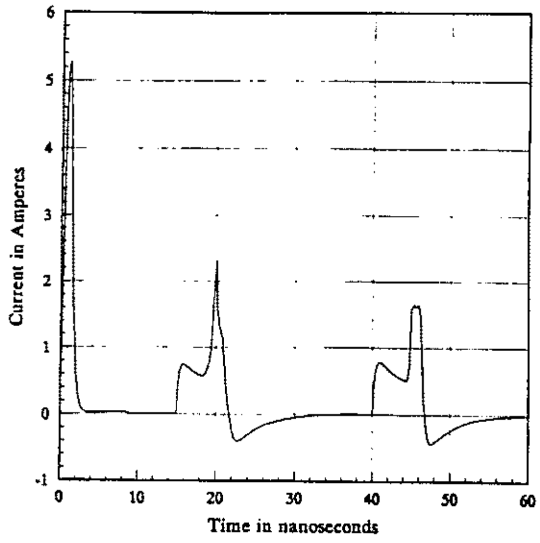

Figure4.20. Current transient through the SAS device.

Second, since the values of the transverse field E_y are much smaller than those of E_x, the driving force for carrier movement and relocation is meager. Consequently, the inherent "relaxation time" or the duration necessary for bringing the semiconductor system back into the initial "OFF state" is quite large. From the simulation results, it appears that this time is more than 25 ns since the SAS does not appear to have fully recovered at the start of the second pulse.

Results pertaining to the internal electric field are presented next. The longitudinal components of the electric field at 10 ns, 18 ns and 20 ns are presented in Figures 4.21-4.23. From these plots it is obvious that the internal field grows and propagates from the P^+-N junction on applying the biasing pulse. A travelling electromagnetic wave is thus evident. From Figure 4.23, this E_x wave is seen to develop a distinct hump near the center of the device at 20 ns. As a result of this hump, the field magnitude over the central portion of the P^+-N junction in Figure 4.23 is not as high as at the two ends. This is in keeping with the requirement that the line integral of the longitudinal field E_x have a constant value across all paths parallel to the longitudinal axis. This value at any time instant, has to be independent of the transverse location as discussed previously. Since the electric field increases at the central portion of the device over the central axis, its value on the central axis at the P^+-N junction is relatively lowered to maintain the path independent requirement.

The snapshots of the transverse field component at 10 ns and 20 ns have been shown in Figures 4.24 and 4.25. The values are much smaller than those of E_x at the corresponding times as may be expected. The temporal development of E_y reveals the

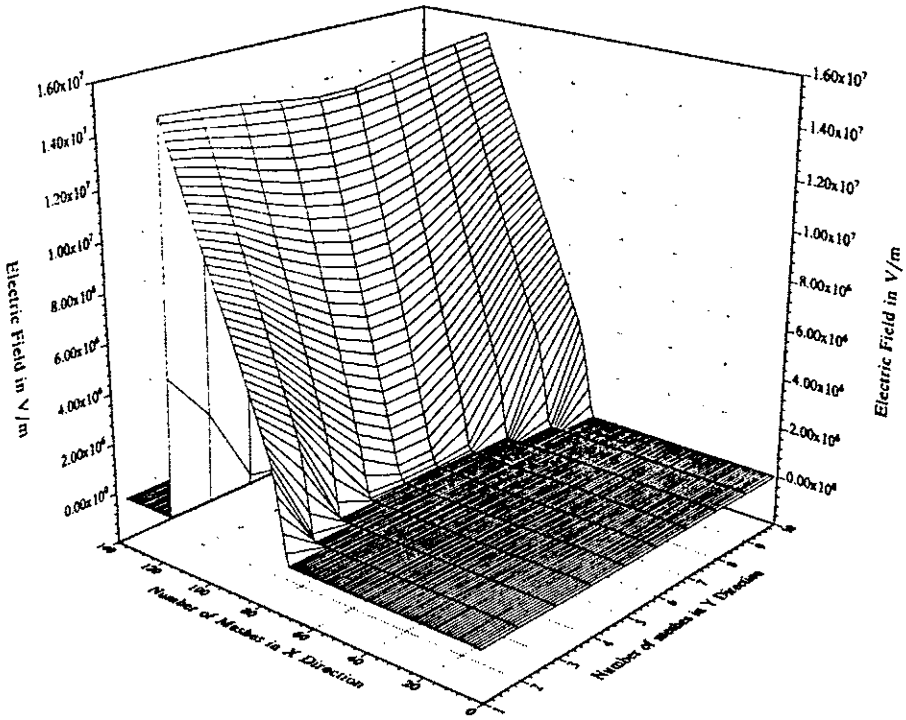

Figure 4.21. X-component of internal electric field at 10 nSec.

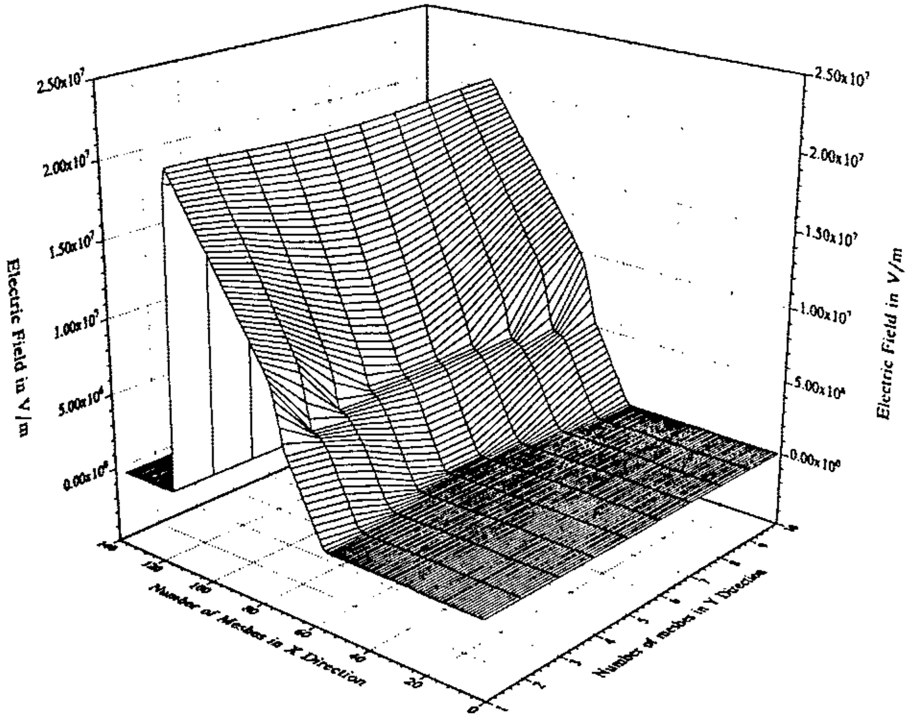

Figure 4.22. X-component of internal electric field at 18 nSec.

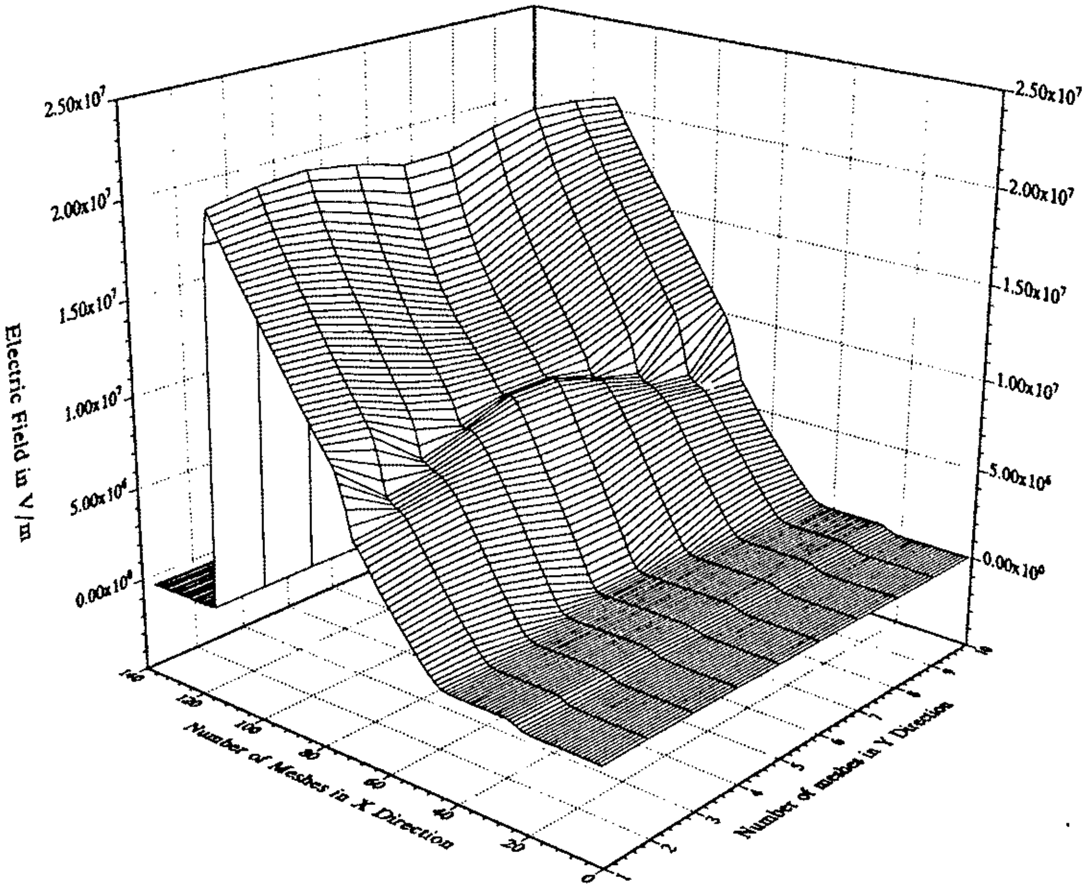

Figure 4.23. X-component of internal electric field at 20 nSec.

formation and movement of an electron wave, and can be understood based on the following physical sequence of events. Application of the initial voltage ramp from 0 Volts to 600 Volts widens the depletion region as compared to the unbiased steady state. Electrons present on the N-side of the P^+-N junction move away from the junction and into the N region. These carriers not only have a longitudinal motion into the N-region, but are also diffuse laterally away from the center. However, the net transverse current has to equal zero at all times since there is no conductive path in this direction. As a result, a transverse electric field E_y builds up to force a dynamic equilibrium with zero net current as in the unbiased case of Figure 4.18. The shape of E_y at 10 ns is therefore again proportional to the negative gradient of the free carrier density and is anti-symmetric relative to the central axis. Most of the transverse diffusion occurs at the edge of the depletion region on the N-side which has a supply of free carriers. The movement of holes from the P^+ portion of the P^+-N junction, however, does not produce a significant transverse field E_y since the change in the depletion layer is very small on the P^+ side because of the relatively high doping.

Figure 4.25 shows E_y at 20 ns. The primary difference between this snapshot and the plot at 10 ns is the distinct growth and formation of a secondary high field region. This exhibits itself as a secondary bump behind the peaks initially seen in Figure 4.24. The secondary bumps are antisymmetric and are caused by the injection of electrons into the N-region from the P^+-N boundary. This transverse distribution of this wave of injected electrons is once again non-uniform and follows the sinusoidal shape of the doping density. As the result, transverse diffusion again takes place, leading to the

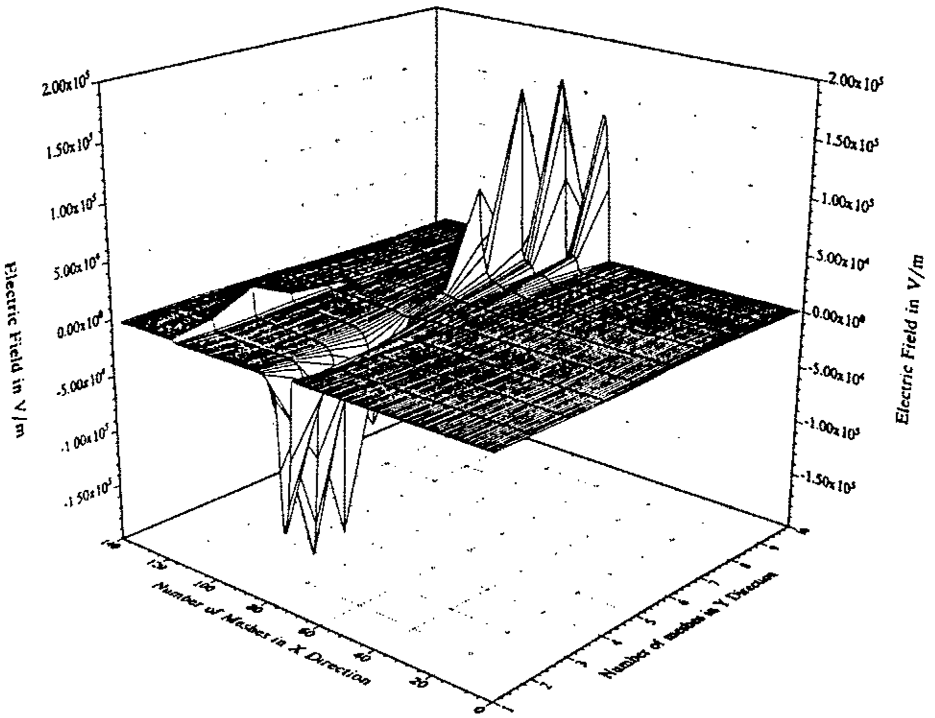

Figure 4.24. Y-component of internal electric field at 10 nSec.

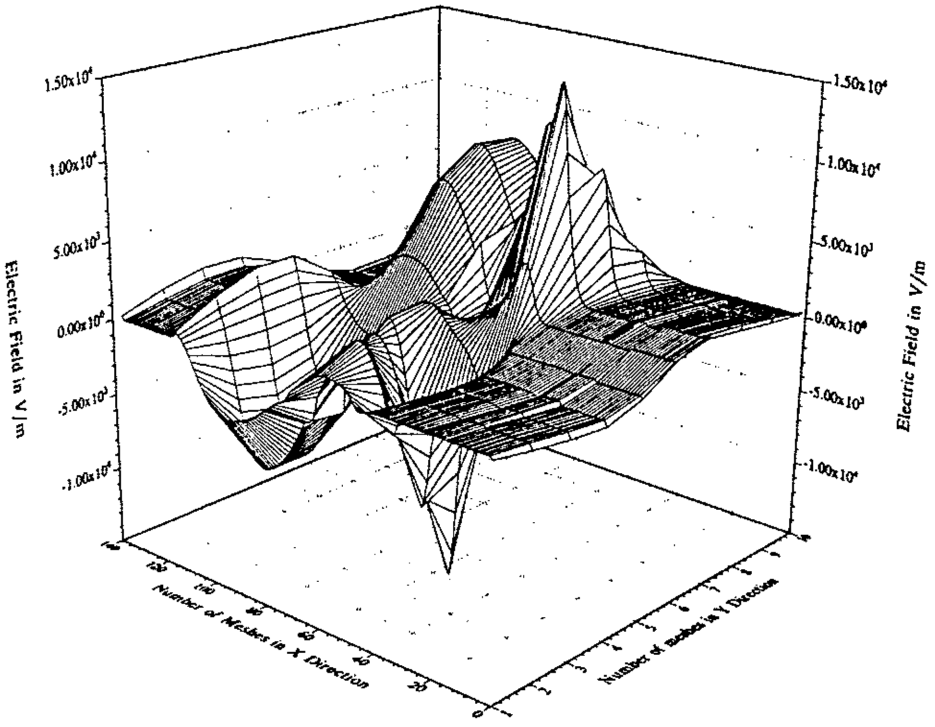

Figure 4.25. Y-component of internal electric field at 20 nSec.

development of a secondary anti-symmetric E_y profile. However, the secondary bump occurs at a slightly different location and is nearer to the P^+-N boundary. This indicates that the electron injection responsible for creating the secondary E_y profile arises from impact ionization, based on the following argument. The P^+-N junction prior to the start of the 1600 Volt voltage ramp is already in a state of depletion as a result of the 600 Volt reverse biasing voltage. It is thus incapable of supplying any free carriers. Instead, the electronic injection is made possible due to avalanching and impact ionization across the junction boundary. The creation of electrons is probably due to the holes as they move away from the junction deeper into the P^+ side.

The current distributions within the SAS device are shown in Figures 4.26-4.28. The longitudinal conduction current at 18 ns shown in Figure 4.26 is relatively large throughout the N^+ and the P^+ regions. This is expected since these regions have high carrier densities leading to large drift current contributions. The conduction current within the middle N-region, however, is much smaller and negligible by comparison. Figure 4.27 at 20 ns reveals a general increase in the current. Within the N region, the conduction current increase is dramatic over the central axis. This can be attributed to three factors. The first arises from the movement of the existing mobile electrons within the N-region upon the application of the reversed biasing ramp. As these carriers move away from the P^+ side, the depletion region begins to expand. Since the central region over the axis has the highest doping and hence the largest supply of mobile carriers, the conduction current is the largest over this section. The second factor arises from electron injection from the P^+ side into the N-region. This mainly occurs over the central axial

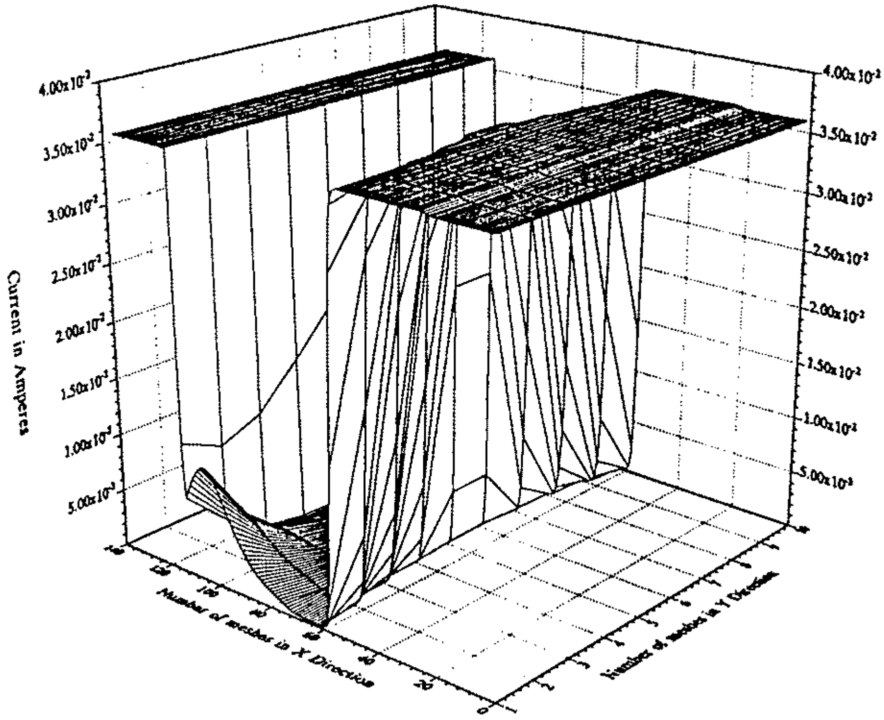

Figure 4.26. X-component of conduction current at 18 nSec.

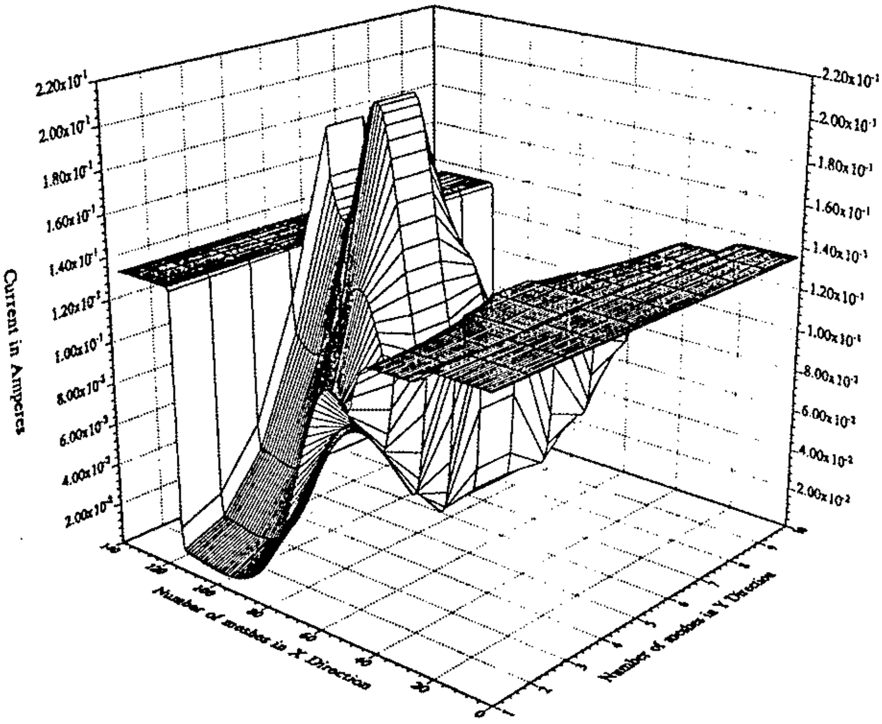

Figure 4.27. X-component of conduction current at 20 nSec.

portion which has the highest supply of carriers to initiate impact ionization. The double humped structure on the axis is indicative of the finite time lag associated with impact ionization and subsequent injection after the depletion region has increased on the N-side of the P^+-N junction. Thirdly, the strong increase in the longitudinal electric field E_x within the N-region, relative to the N^+ and P^+ regions also contributes to the high conduction current. The drift velocity is appreciably enhanced as a result of the electric field increase which promotes a high drift current value. Figure 4.27 also reveals the presence of a highly non-uniform current distribution along the transverse dimension, and is indicative of a "filamentary mode". The central location of this current filament can be potentially detrimental, since it can lead to internal heating. Heat produced within the filament would be more difficult to dissipate through external cooling, given its central axial location. Had the filament been towards the outer boundaries, heat dissipation through external cooling schemes would be easier. The heating can potentially lead to a second breakdown and irreversible device failure. These results therefore indicate that SAS devices with large doping towards the central axis cannot be left in the "ON-state" for a long duration. This curtails the time duration of the high voltage pulse. Finally, the profile of the longitudinal current at 38 ns shown in Figure 4.28 reveals that the system has almost reverted to its initial "OFF-state". The values are much lower than those shown in Figure 4.27. Only a small region near the P^+-N junction exhibits current. This represents the on-going and incomplete relaxation of E_x within the device.

The total longitudinal current I_x as a function of the transverse direction is shown in Figures 4.29-4.31. These plots were obtained from the simulations at various times.

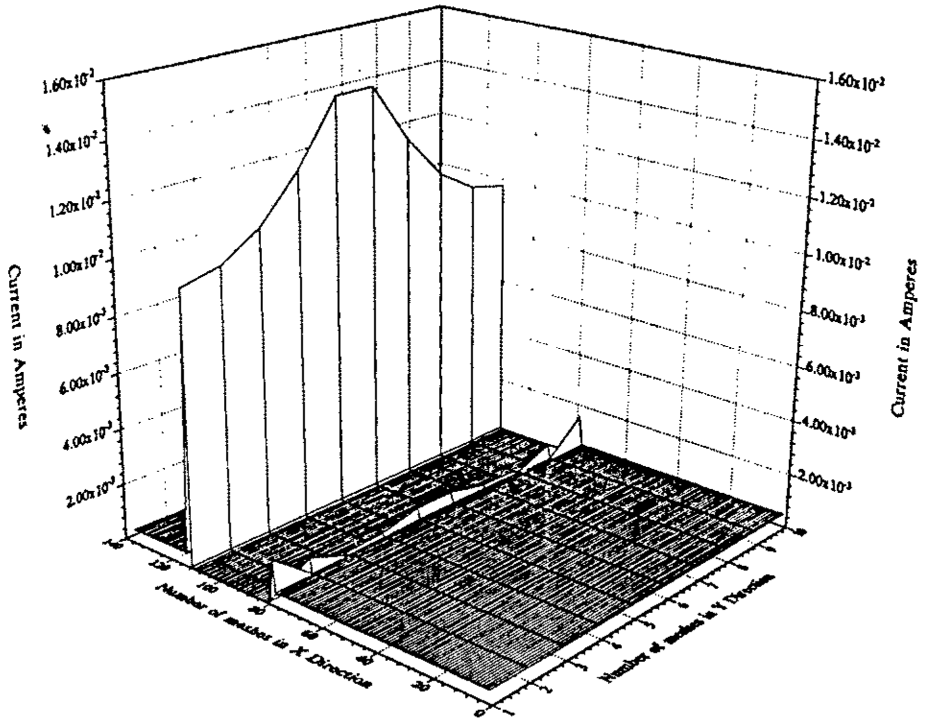

Figure 4.28. X-component of conduction current at 38 nSec.

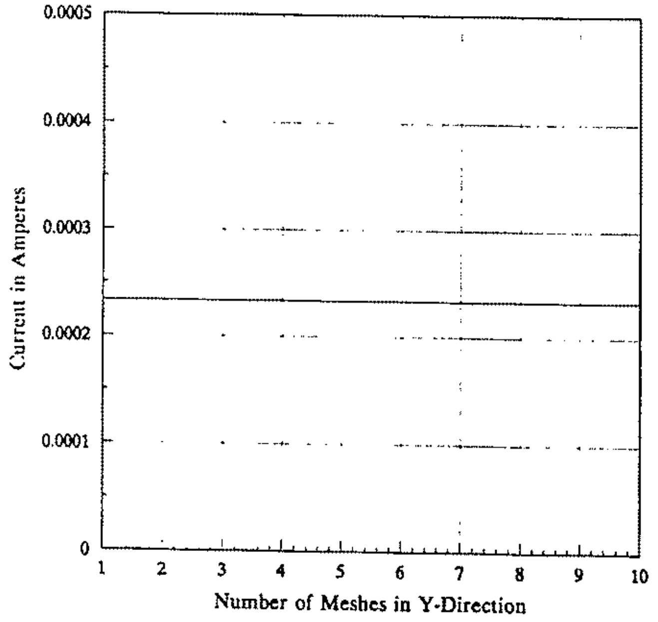

Figure 4.29. Total current through SAS device at 10 nSec.

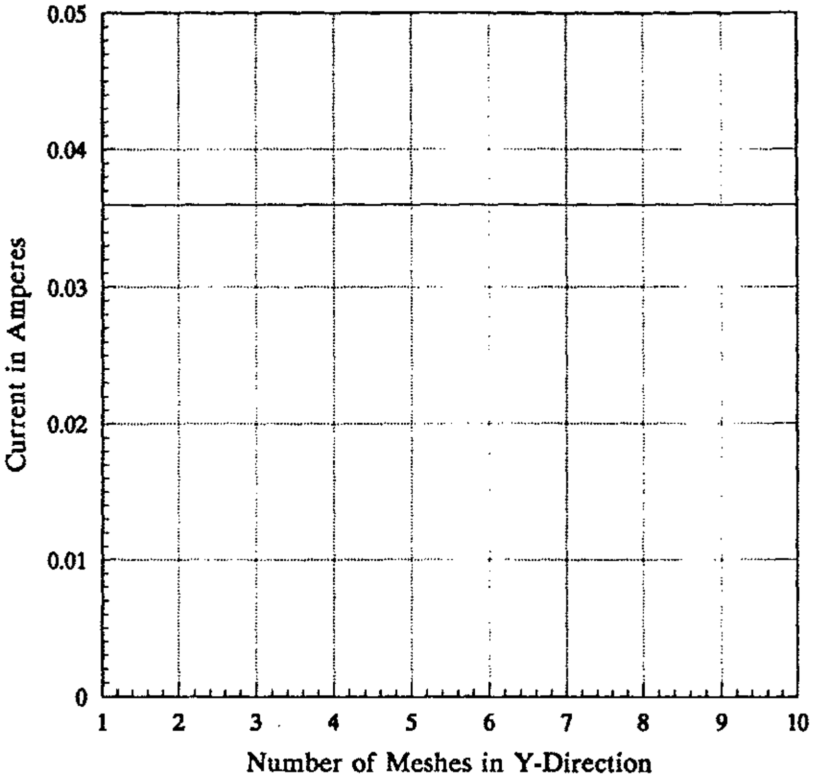

Figure 4.30. Total current through SAS device at 18 nSec.

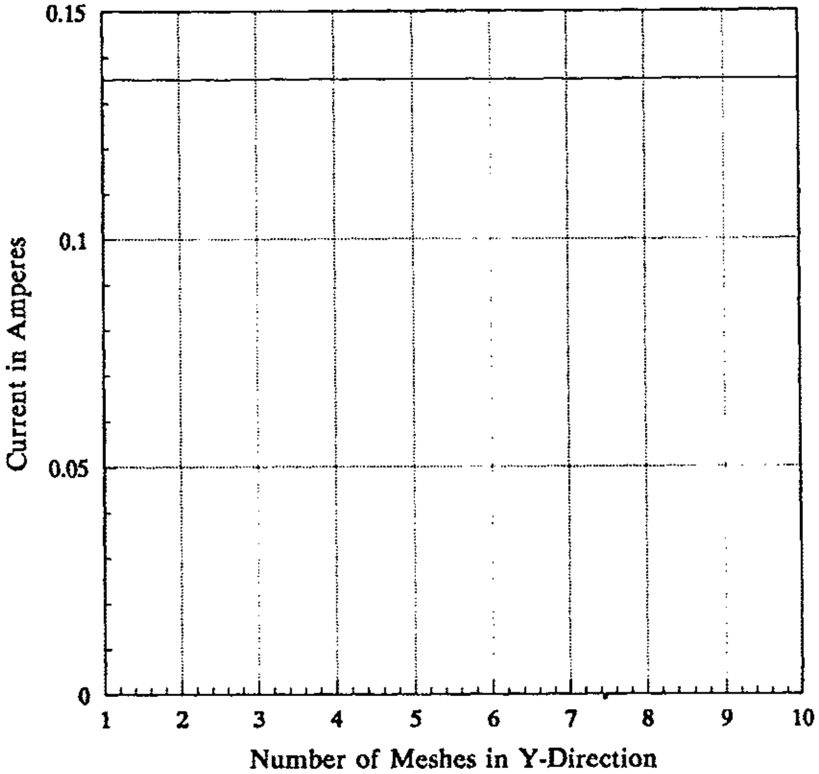

Figure 4.31. Total current through SAS device at 20 nSec.

They show, as expected, that the current progressively increases from 10 ns to 20 ns as the biasing pulse is turned on. Furthermore, the longitudinal currents are all equal and there is no transverse variation. This result provides a consistency check for the 2D simulations employed here, since one expects the gradient of the total current to be zero based on the following argument. Basically, since the total current has to be conserved, $J^{tot} = J_x^{tot} + J_y^{tot}$ = constant. However, $J_y^{tot} = 0$ since there is no conduction path along the transverse y-direction. Since J^{tot} is a constant, the curl of J^{tot} has to be zero. But the curl of J^{tot} equals: $\mathbf{a}_z\,[dJ_y^{tot}/dx - dJ_x^{tot}/dy] = \mathbf{a}_z\,[0 - dJ_x^{tot}/dy] = -\,\mathbf{a}_z\,dJ_x^{tot}/dy$. As a result, $dJ_x^{tot}/dy = 0$ as borne out in the simulation results of Figures 4.29-4.31.

4.3.2 TWO-DIMENSIONAL RESULTS AND ANALYSIS: CASE II

Results for the second doping profile are examined next. This test case is the inverse of the previous profile, with the dopant density being centro-symmetric with a minimum level at the central axis and the maximum at the two end surfaces. Before discussing the results obtained, it is instructive to look at some of the obvious differences. First, we compare the average conductive ratio between the two cases by evaluating the dopant charge. Since the conductance "G" is proportional to the carrier density, a ratio of the conductances $G_I/G_{II} = \rho_I^{av}/\rho_I^{av}$. For the dopant distributions chosen here, this ratio works out as given below with L_T being the transverse length along the "y" axis.

$$\frac{G_I}{G_{II}} = \frac{\int_0^{L_T} [\, \frac{1}{2} + \frac{1}{2}\sin(\frac{\pi y}{L_T}) \,]\, dy}{\int_0^{L_T} [\, 1 - \frac{1}{2}\sin(\frac{\pi y}{L_T}) \,]\, dy} \approx 1.2 \ . \tag{4.1}$$

Hence, the average conductivity for case I is larger than that of case II. This implies that on an average, the carrier or doping densities are higher for case I. It therefore follows that the circuit currents can be expected to be higher in case I as compared to case II. A second point pertains to anticipated relative values of the peak electric field within the device. Based on simple P-N junction theory [40], the maximum internal electric field E_{max} at any voltage is a monotonic function of the average doping density "N_{av}". Thus: $E_{max} \alpha (N_{av})^{1/2}$. This implies that the peak electric field for case I would be higher than those for case II. As a result, impact ionization is expected to be relatively strong for case I and not as dominant for the case II device.

Simulation results for the initial unbiased steady state conditions within the SAS device are shown in Figs. 4.32-4.34. These profiles are in keeping with the results expected for the chosen centro-symmetric distribution. The peak magnitude of the ionized impurity density nearly equals 5 x 10^{16} cm^{-3} which is the maximum concentration of dopant atoms, and occurs at the two edges. The unbiased steady state electric fields associated with the charge distributions of Figs. 4.32-4.34 are shown in Figs. 4.35-4.36.

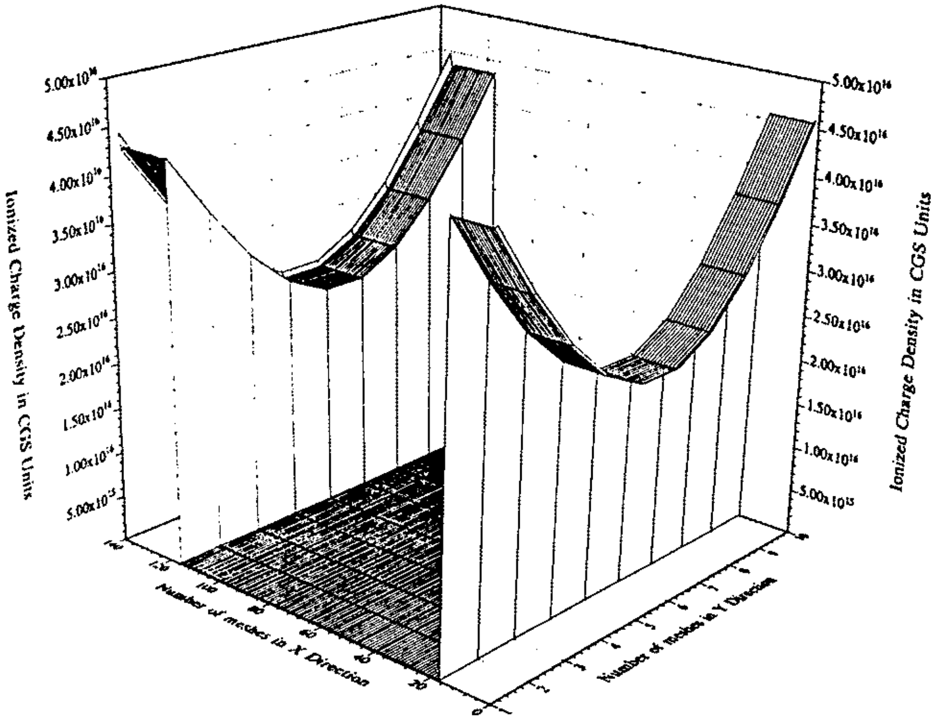

Figure 4.32. Initial ionized charge density: unbiased.

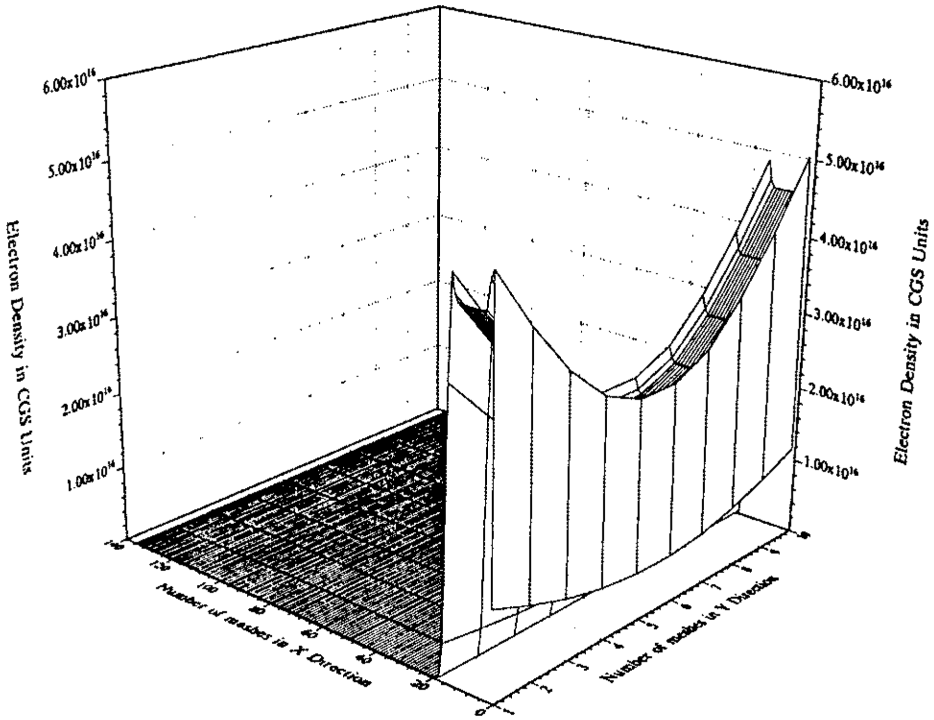

Figure 4.33. Initail electron density: unbiased.

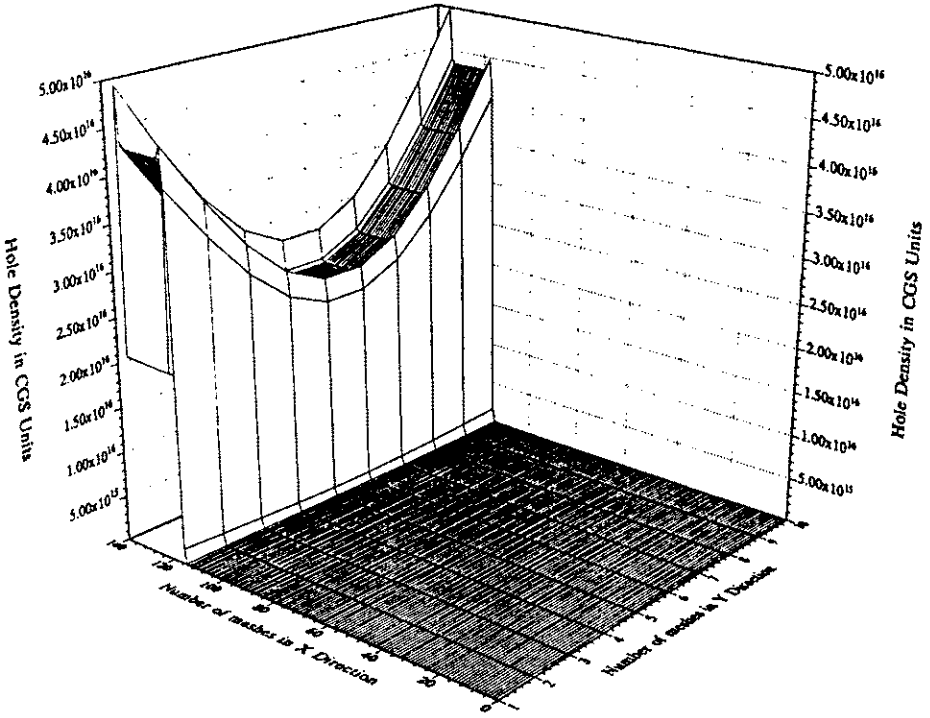

Figure 4.34. Initial hole density: unbiased.

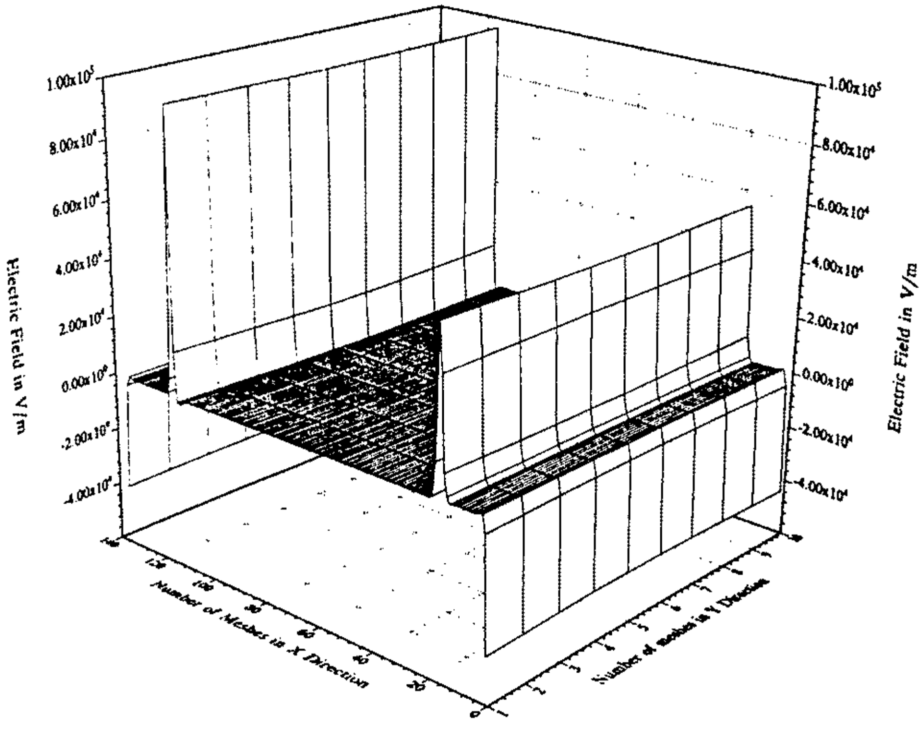

Figure 4.35. X-component of internal electric field profile: unbiased.

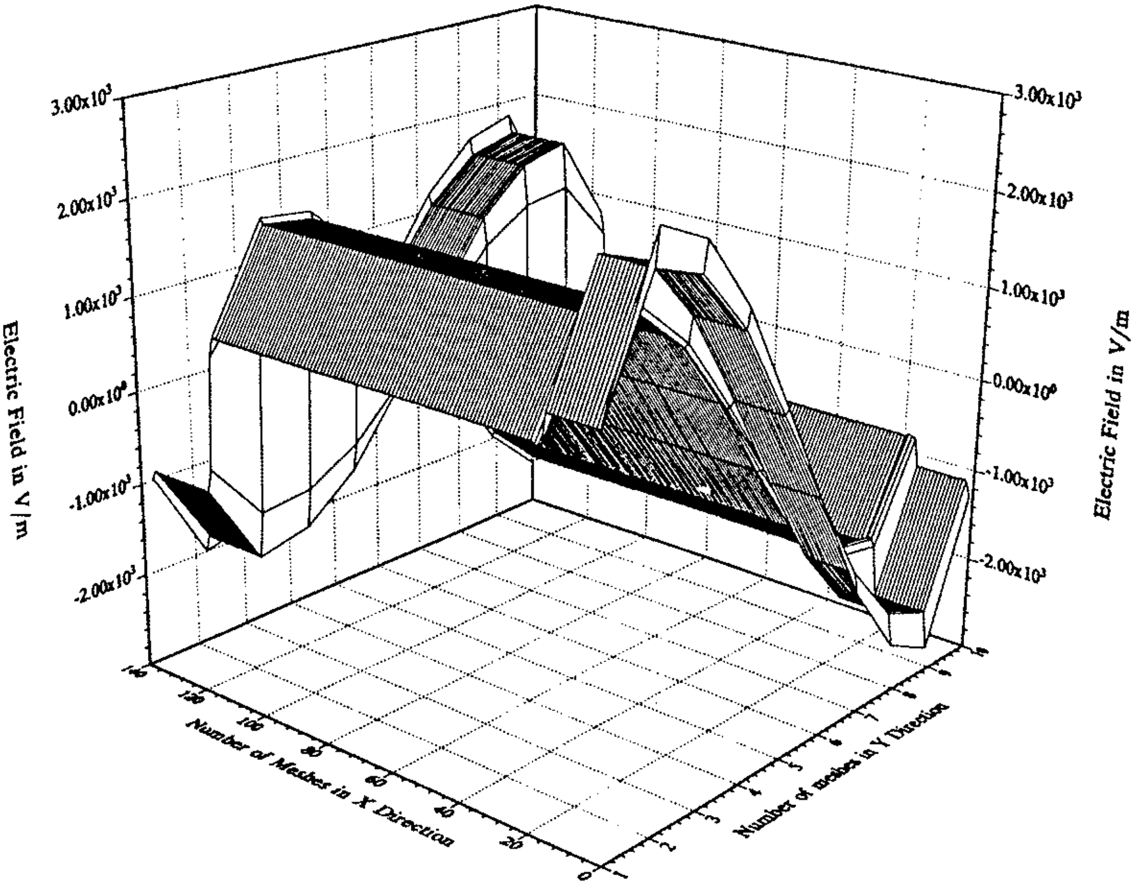

Figure 4.36. Y-component of internal elctric field profile: unbiased.

The longitudinal electric field distribution E_x shown in Figure 4.35 is similar to that of Figure 4.5 for the 1D case. The transverse field E_y is seen in Figure 4.36. It is the reversed image of Figure 4.18. The areas having positive E_y values in Figure 4.18 are negative in Figure 4.36, and vice versa. Such behavior is expected since the electric field depends on the density gradient, and the gradient in case II is negative of case I. The transient SAS circuit voltage waveforms for the 2D simulations are shown in Figure 4.37. The transient current corresponding to this voltage waveform is shown in Figure 4.38. This plot differs from the corresponding results for case I that were shown in Figure 4.20 in two respects. (i) First, the value of the circuit currents for case II are generally lower than those for case I. For instance, the initial displacement current spike is about 5.2 Amperes in case I but only 3.6 Amperes in case II. The maximum currents during the applied voltage pulse at about 20 ns and 46 ns are also smaller for case II. These smaller current magnitudes are the result of a lower average conductance G_{II} for case II as compared with case I. Such a result is expected and was briefly discussed above through equation (4.1). (ii) Next, the sharp current pulses produced around 20 ns and 46 ns during the voltage ramps in case I are absent in case II. Instead, a broad current pulse having a 5 ns time duration results in case II. The production of such a broad pulse is not very useful for pulse shaping applications. The absence of a sharp current peak in case II suggests a lack of strong impact ionization and internal avalanching. This result is a direct consequence of a lower average device doping which leads to lower values of the maximum electric field E_{max} as has been discussed above. These lower field values preclude the onset of strong avalanching, and the launching of a rapid ionization wave.

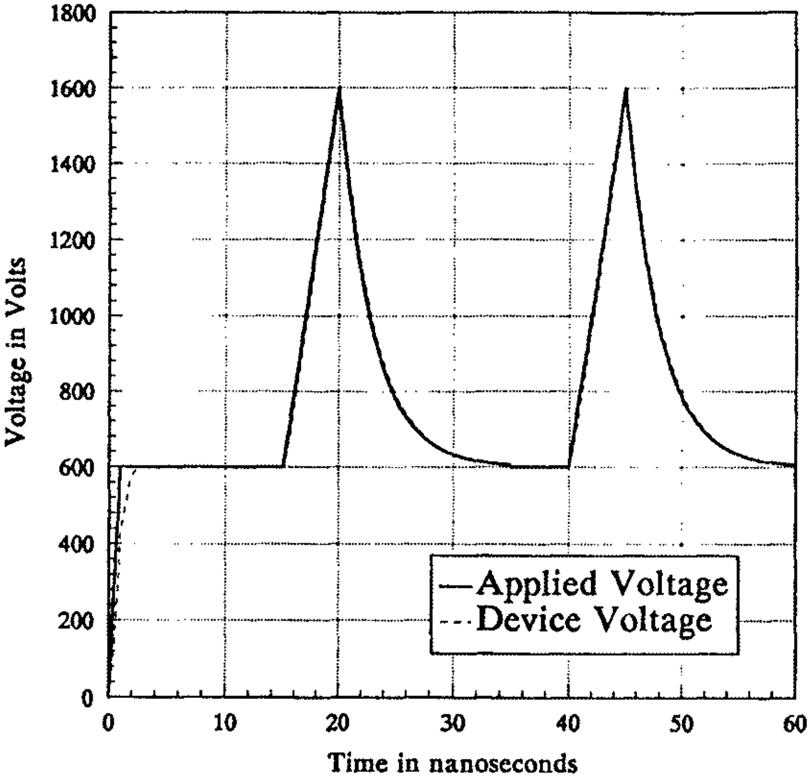

Figure 4.37. Time dependence of voltages.

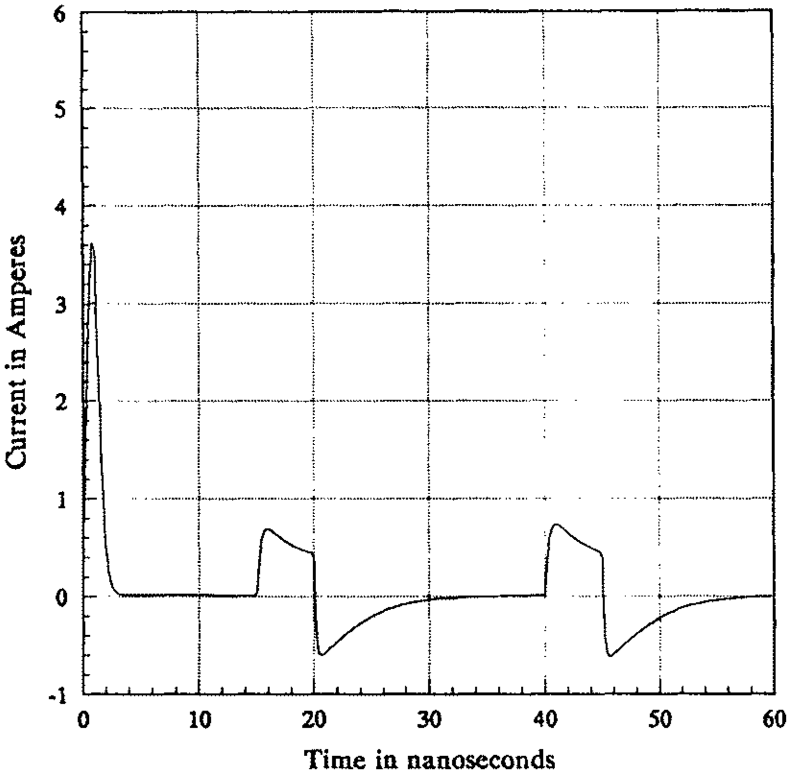

Figure 4.38. Current transient through the SAS device.

Given this lack of strong internal ionization, the current waveform only displays an initial displacement current rise at around 15 ns and 40 ns as the voltage ramp is applied. This is followed by a monotonic decrease as the voltage drop across the 50 Ohm series resistor increases. As a result of increases in the 50 Ohm resistive drop, the device voltage cannot grow quite as fast which leads to a weakening of the displacement current.

Results of the internal electric field E_x at 10 ns and 20 ns are presented in Figures 4.39-4.40. These plots reveal some growth and propagation of the internal field. This growth and propagation occurs mainly towards the outer edges. Correspondingly, the value of the electric field over the outer portions of the P^+-N junction in Figure 4.40 are not as high as those over the center. This is in keeping with the requirement that the line integral of the longitudinal field E_x have a constant value across all paths parallel to the longitudinal axis. The primary difference between Figure 4.40 and the case I plot of Figure 4.23 lies in the magnitudes of the electric field. The peak values in Figure 4.40 are at about 1.7×10^7 V/m, while those of Figure 4.23 are at 1.85×10^7 V/m. The lower values of the maximum field work to dramatically reduce the impact ionization since the process has an exponential dependence on the electric field. As a result, ionization and avalanching in the device of case II is not as strong, and does not give rise to a sharp current amplification.

Snapshots of the longitudinal conduction current at 18 ns and 20 ns within the SAS device are shown in Figures 4.41-4.42. The plot of Figure 4.41 shows that the conduction current is relatively large throughout the N^+ and the P^+ regions as expected due to the large supply of free cariers. However, in the middle N-region, the current is

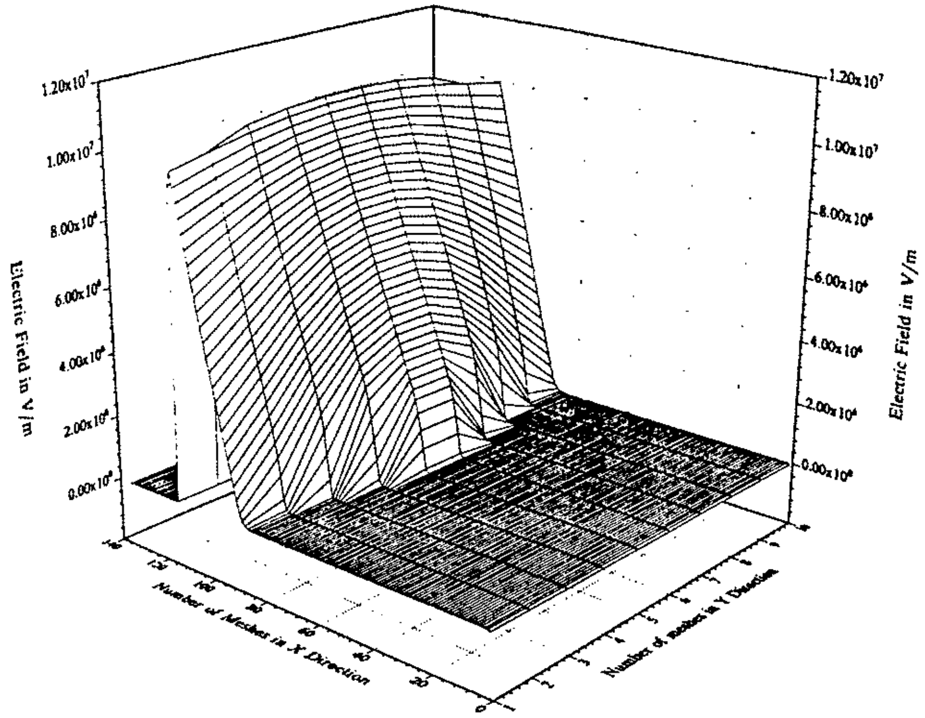

Figure 4.39. X-component of internal electric field at 10 nSec.

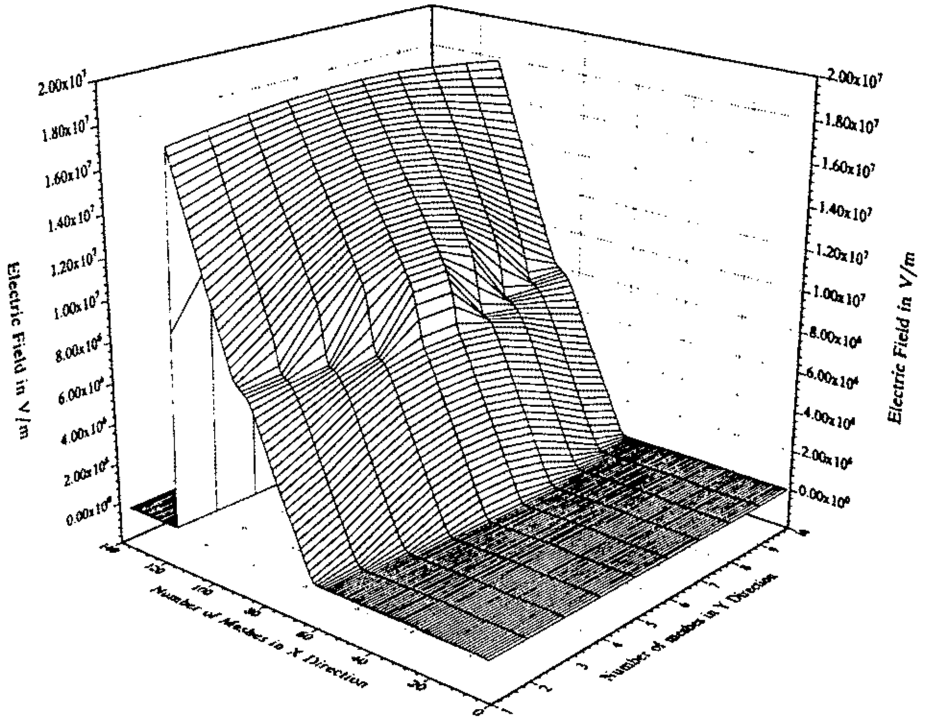

Figure 4.40. X-component of internal electric field at 20 nSec.

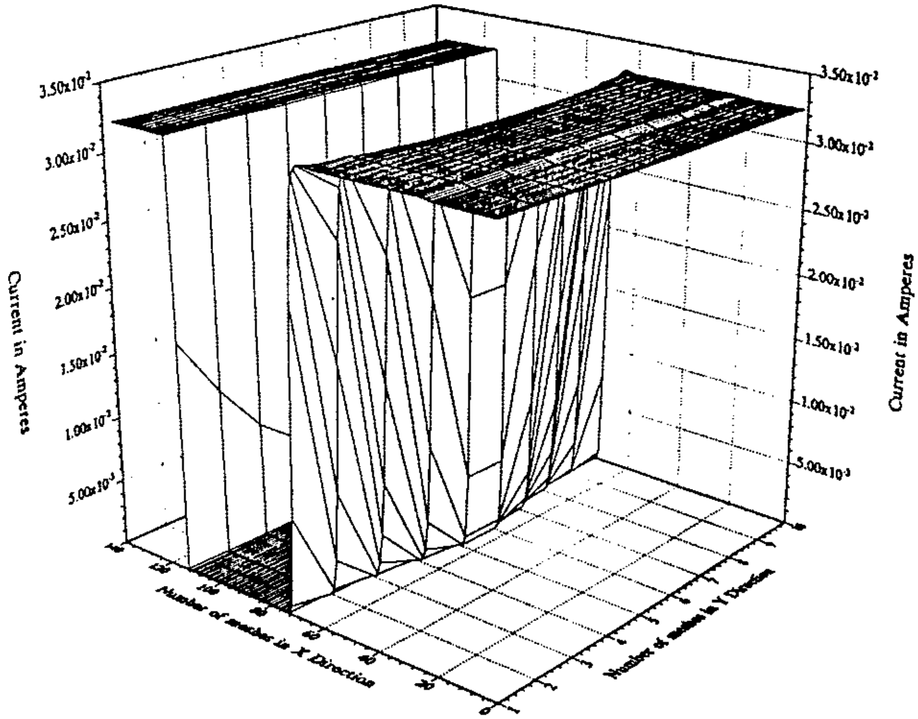

Figure 4.41. X-component of conduction current at 18 nSec.

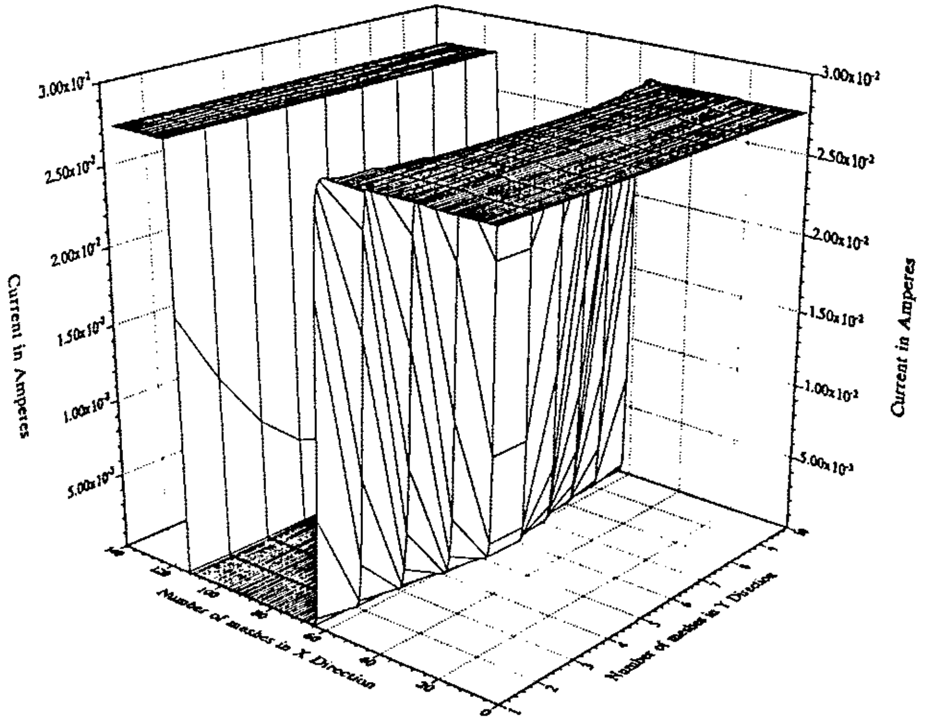

Figure 4.42. X-component of conduction current at 20 nSec.

almost negligible. Furthermore, no filamentary growth or localized current flow enhancements are evident. This result is completely different from that obtained in Figure 4.26. Even at 20 ns there is no evidence of any localized growth in the particle current. In fact, the current magnitude at 20 ns is slightly lower than that at 18 ns. This again indicates the lack of impact ionization and electronic injection across the P^+-N boundary.

The total longitudinal current I_x as a function of the transverse direction is shown in Figures 4.43-4.44. These plots were obtained from the simulations at 10 ns and 18 ns. As in case I, the longitudinal currents are constant throughout the device with no transverse variation once again validating the 2D simulations model.

4.3.3 TWO-DIMENSIONAL RESULTS AND ANALYSIS: CASE III

Simulation results for the asymmetric doping profile are examined next. This case represents an aberration in the doping distribution. The ionized dopant distribution is shown in Figure 4.45. In this case the total dopant charge inside the device is greater than both of the two previous cases. As a result, the device conductance "G" is correspondingly higher, implying that the circuit currents can be expected to be higher than previously obtained. Since the average dopant densities are higher, the peak electric field values within the device should also be larger. This is indicative of stronger impact ionization for this device.

Simulation results for the electron and hole densities under unbiased steady state conditions within the SAS device are shown in Figures 4.46-4.47. These profiles are in keeping with the results expected for the asymmetric distribution of Figure 4.45. Effects

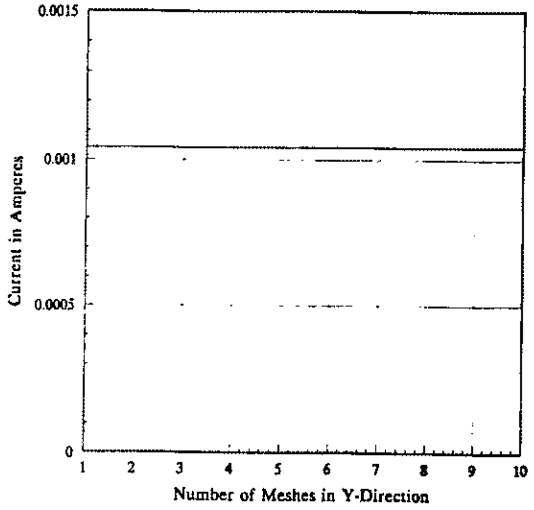

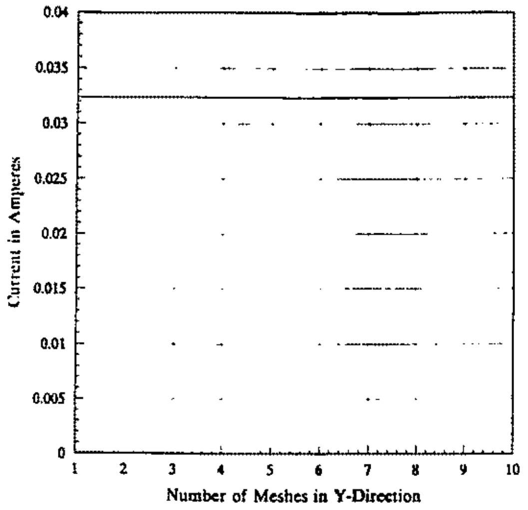

Figure 4.43. Total current through SAS device at 10 nSec.

Figure 4.44. Total current through SAS device at 18 nSec.

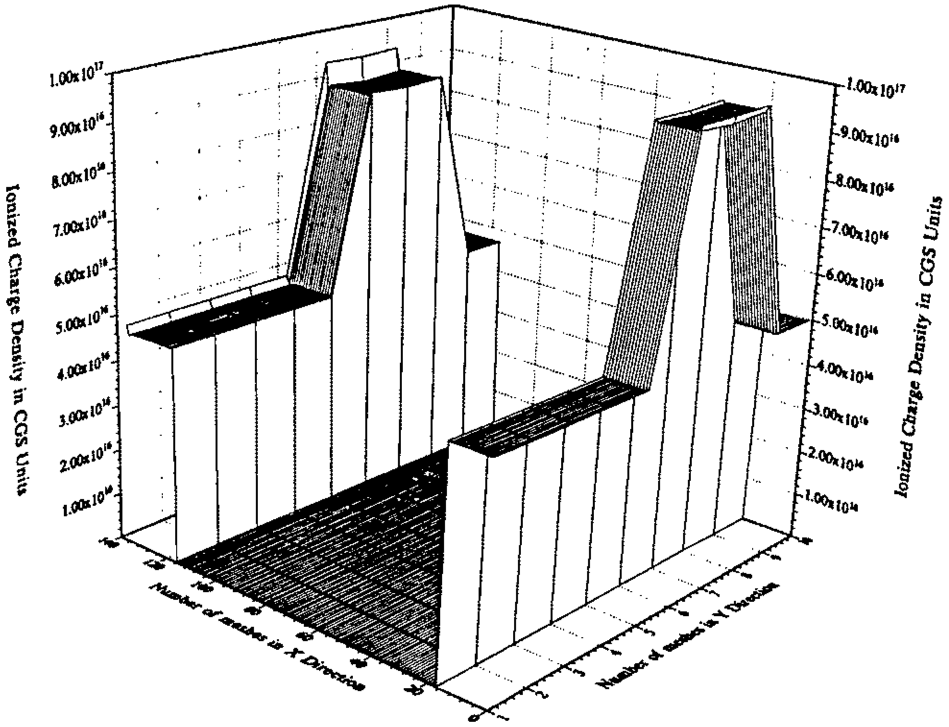

Figure 4.45. Initial ionized charge density: unbiased.

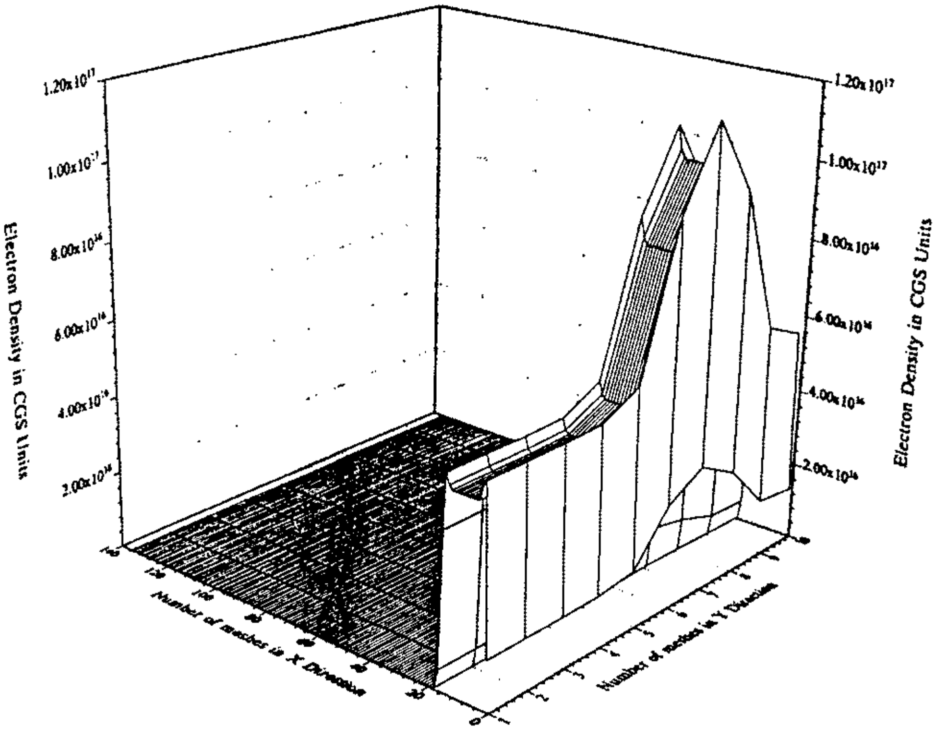

Figure 4.46. Initial electron density: unbiased.

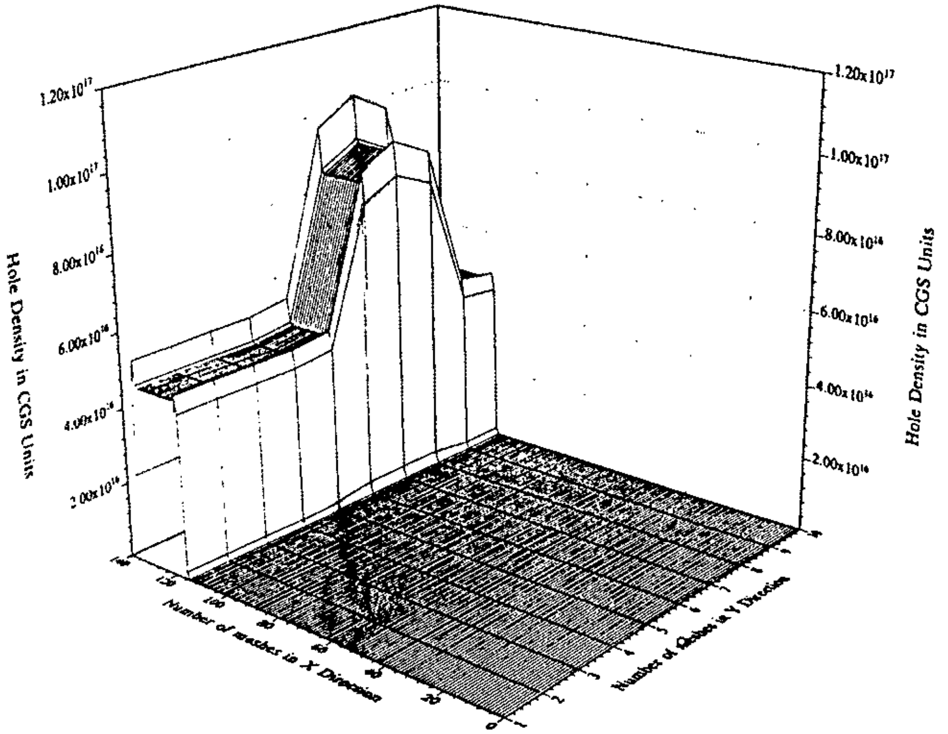

Figure 4.47. Initail hole density: unbiased.

of diffusion and transverse spreading are obvious. The unbiased electric fields are shown in Figures 4.48 and 4.49. The longitudinal electric field distribution E_x is similar to that of Figures 4.5, 4.17 and 4.35. The transverse field E_y of Figure 4.49 show the effects of diffusion. The values are close to zero near the Y=0 plane since the dopant density is constant and the effect of diffusion is negligible. Once again, the polarity of E_y is reversed going from the N^+ side to the P^+ side.

The transient SAS circuit voltage waveform and the transient current are shown in Figures 4.50 and 4.51. The values of the circuit current are much higher than those for cases I and II. For instance, the maximum currents during the applied voltage pulse at about 20 ns and 46 ns are about 4 and 5 Amperes, as compared to 2.2 and 1.8 Amperes for case I. Such high values of the current are associated with the large device conductance and the ability for strong impact ionization on the basis of larger electric fields.

Results of the internal electric field E_x at 18 ns and 20 ns are presented in Figures 4.52 and 4.53 which show the propagation of an internal electric field wave. The electric wave, however, does not move into the N-region in a uniform manner. Instead, its dynamics and propagation is determined by the doping non-uniformity along the transverse direction. For example, the region of highest doping occurs over a longitudinal strip located between meshes 7 and 9 along the Y-direction. The electric field at the P^+-N junction is therefore highest over Y-meshes 7 to 9, with the smallest penetration into the N-region. The small penetration is the result of a large slope in the E_x profile, since the slope is proportional to the ionized dopant density in accordance with Gauss' law.

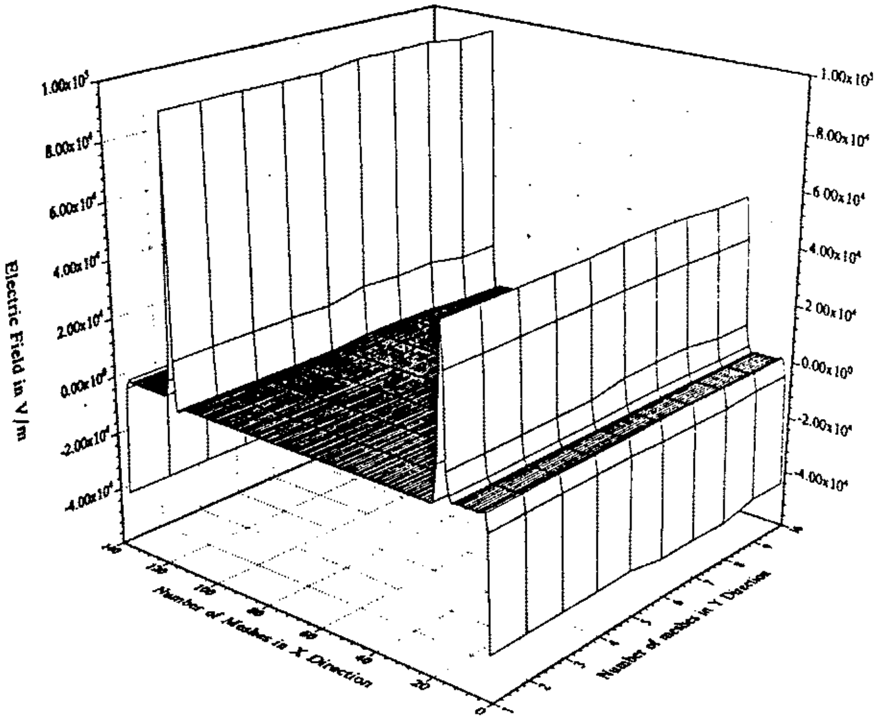

Figure 4.48. X-component of internal electric field profile: unbiased.

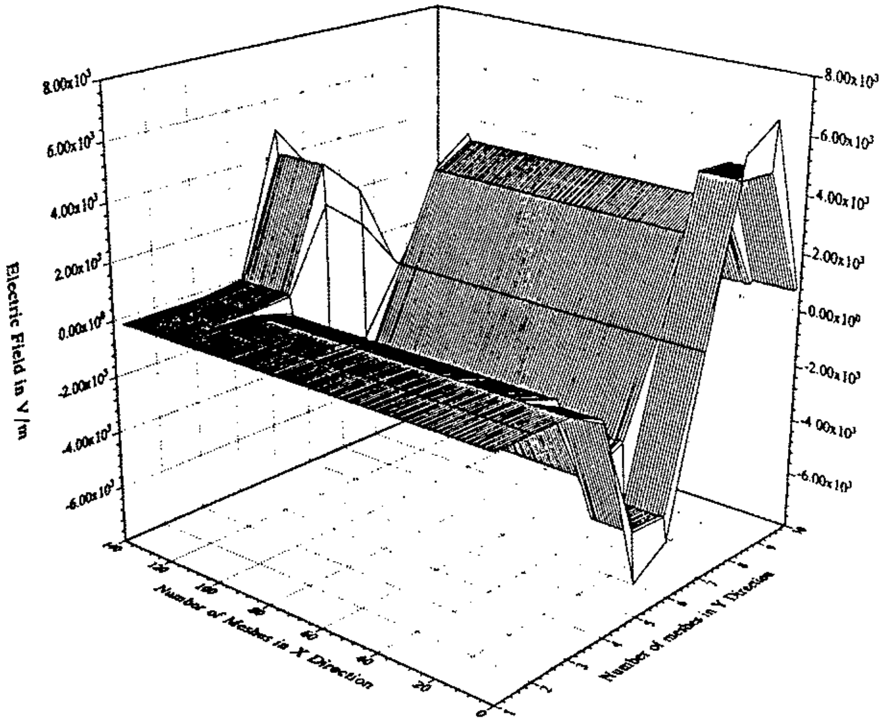

Figure 4.49. Y-component of internal electric field profile: unbiased.

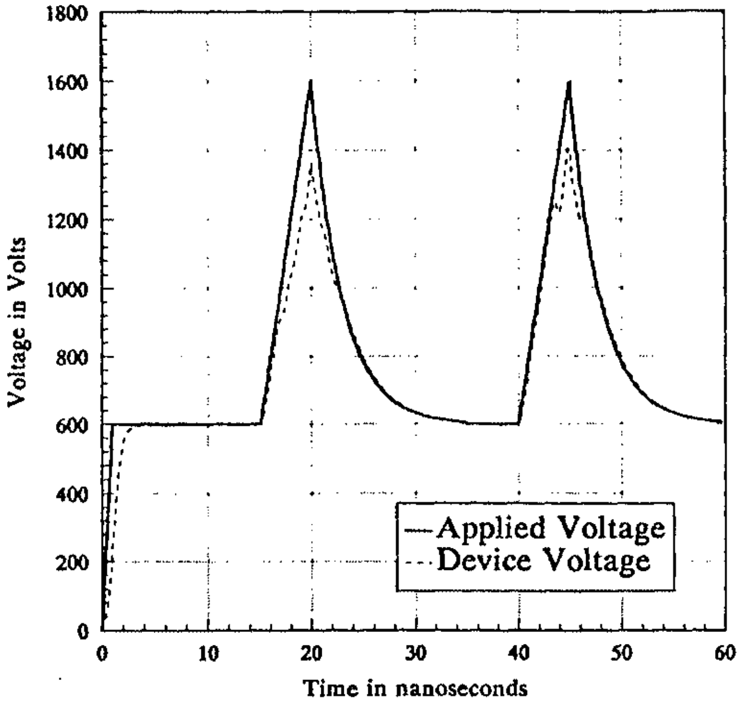

Figure 4.50. Time dependence of voltages.

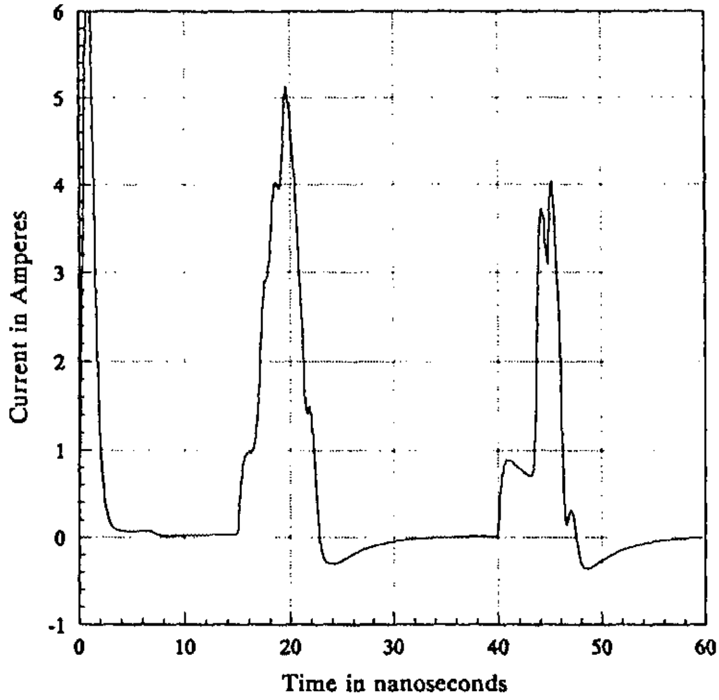

Figure 4.51. Current transient through the SAS device.

Similarly, values of the electric field maxima at the P^+-N junction, away from the strip between Y-meshes 7 through 9, are not as large. However, the field extends deeper into the N-region due to the smaller slope in $E_x(x)$ associated with the smaller ionized dopant density. On application of the voltage pulse, the fields begin to increase in magnitude and spread into the N-region. However, the wavefront moves non-uniformly along the transverse direction. Electric field propagation into the N-region over the strip between Y-meshes 7 to 9, is the slowest because of the high doping. The peak value, however, exhibits a fast growth as seen in Figure 4.52. Conversely, the propagation and spreading of the electric field over the regions outside the high doping strip is much faster, even though the peak field values do not increase quite as much. This behavior is evident in Figure 4.52 which shows an E_x wave moving faster in an asymmetric fashion. At 20 ns, this non-uniform movement is even more apparent. A distinct hump is seen towards the left surface of the device roughly given by mesh coordinates X = 80, Y = 2.

Finally, plots of the longitudinal conduction current at 18 ns and 20 ns are shown in Figures 4.54 and 4.55. The plots indicate that unlike the previous cases, the conduction current is not largest within the N^+ and the P^+ regions. This is due to the relatively negligible electric fields E_x in these regions which reduces the carrier drift velocities, and hence the conduction current, to negligible levels. Instead, there are two localized areas of large conduction current. These occur within the N-region near the P^+-N junction at the two transverse ends, and are removed from the asymmetric highly doped strip. These areas of high conduction current are also seen to be moving towards the N^+

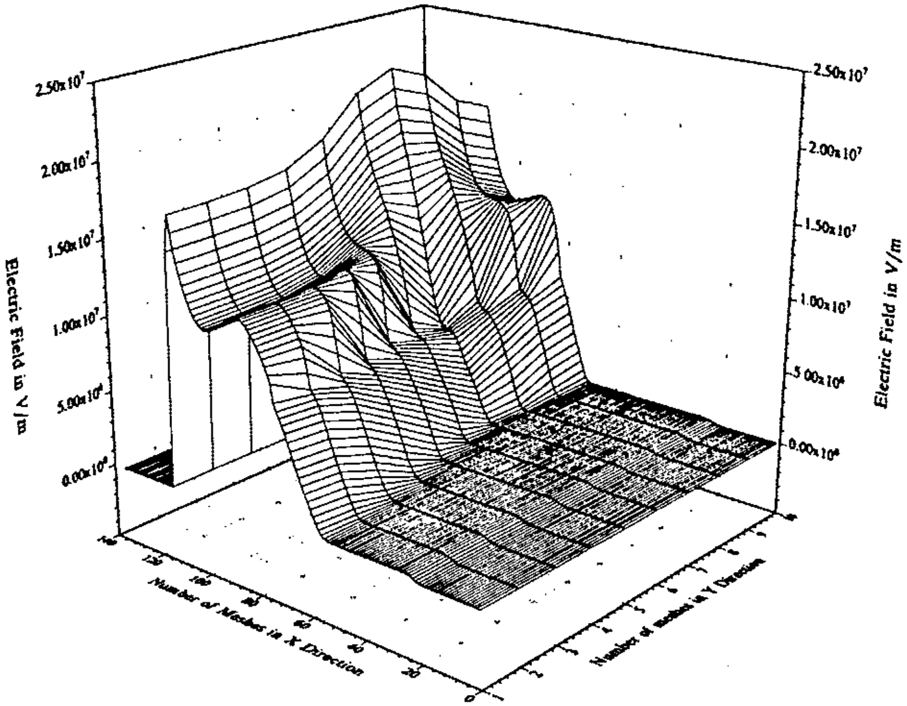

Figure 4.52. X-component of internal electric field at 18 nSec.

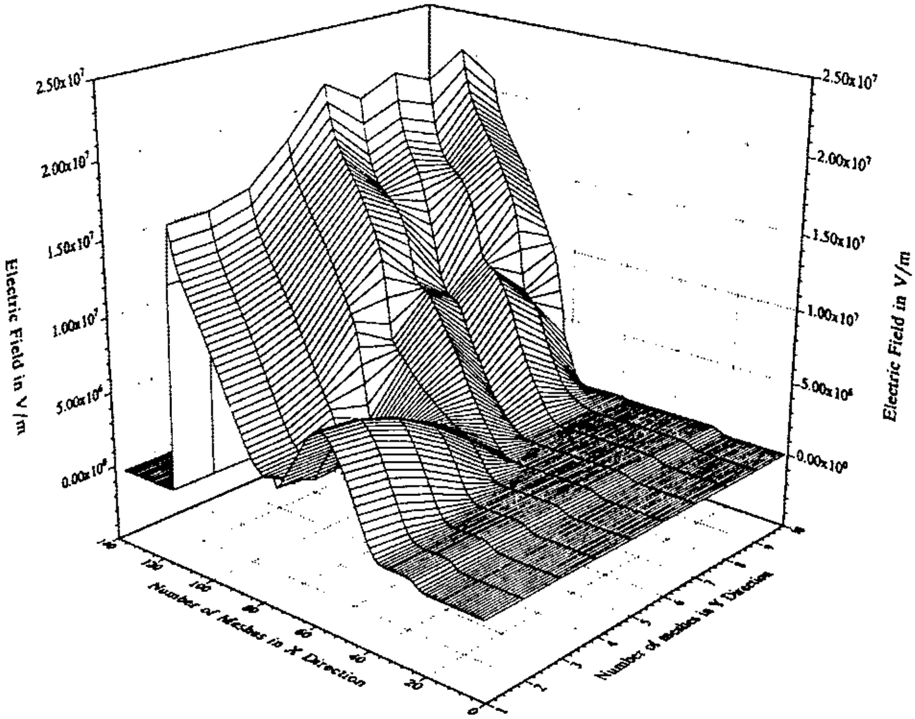

Figure 4.53. X-component of internal electric field at 20 nSec.

region as gauged from the locations of the peaks at 18 ns and 20 ns. This movement is brought about by the propagating electric field.

There is some similarity between this situation and that chosen for case I. Both involve convex shaped transverse doping profiles with minima at the two outer boundaries. One might therefore expect the conduction current distributions to be somewhat similar. However, a comparison of Figures 4.55 and 4.27 shows that this is not the case. For example, while case I exhibits a partial conductive filament at the central axis, most of the conduction current in Figure 4.55 occurs towards the two boundaries away from the center. This difference is associated with the following features: (i) The existence of a much stronger transverse diffusive process as compared to case I, due to the sharper gradient in the doping profile. This diffusion works to force mobile carriers away from the higher doped asymmetric longitudinal strip, towards the outer boundaries more efficiently. (ii) The presence of much higher values of the maximum electric fields E_x throughout the P^+-N junction as compared to case I. The doping for case III is the same or higher than that of case I for all points. The higher fields lead to exponential increases in the ionization coefficients.

The two factors mentioned above work to produce the following sequence within the N-region. As the turn-on voltage ramp is applied, the mobile carriers that lie just outside the P^+-N depletion region begin moving. This produces a conduction current wave and the free carrier density begins to increase within regions to the right. However, the process of diffusion, forces the excess charge away from the asymmetric high doped longitudinal strip and towards the outer boundaries. With time, the internal electric fields

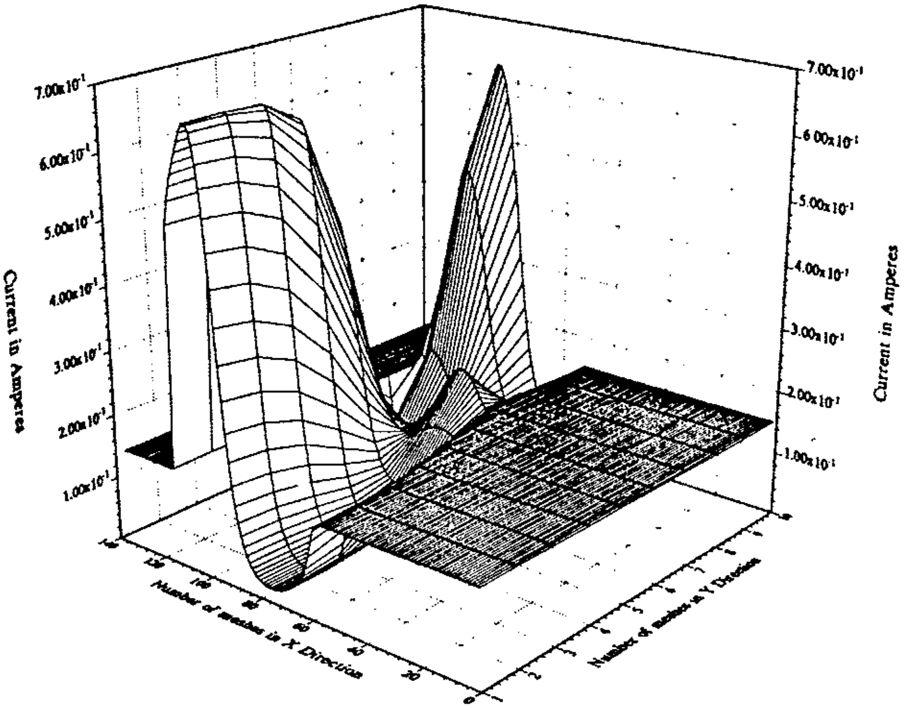

Figure 4.54. X-component of conduction current at 18 nSec.

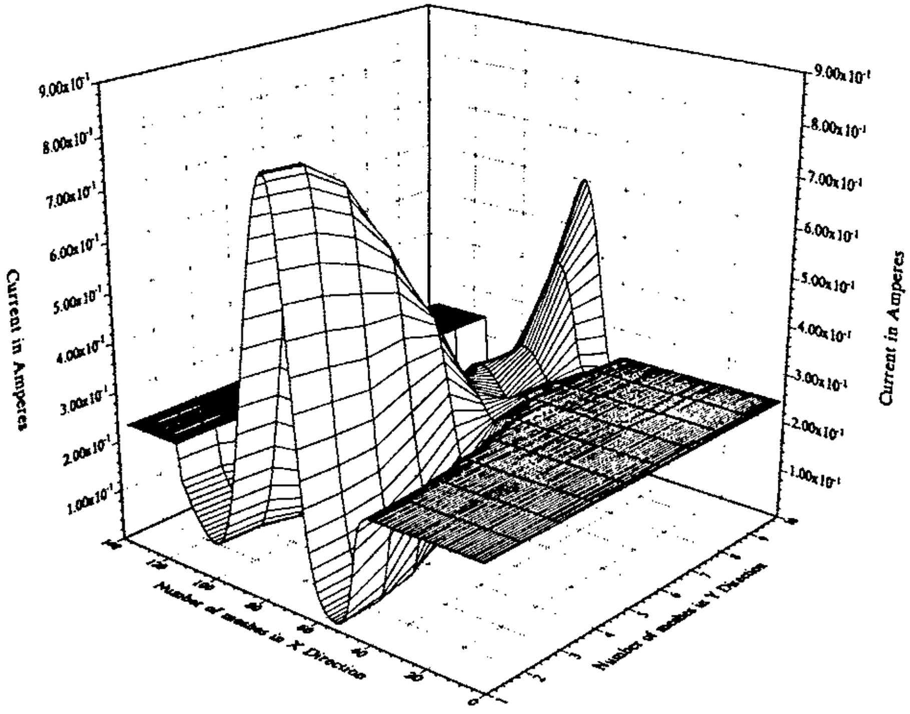

Figure 4.55. X-component of conduction current at 20 nSec.

increase leading to larger values of E_{max} at the P^+-N junction boundary and the expansion of the field deeper into the N-region. The former initiates the impact ionization process and initiates electron injection into the N-region. The latter enhances the local drift velocity values, significantly increasing the drift velocity and hence the conduction current. However, since the electric field does not move as fast nor does it increase as much over the asymmetric strip, the growth in the drift velocity is not quite as large. Besides, strong carrier diffusion forces the mobile carriers away from the strip and towards the two boundaries. Increase in the conduction currents at the boundaries is therefore stronger.

Though such diffusion along the transverse direction also occurs in case I, it is relatively weak. As a result, increases in carrier density towards the boundaries due to diffusion of charge injected over the central axial layer, is not very strong. Furthermore, the doping densities towards the boundaries in case I are about 50 percent weaker than those in case III. As a result, the peak electric fields towards the boundaries in case I are much lower than those for case III. The result, is that impact ionization and avalanching towards the boundaries is relatively weak in the situation of case I. This precludes any significant growth of a conduction current away from the boundaries for case I, unlike the behavior for case III shown in Figure 4.55.

The occurrence of a crest in the conduction current of Figure 4.55 signifies the formation and movement of single electronic wavepacket. Only a single wavepacket or electronic swarm is produced due to the internal polarization effect. As the electrons get injected into the N-region from the P^+-N junction following impact ionization, the value of the maximum electric field begins to collapse due to the polarization. This reduces the fields below the impact ionization threshold, and prevent the subsequent and continuous launching of electron waves into the N-region. As a result, only one swarm or packet of electrons are injected into the N-region. A high conduction current associated with this electron packet as it moves in the N-region towards the N^+ side appears in the snapshot picture of Figure 4.55.

4.3.4 TWO-DIMENSIONAL RESULTS AND ANALYSIS: CASE IV

Finally, 2D simulation results for an SAS device having a uniform dopant profile along the transverse direction were also obtained for completeness. Basically, this represents 2D modeling of the SAS device that was examined through the 1D simulations in section 4.1. Figure 4.56 shows the density of internal immobile charge, which has no variations along the transverse direction as expected. The transient current of Figure 4.57 shows a behavior similar to that of Figure 4.3. The growth and propagation of an electric field wave starting from the P^+-N junction is evident in Figures 4.58-4.60. Again there are no variations along the transverse axis due to the uniformity of the dopant profile. This leads to near-zero transverse electric fields E_y within the device at all times as shown in Figures 4.61 and 4.62. Finally, the conduction current distributions within the simulated SAS device at two different times during the applied voltage pulse are shown in Figures 4.63 and 4.64. From the plot of Figure 4.63 it can be seen that the conduction currents within the P^+ and N^+ regions are almost equal and uniform. Since a high density of free carriers is available in these regions, the drift (and hence the conduction current) component dominates and is nearly equal to the total current I_T. Requirement of current continuity and the conservation of total current I_T therefore dictates that the conduction currents in the P^+ and N^+ regions nearly equal I_T and hence match each other. The current within a portion of the N-region that lies towards the N-N^+ boundary is also composed mainly of the drift current. This region is just beyond the P^+-N depletion boundary, and has a supply of free electrons available for conduction. Even though their densities are slightly lower than those within the N^+ and the P^+ regions, a larger drift velocity driven by higher electric fields compensates for the difference. This occurs because the electric field increases more quickly in the N-region than in either of the P^+ or N^+ regions. As a result the carrier drift velocities are quickly enhanced, and the drift current component within this portion of the N-region can match the currents in the N^+ and P^+ regions. However, the absence of free carriers within the depletion region on the P^+-N junction, leads to near-zero conduction current levels. This is clearly evident in Figure 4.63. At a later time of 20 ns, the process of avalanching and electron injection over the P^+-N junction changes the conduction current distribution. As the electric field at the P^+N junction increases and crosses the impact ionization threshold during the voltage ramping, a wave of electrons is injected into the N-region. This produces two effects: (i) The drift component is increased within the N-region lying near the P^+ boundary, and (ii) The rate of increase in the electric field is lowered. This decrease in the rate can also be viewed as a polarization effect. Suppression of the electric field due to this polarization effect, prevents the subsequent launching of electron waves into the N-region. Furthermore, turning off the applied voltage at 20 ns, also precludes a

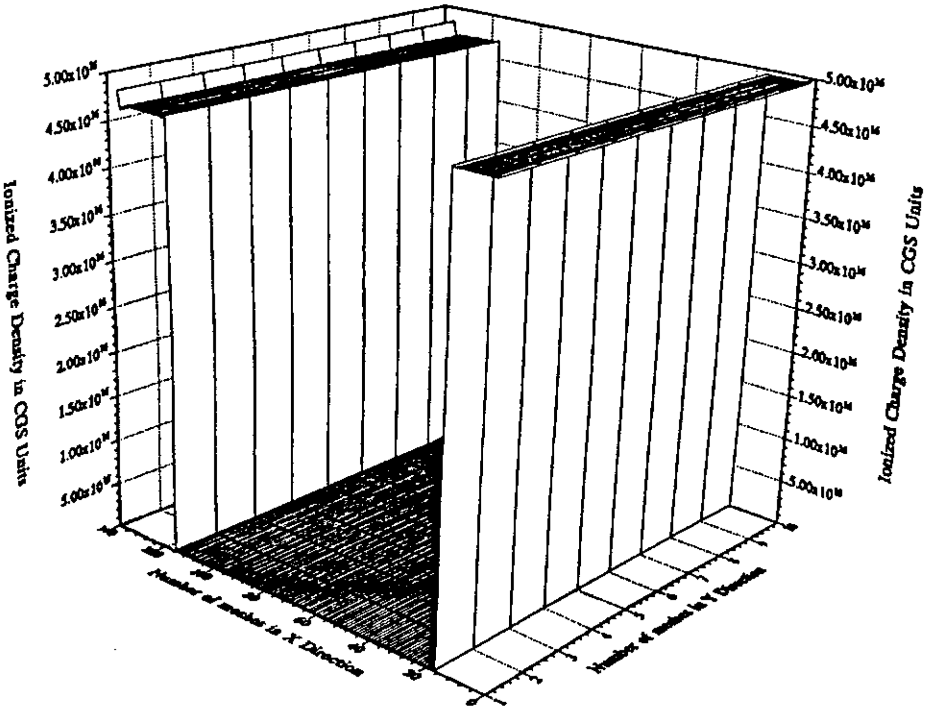

Figure 4.56. Initial ionized charge density: unbiased.

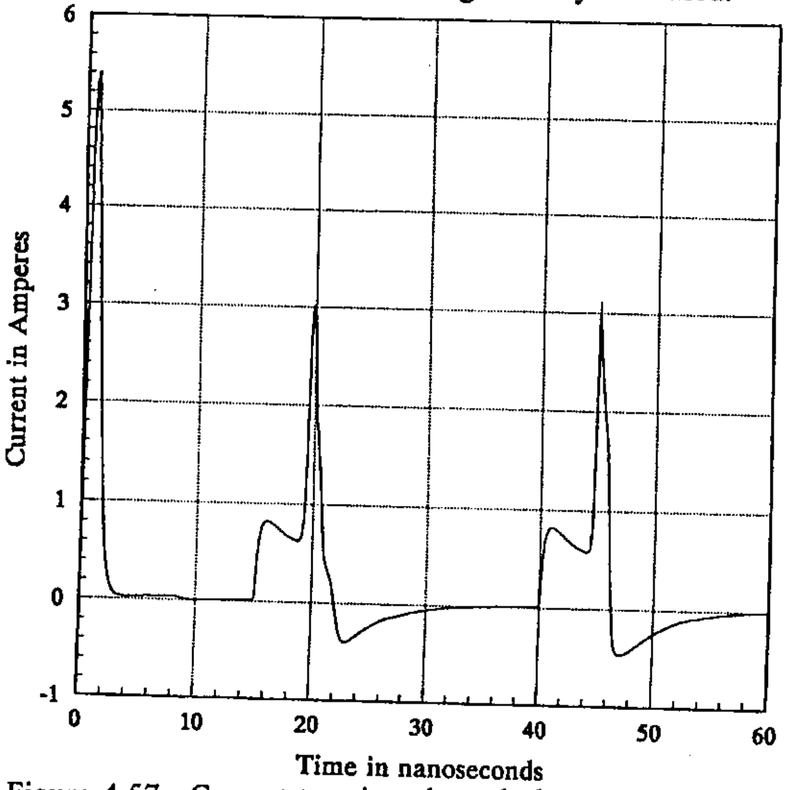

Figure 4.57. Current transient through the SAS device.

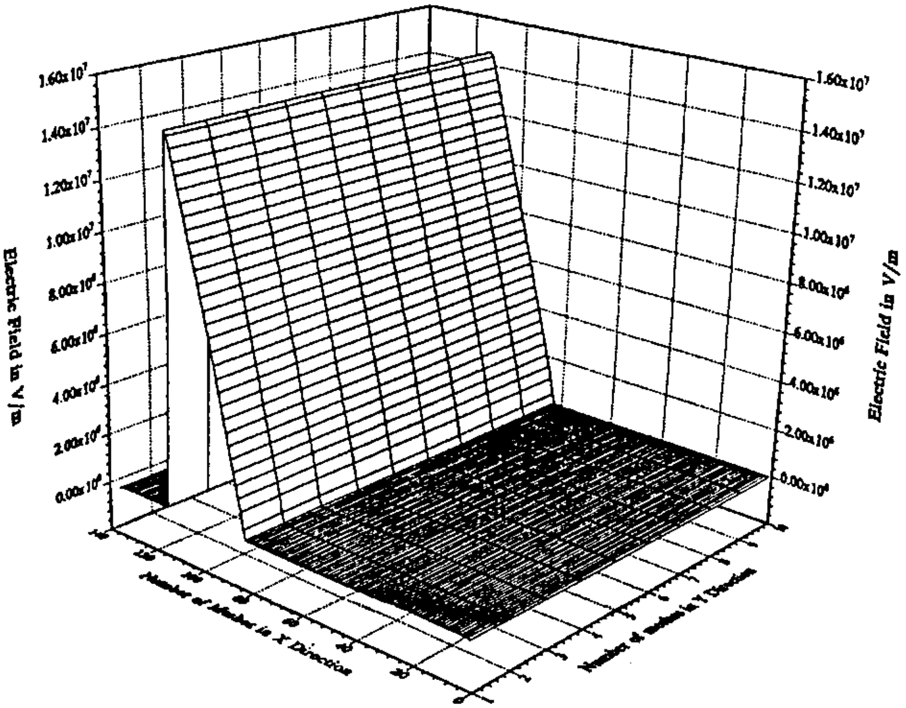

Figure 4.58. X-component of internal electric field at 10 nSec.

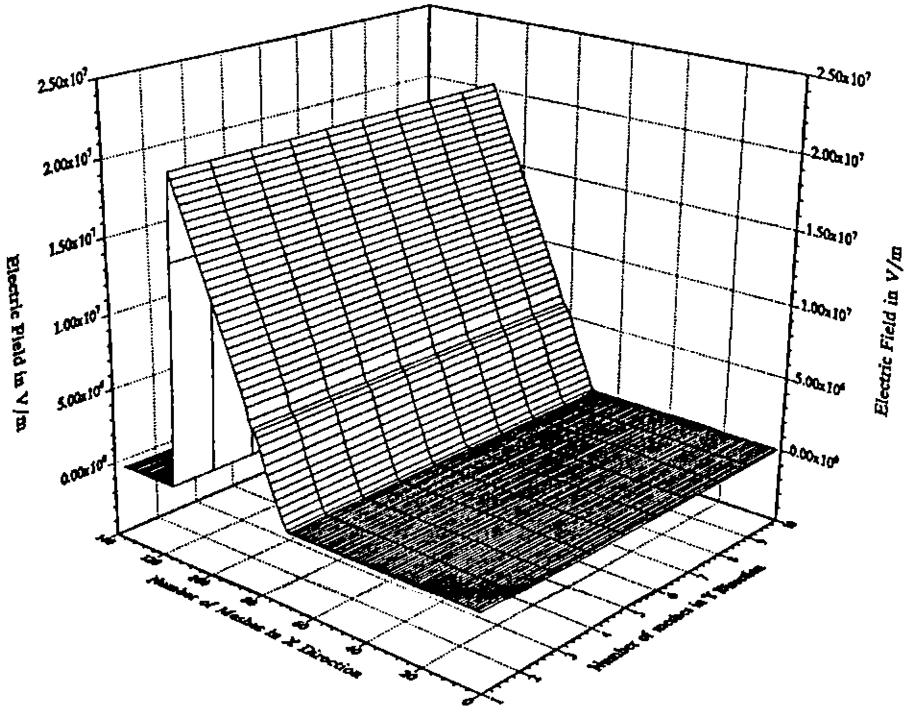

Figure 4.59. X-component of internal electric field at 18 nSec.

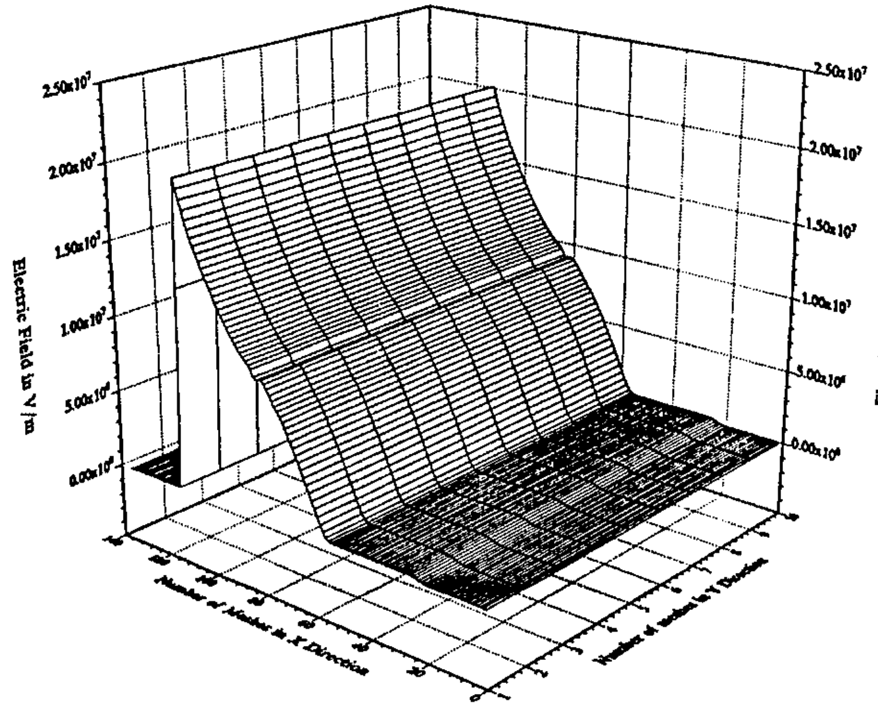

Figure 4.60. X-component of internal electric field at 20 nSec.

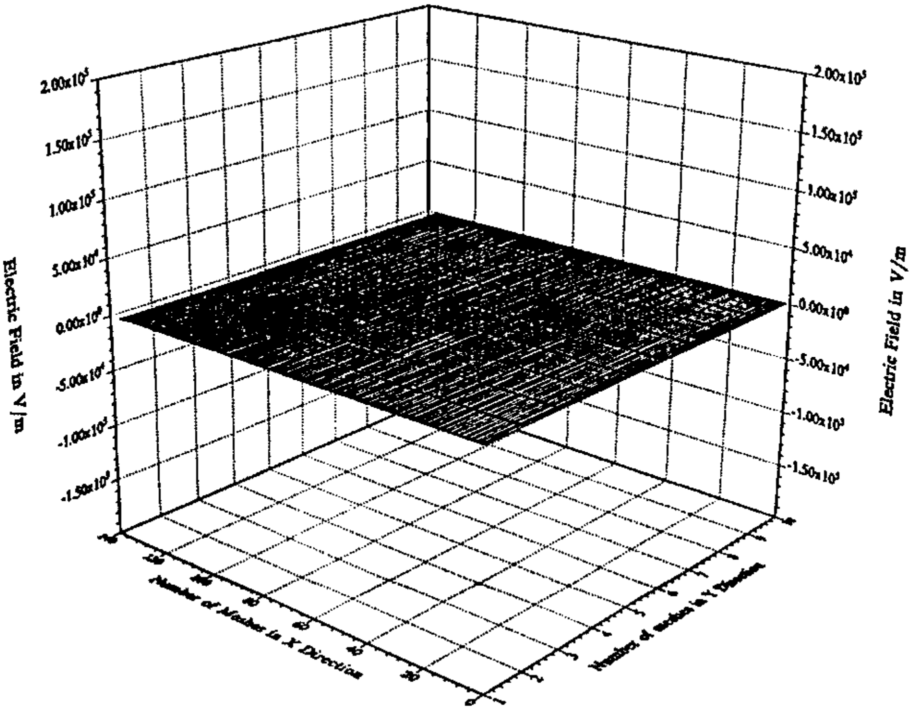

Figure 4.61. Y-component of internal electric field at 10 nSec.

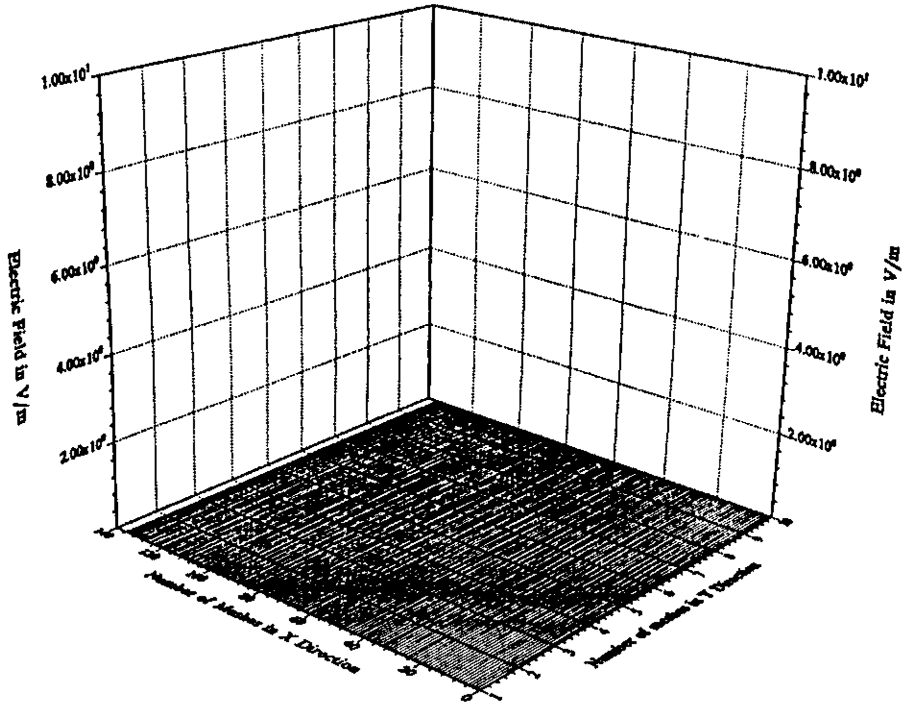

Figure 4.62. Y-component of internal electric field at 20 nSec.

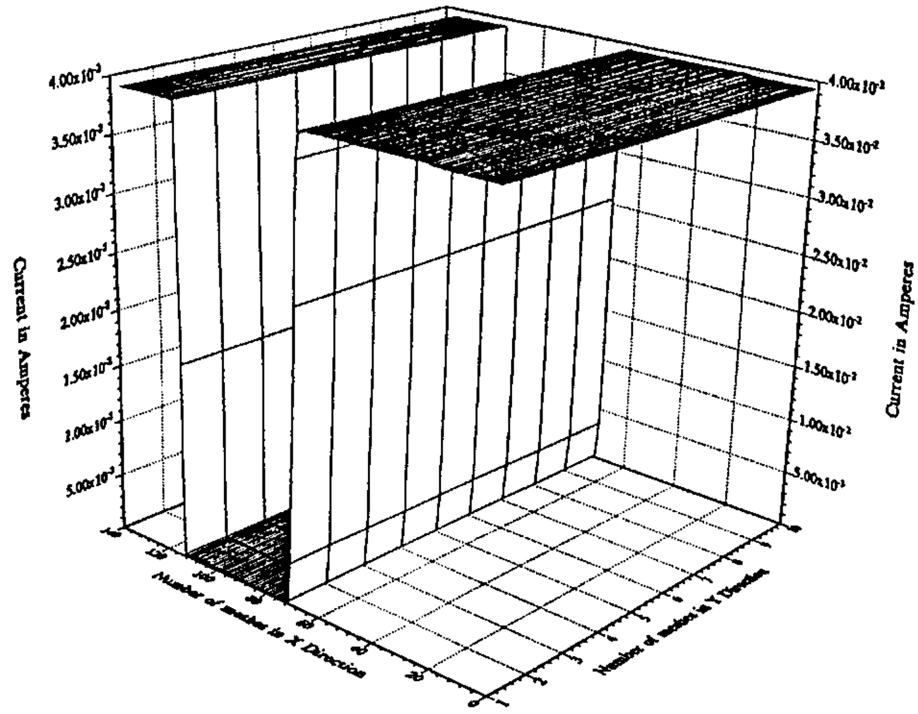

Figure 4.63. X-component of conduction current at 18 nSec.

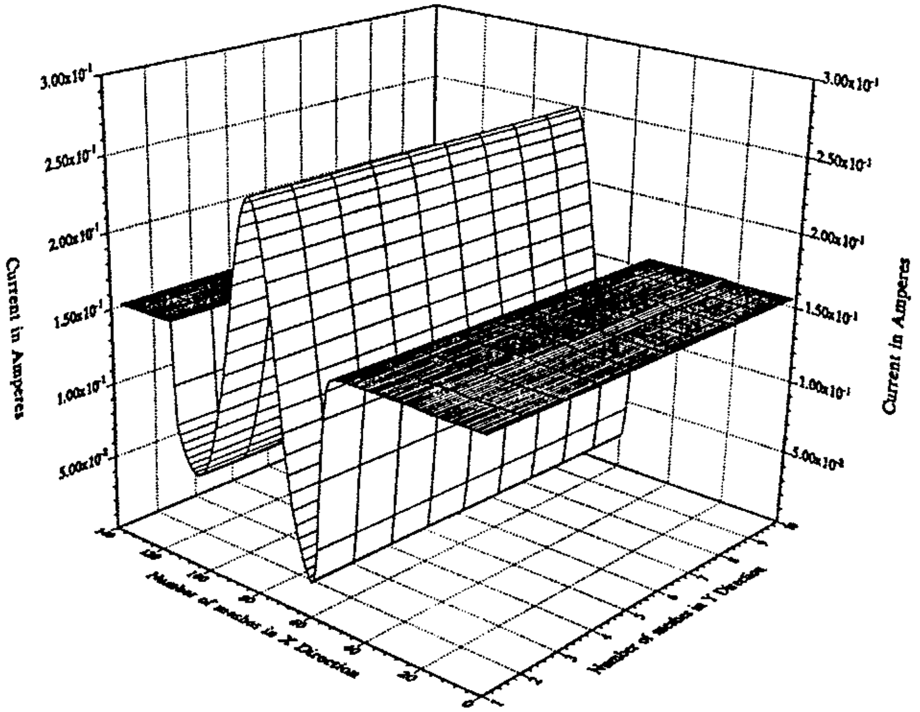

Figure 4.64. X-component of conduction current at 20 nSec.

continuous and steady electron injection. As a result, only one swarm or packet of electrons are injected into the N-region. A high conduction current is associated with this electron packet as it moves in the N-region towards the N^+ side. This appears in the snapshot picture of Figure 4.64 as the crest of a conduction current wave located near the P^+-N boundary.

CHAPTER 5

CONCLUSIONS AND FUTURE WORK

5.1 SUMMARIZING CONCLUSIONS

Silicon Avalanche Shaper devices have been projected as being important components of an inexpensive, semiconductor-based all-electrical technology for high power switching applications. The primary advantage of this technology is that it is based on Silicon material which is easy to fabricate and has a well established processing technology. Unlike other high power technologies, the SAS devices do not rely on the more expensive GaAs material. The use of semiconductors reduces the size and weight of the overall system. The primary purpose of the SAS devices is to provide high voltage pulse shaping capabilities which are required for applications involving high voltage pulse generators, high energy pulsed lasers, impulse radars and ultrawideband microwave generators. Another advantage of the compact SAS switches is that they do not rely on external optical triggering. This eliminates the need to have additional lasers and related optical circuitry. Instead, the SAS devices are triggered by electrical means such as the application of a fast voltage ramp. In so doing, the device can be activated within sub-nanosecond time frames producing currents in the Ampere range.

The SAS based high power switching technology has been pioneered and tested by the Russian group. The preliminary results have been very encouraging. However, the device reliability and its operating capability at high voltages have not been studied in detail. Furthermore, the test experiments conducted so far have used simple doping profiles. The effects of tailoring the doping profile, or the impact of transverse variations on the electrical characteristics have not been studied. Also, as with other semiconductor based high energy, pulsed-power systems; there might be a potential for internal current filamentation and device breakdown. This aspect has also not been investigated and can best be studied and understood through numerical simulations.

In this thesis research, a two-dimensional simulator for the SAS device has been developed based on the drift-diffusion model. It represents the first attempt to obtain device performance predictions and the anticipated transient device response. The 2D semiconductor model was successfully implemented into a numerical code. The role of transverse variations in the doping profile were then analyzed by obtaining the transient current characteristics. Four different doping profiles were studied through the numerical simulations. The dynamics of development, growth and propagation of internal electric field waves were also analyzed. These studies provide useful insight into the physics of the avalanche process. Finally, predictions of potential current filamentation within the device for a given doping profile were obtained. Simulation data for the conduction current distribution within the device at various time instants, clearly showed growth of filamentary modes.

A number of important conclusions can be drawn from the results presented in the previous chapter. The main deductions and salient features are as listed below.

(1) The dopant densities are seen to strongly affect the circuit currents by controlling the device conductance. Both the magnitude and the temporal shape can vary dramatically with changes in the doping profiles. In general, the current

magnitudes are higher for larger doping. This is the combined result of two factors: (i) An increased conductance which reduces the overall resistance in the circuit, and (ii) the increased value of the electric field at the p-n junction which enhances impact ionization.

(2) Current pulses having durations in the sub-nanosecond range were seen to result upon the application of much broader voltage pulses. However, there seems to be a trade-off between current pulse sharpness and the potential for instability linked to current filamentation. Sharp and narrow current pulses, as obtained in the simulations of section 4.3.1 and 4.3.3, are associated with the growth of filamentary currents. The sharp pulses were the direct result of strong impact ionization and avalanche action. However, the avalanche process can be very non-uniform due to doping variations giving rise to localized surges in the conduction current. Though such localized current may not be detrimental over a short duration, the device could be destroyed during repetitive operation as a result of prolonged internal heating. The absence of sharp current pulses, on the other hand, provides for more stable operation. This was demonstrated through the transient current curve shown and discussed in section 4.3.2.

(3) Evidence of a distinct electric field wave propagating from the cathode to the anode of the SAS device was presented through the various simulations. The movement and propagation of the electric field wave was seen to be non-uniform in general, and dependent on the doping variations along the transverse dimension.

Larger values of the doping created a slower moving wave since the associated depletion regions did not increase quite as rapidly.

(4) Associated with a propagating electric field wave, was a travelling conduction current. For "near-uniform" profiles along the transverse direction, the conduction current was seen to develop over regions of highest doping density, and to propagate away towards the anode. Furthermore, this conduction current was due to mobile electrons. This result seems to suggest that slight increases in the dopant density over the central portions of the SAS device could potentially be detrimental. The corresponding conduction current increases and possible temperature enhancements over the central portion, would be more difficult to control or quench. Dopant density increases near the outer surfaces or peripheral regions might present a less acute problem since the associated temperature enhancements could be controlled through external cooling. Fortunately, the doping profiles resulting from the diffusion process naturally provide such doping enhancements over the peripheral regions.

(5) Carrier diffusion was seen to be important for profiles having strong gradients in the doping profiles. For instance, the results of section 4.3.3 showed that localized areas of high conduction currents could arise in regions with moderate doping. This was caused by rapid transverse diffusion. This suggests that there is an optimal gradient of the doping along the transverse direction which would lead to a more uniform current flow. Since "near-uniform" profiles cause filaments over regions of highest doping, while sharp gradients give rise to

filaments over regions of relatively low doping, a moderate gradient would lead to a more even current distribution.

(6) The impact ionization and avalanching processes within the SAS device are caused by holes rather than electrons. During the turn-on transient, holes move from the N-region towards the P^+ side of the junction in response to the voltage pulse. The reason that holes dominate the carrier generation process as compared to electrons, is associated with the doping densities on either side of the P^+-N junction. The minority electron densities on the P^+ side are relatively much smaller than the minority hole densities on the N-side. Consequently, on applying the voltage ramp, more minority holes are able to traverse the high field region at the P^+-N junction boundary from the N-side, than minority electrons from the P^+-side. As a result, carrier generation is facilitated mainly by the overwhelming population of moving holes.

(7) Finally, the SAS devices were seen to require at least 25 ns to make a complete recovery to their original state following a voltage pulse. This time is expected to increase with the transverse dimensions of the device. Such increments in the transverse device dimensions may be necessary for enhancing the current carrying capability. However, by increasing the transverse dimensions, the recovery time would be adversely affected.

(8) As regards the doping of the N^+ and P^+ contact regions, the simulation data suggests that increases in the concentration would lead to enhancements in the circuit currents. The process of impact ionization would also increase due to the

higher values of the electric fields at the junction. Hence, a high doping density of about 10^{18} cm^{-3} at the P^+ and N^+ end regions, appears to be a desirable goal. These levels can realistically be attained through high temperature diffusion.

5.2 SCOPE FOR FUTURE RESEARCH WORK

The research presented in this thesis focussed on developing numerical simulation codes for the two-dimensional modeling of the SAS switches. This technology has shown promise over other optical based switching approaches. The simulations developed here were meant to analyze a simple device geometry. The model was thus a first step towards the development of a more powerful two-dimensional device simulator. For example in this thesis, the contacts were assumed to be planar and to completely cover the two end surfaces. In reality, the metallic contacts may be circular in shape and may not cover the entire end face. Furthermore, the end surfaces were all taken to be parallel with respect to each other, and the device cross-section was uniform. In some of the actual devices that have been manufactured, the cross-sections have not been uniform, but instead have had trapezoidal cross-sections. The contacts too, may not necessarily be on opposite surfaces in an actual device. Both the anode and the cathode, for example, could be deposited on the front face for easier planar processing. Also, a simple external circuit consisting of a series resistance was used here. In general, however, the external circuitry could be more complicated and might involve inductors and capacitors for complex wave shaping. Finally, the doping variation along the transverse direction were assumed to be translational invariant along the longitudinal direction. This precluded the inclusion of localized variations in the doping density and point defects. All of the above elements could, however, be incorporated as additions to enhance the utility and applicability of the simulator. Including the enhancements would constitute the next set of research tasks. A summary of the various tasks and the scope of future research are listed below.

(i) Development of an enhanced two-dimensional model to include non-uniform device cross-sections. The non-uniform cross sections may be due to the planar processing techniques used during the fabrication process. In such a case, the two metallic contacts to the device would typically be placed on the same front surface. The cross-sections could also be non-uniform to suppress surface flash-over and dielectric breakdown. In order to avoid surface flash-over, for instance, the path length between the anode and cathode has to be increased as much as possible. Tapered trapezoidal cross-sections have been proposed in this regard to reduce the magnitude and the location of the maximum internal electric field distribution within the device.

(ii) Inclusion of more complex external circuits. Elements such as inductors need to be included for more realistic simulations. Such inductive elements could either be part of an actual pulse shaping circuit or may be associated with the self- and mutual-inductances of the connecting wires.

(iii) Allowing for more complicated variations in the doping profiles along the transverse direction. Such variations could include localized clumps and clusters, point defects and other profiles lacking translational symmetry along both the longitudinal and transverse directions. This would also reveal the potential for current filamentation due to the presence of localized traps.

(iv) The numerical simulations could also be performed for a class of other voltage waveforms. In the present study only one waveform was used throughout. Furthermore, the magnitudes of the peak turn-on voltage, its temporal shape, and turn-on slope could be varied for a more extensive evaluation.

(v) In this thesis, only P^+-N-N^+ structures were examined. As an extension, other possibilities such as the P^+-P-N^+ or the P^+-I-N^+ structures could be included.

(vi) This work focussed on the transient electrical response of a single SAS device. However, for applications requiring voltage scaling, a number of such SAS devices may have to be used in a serially stacked mode. Evaluating the performance of such a composite stacked arrangement could be another direction for extending the current simulations.

(vii) A final area of future research in connection with the SAS shaper devices might be to extend the analysis for heterojunction structures. Instead of having an all-Silicon device, the potential benefits of a Si-Ge heterojunction structure could be examined.

REFERENCES

1. I. V. Grekhov, Solid-State Electronics **32**, 923-930 (1989).
2. Ihor Vitkovitsky, in *High Power Switching*, (Van Nostrand Reinhold Company, New York, 1987).
3. R. D. Ford, I. Vitkovitsky, and M. Khan, Trans. Electrical Insulation **EI-20**, 29 (1985).
4. R. D. Ford and I. M. Vitkovitski, in *Proceedings of the Workshop on Solid State Switches for Pulsed Power*, edited by W. M. Portnoy and M. Kiristiansen, (Texas Tech University Press, Lubbock, TX, 1983), pp. 309-326.
5. V. K. Mathur, C. S. Chang, Wei-Lou Cao, M. J. Rhee, and Chi H. Lee, IEEE Journal of Quantum Electronics, **QE-18**, 205 (1982).
6. R. B. Hammond, IEEE Journal of Quantum Electronics, **QE-18**, 222 (1982).
7. G. Mourou, W. Knox, S. Wiliamson, Laser Focus **4**, 97 (1982).
8. J. B. Gunn, Solid State Commun., **1**, 88 (1963).
9. M. Weiner and A. Kim, in *High-Power Optically Activated Solid-State Switches*, edited by A. Rosen and F. Zutavern (Artech House, Boston, 1994), p. 219.
10. A. Rosen, P. Stabile, and P. Herczfeld, in *High-Power Optically Activated Solid-State Switches*, edited by A. Rosen and F. Zutavern (Artech House, Boston, 1994). p. 139.
11. V. A. K. Temple, IEDM Tech. Digest, **Abstr. 10.7**, 282 (1984); V. A. K. Temple, IEEE Trans. Elec. Dev. **ED-33**, 1609 (1986).

12. M. Stoisiek and H. Strack, in IEDM. Tech. Digest, 158 (1985).

13. J. P. Russels, A. M. Goodman, L. A. Goodman, and J. M. Nielson, IEEE Elec. Dev. Lett. **EDL-4**, 63 (1983).

14. B. J. Baliga, M. S. Adler, R. P. Lowe, P. V. Gray, and N. D. Zommer, IEEE Trans. Elec. Dev. **ED-31**, 821 (1984).

15. K. H. Schoenbach, V. Lakdawala, D. C. Stoudt, T. Smith, and R. P. Brinkmann, IEEE Trans. Elec. Dev. **ED-36**, 1793 (1989).

16. K. H. Schoenbach, V. Lakdawala, R. Germer, and S. Ko, J. Appl. Phys. **63**, 2460 (1988).

17. R. A. Falk and J. Adams, Proc. Optically Activated Switching **SPIE 1378**, 70 (1990).

18. M. Herman, K. M. Positeri, and R. A. Lewis, Proc. Optically Activated Switching **SPIE 1632**, 177 (1992).

19. I. V. Grekhov, A. Gorbatyuk, L. S. Kostina, S. V. Korotkov, and N. S. Yakovtchuk, Solid State Electronics **26**, 1132 (1983).

20. I. V. Grehhov, A. F. Kardo-Sysoev, M. Popova, S. V. Shenderei, Sov. Phys. Semicond. **17**, 877 (1983).

21. J. H. Zhao, T. Burke, D. Larson, M. Weiner, A. Chin, J. Ballingall, and T. Yu, IEEE Trans. Elec. Dev. **ED-40**, 817 (1993).

22. R. J. Lis, J. H. Zhao, L. Zhu, J. Illan, S. McAfee, T. Burke, M. Wiener, W. Buchwald, and K. Jones, IEEE Trans. Elec. Dev. **ED-41**, 809 (1994).

23. For example, R. S. Ramshaw in *Power Electronics Semiconductor Switches*, (Chapman and Hall, London, 1993).

24. For example, B. Jayant Baliga, in *Modern Power Devices*, (John Wiley, New York, 1987).

25. J. J. Ebers, Proc. IRE **40**, 1361 (1952); J. Moll, M. Tannenbaum, J. M. Goldey, and N. Holonyak, Proc. IRE **44**, 1174 (1956).

26. K. H. Schoenbach, in *High-Power Optically Activated Solid-State Switches*, edited by A. Rosen and F. Zutavern (Artech House, Boston, 1994), p. 95.

27. M. Gundersen, J. H. Hur, and H. Zhao, J. Appl. Phys. **71**, 3036 (1992).

28. I. V. Grekhov and A. F. Kardo-Sysoev, Sov. Tech. Phys. Lett. **5**, 395 (1979); I. V. Grekhov, A. F. Kardo-Sysoev, and L. S. Kostina, Sov. Tech. Phys. Lett **5**, 399 (1979).

29. I. V. Grekhov, V. M. Efanov, A. F. Kardo-Sysoev, and S. V. Shenderei, Sov. Tech. Phys. Lett. **9**, 527 (1983).

30. I. V. Grekhov and A. F. Kardo-Sysoev, L. S. Kostina, and S. V. Shenderei, Sov. Phys. Tech. Phys. **26**, 984 (1981).

31. B. L. Gelmont and M. Shur, Sov. Phys. JETP Lett. **11**, 350 (1970).

32. J. B. Gunn, IBM J. Res. Dev. **8**, 141 (1964).

33. M. Lundstrom in *Fundamentals of Carrier Transport*, edited by G. Neudeck and R. Pierre, (Modular Series on Solid State Devices, Addison-Wesley, N. York, 1990), Vol. 10.

34. S. Tiwari in *Compound Semiconductor Devices*, (Academic Press, N. York, 1992).

35. M. Kurata, in *Numerical Analysis of Semiconductor Devices*, (D. C. Heath Publishers, MA, 1985).

36. C. Jacoboni and P. Lugli, in *The Monte Carlo Method for Semiconductor Device Simulation*, (Spriger-Verlag, Wien, 1989).

37. S. Selberherr, in *Analysis and Simulation of Semiconductor Devices*, (Springer-Verlag, Wien, 1984).

38. M. Ruff, M. Mitlehner, and R. Helbig, IEEE Trans. Electron. Dev. **ED-41**, 1040 (1994).

39. R. G. Humphreys, D. Bimberg, and W. J. Choyke, Solid State Commun. **39**, 163 (1981).

40. For example, M. Shur in *Physics of Semiconductor Devices* (Prentice Hall, Englewood Cliffs, N. Jersey, 1990).

41. For example, J. Stoer and R. Bulirsch, in *Introduction to Numerical Analysis*, (Springer-Verlag, N. York, 1980).

42. R. J. Focia, E. Schamiloglu, C. Fleddermann, W. Nunnally, and J. Gaudet, Proc. of the IEEE Pulsed Power Conference, Albuquerque, N. Mexico, Vol. I, 592 (1995).